Magnetic and Charge Order in $LuFe_2O_4$ and $YbFe_2O_4$ Multiferroics

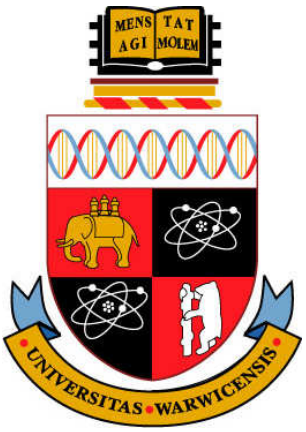

Hailey L Williamson
The University of Warwick
Department of Physics

A thesis submitted for the degree of
Masters by Research

25th January 2012

Abstract

Multiferroicity through the years has gained increasing interest based on a deeper understanding of the various types of ferroic coupling which exist, particulary in the rare earth oxides. Despite many years of research and investigation into the 'primary candidate' charge ordered multiferroic materials $LuFe_2O_4$ and $YbFe_2O_4$, a true understanding of their magnetism and charge order have only recently come to light. The following thesis presents detailed studies on the magnetism and charge order of $LuFe_2O_4$ and the potential multiferroic properties of $YbFe_2O_4$ in single crystal form.

The research performed over the last 20 years on the rare earth oxides has highlighted one main afflicting factor, governing the magnetic and charge order effects, especially within the $R Fe_2O_4$ series (R= Y, Ho, Er, Tm, Yb and Lu), which stems from a sensitivity to oxygen stoichiometry. Isostructural $LuFe_2O_4$ and $YbFe_2O_4$ both exhibit a coupling between magnetism and electric polarization, but the true origin is still unclear. $LuFe_2O_4$, once clarified as a material which exhibited ferroelectricity though charge ordering, has, through extensive neutron scattering, X-ray magnetic circular dichroism (XMCD) as well as wide range of macroscopic measurements, now been established as non-polar. Paying careful attention to the oxygen deficiency and its effects on crystal quality through basic magnetization measurements, $LuFe_2O_4$ can be characterized into four different qualities (poor to excellent). Therefore by tuning the stoichiometry, through a partial pressure $CO:CO_2$ atmospheric environment during crystal growth, via floating zone technique, an optimal single crystal of $LuFe_2O_{4-\delta}$ can be grown.

Magnetization measurements on $LuFe_2O_{4-\delta}$ grown in the $CO:CO_2$=1:5, exhibit two large transitions, one present at 235 K and representative of the paramagnetic to ferrimagnetic phase, followed by a smaller but greatly defined transition at 175 K, indicative of spin glass behavior previously reported. Identical measurements performed on the $LuFe_2O_{4-\delta}$ crystal grown in the $CO:CO_2$=1:3 gas atmosphere presented only one broad transition at 202 K, which does not correspond to either the 235 K Néel transition or the spin glass transition present at 175 K, but rather purely spin glass in nature based on poor oxygen stoichiometry. Specific heat data provided initial insight into the presence of charge order at 314 K. Single crystal x-ray diffraction highlighted the appearance of 2D diffuse scattering and 3D charge order peaks along the (1/3, 1/3, l) line, present in the $LuFe_2O_4$ crystals grown in $CO:CO_2$=1:3 and $CO:CO_2$=1:5 gas atmospheres, respectively.

The new understanding into the magnetism and charge order of $LuFe_2O_{4-\delta}$ and it's large sensitivity to oxygen stoichiometry has produced a surge of new interest within the remaining rare earth series. Single crystals of $YbFe_2O_{4-\delta}$ were grown in two different partial pressure oxygen environments, $CO:CO_2$=1:3 and $CO:CO_2$=1:3.5. In order to investigate the magnetism and charge order properties, macroscopic measurements of magnetization, specific heat, single crystal x-ray diffraction, ac susceptibility and Mössbauer spectroscopy were performed. To investigate the type of magnetic ordering within a $YbFe_2O_{4-\delta}$ single crystal, oriented along c, Diffuse Neutron Scattering (DNS) was performed at DNS-FRM II. Magnetization measurements of each single crystal grown in $CO:CO_2$=1:3 and $CO:CO_2$=1:3.5, provided very similar data curves with three main transition points; the main ferrimagnetic transition at 240 K, followed by a small peak at 220 K. The third largest transition present on the magnetization data appears at 150 K, finalized by a small very broad feature at 30 K. The appearance of charge order at 305 K is seen clearly in the specific heat data supported by single crystal x-ray diffraction which exhibits strong diffuse scattering along (1/3, 1/3, l) line.

To the most supportive parents; Christine and Neville.....

Acknowledgements

I would like to acknowledge the following people who were connected to both the experimental investigations and writing of this thesis, who without their help would not have been possible.

Geetha Balakrishnan, Manuel Angst and Raphael Hermann, I would like to thank you all for co-supervising this project, providing me with invaluable knowledge regarding the experimental research into the realm of multiferroics. The depth of research conducted this year, focusing on the crystal growth of such interesting compounds complimented by a full support in learning new techniques and expanding my previous knowledge in this area, enabled me to grow as a researcher. Without you all this would not have been possible and for this I am truly grateful.

Martin Lees, Oleg Petrenko and Karen Friese, I thank you for support with the necessary training on experimental instruments and software, providing me with the ability to ask questions on my research and guiding me when I reached certain obstacles along the way.

Thomas Brückel, I would like to thank you for giving me the opportunity to work in such a prestigious institute and be surrounded by a wonderful group of people in JCNS-2.

Jörg Persson, without your persistence and guidance with orientating sometimes difficult samples, I would not have been able to obtain the miraculous results I have during the course of this masters.

Yixi Su and Kirill Nemkovskiy, my time at DNS was made successful with the great support from you both, with respect to both the sample mounting and measurement time, as well as understanding and interpreting the results. I thank you greatly for this.

Barbara Köppchen and Susan Tatlock, I could not have got through this year without you both, Barbara, you have not only been a complete saint when helping me with travel and administration work, but often been a sounding board then things were going wrong. Thank you.

Joost deGroot, I do not think my time at Jülich and learning new experimental equipment and software would have gone so smoothly without your support. You guided me through each step, showing me the ropes and allowed me to gain great results with your prior knowledge in this area. Thank you.

Shilpa Adiga, Pankaj Thakuria, Thomas Müller, I am grateful that I was able to become a apart of the young investigates group and work with you all, especially our times at conferences and beam time experiments, which will stay fondly with me in my memories.

Ronnie Simon, Marcus Herlitschke, Benedikt Klobes, Paula Bauer, Tania Claudia Weber, Thank you for giving me guidance with training on experimental equipment and software as well as many chats about research in the coffee room.

Ravi Singh, Robert Cook, Tom Orton, Tom Hayes, Olga Young, Michael Smidman and Natalia Parzyk, I really enjoyed being apart of the Superconductivity and Magnetism group, you all, not only each provided me with invaluable training during the course of my masters, but you were a great group of people to work and socialize with, making me feel completely welcome and at home. Thank you.

Klaus Neumann, There are not many words that express how truly grateful I am to you. If you hadn't stood by me through my time at Loughborough university, encouraging me to keep going even when I felt like giving up, I would not be in the position I am today. You provided me with invaluable contacts and experiences in research over the last seven years, which has given me the drive and inspiration to hopefully one day become a good scientist. Thank you Klaus for everything.

Family and friends as well as the people no longer here with me, Thank you to all those you have supported me through the ups and downs,

because this year, although completely and utterly rewarding has seen it's difficulties. The five people I wish to thank are Chris, Mike and Paul who allowed me to become part of a family when living in Coventry and who I will keep close to my heart for the many years to come. I finally thank the last two people, the two most important people in my life, who have given me constant support through the good and bad times, providing me with sound advice as well as love and care to see me through.... Mum and Dad, thank you from the bottom of my heart, I hope I have made you proud because without you both I would not be the person I am today. I would also like to say a final thank you to the close people who have supported me and are no longer with us on this earth. Nan I did this for you.

Contents

List of Figures

LIST OF FIGURES

LIST OF FIGURES

List of Tables

LIST OF TABLES

1

Introduction

Magnetic and insulating materials were once thought to exhibit completely independent characteristics based on their mutually exclusive properties. However James Maxwell in 1865 postulated the existence of a class of real materials 'Multiferroics' in which spontaneous magnetic and dielectric ordering occur (1). The fascinating coupling within multiferroic materials has produced a fast breeding ground of experimental research, based on their switchable polarization: by applying an external electric field the material becomes magnetically ordered and with the application of an external magnetic field the material becomes charge ordered. Ferroelectricity itself has been put largely in to play with extensive use in memory elements, filtering devices and high-performance insulators (2). The exploitation of the interplay between electricity and magnetism may lead to large advancements in the electronic industry with the production of multifunctional memory storage devices and the development of magnetic field sensors (3)(4). The question remains: what allows for this mutually exclusive condition in magnetism and electricity within certain compounds and what are the conditions which govern the term 'multiferroicity'? The following thesis provides a detailed look at the investigation into these properties within two candidate multiferroic materials, in single crystal form.

1.1 Multiferroics

A material which exhibits more than one primary ferroic order is classed as a multiferroic material. Ferroic order is found in materials that adopt a spontaneous, switchable internal alignment, for example, the alignment of electronic spins in ferromagnetic materials and the switchability of the electric dipole moments in ferroelectric materials

(3). H. Schmid in 1994 was the first scientist to provide the term 'multiferroic' for materials which possess more than one ferroic order. His definition referred to multiferroics as single phase materials which simultaneously possess two or more primary ferroic properties (5). There are three main types of ferroic orders:

***Ferroelectricity*:** occurs in materials which have a spontaneous polarization that is stable and with the application of externally applied electric field can be switched hysteretically.

***Ferromagnetism*:** occurs in materials which have a spontaneous magnetization that is stable and with the application of an externally applied magnetic field can be switched hysteretically.

***Ferroelasticity*:** occurs in materials which display a spontaneous deformation that is stable and with applied stress can be switched hysteretically. For example applying a small strain on a multiferroic thin film which causes a structural change in the crystallographic unit cell; from a rhombohedral unit cell to monoclinic, therefore altering either the magnetic or charge order; inducing ferroelectricity.

A material that exhibits two or more of these primary ferroic properties such as ferromagnetism, ferroelectricity or ferroelasticity described above, is classed as a multiferroic. All of the primary ferroics described form small regions of order, known as domains, within the material. Domains of different orientation are separated by domain walls. With the application of an appropriate field, such as a magnetic field on a magnetic material the domains will align.

The multiferroic coupling between these three ferroic orders can be seen in figure 1.1 (6). The coupling between electricity and magnetism also known as the 'magnetoelectric effect', is, in itself a 'contraindication' (7) where magnetic and insulating materials exhibit characteristics which are mutually exclusive to each other. Most ferroelectric materials are transition metal oxides in which the transition ions have empty d shells (1). These positively charged ions (anions) form molecules with neighboring negative

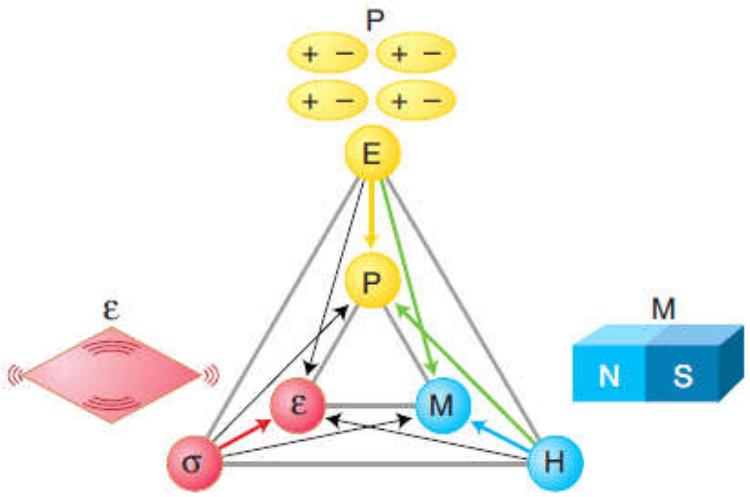

Figure 1.1: Multiferroic Triangle
Multiferroic coupling between three main single phase ferroic orders: magnetism, electricity and strain. Reproduced for Ref (6).

oxygen ions (cations). The collective shift of cations and anions inside a periodic crystal induces a bulk electric polarization, in which the mechanism of covalent bonding or electron pairing provides a virtual hopping of electrons, from one filled oxygen shell to and empty d shell of a transition metal ion. Magnetic materials, on the other hand, require a partially filled d shell, based on Hunds rule, electron spins which fully occupy the outer shell add to zero and do therefore not contribute to the magnetism.

The interplay between the magnetism and electricity was first introduced theoretically during the early 19th century with the Maxwell equations (8). It was only later during the 1960s that attempts to combine both ferromagnetic and ferroelectric properties began (9). The magnetoelectric effect describes coupling between the magnetic and electric degrees of freedom, allowing the ability to induce magnetization by an electric field and polarization by a magnetic field. The linear magnetoelectric coupling term α, which links the magnetic and electric degrees of freedom, is shown in relation of the free energy of the material and electric/magnetic field $\vec{E}/\vec{H}$ and is expanded as follows (10):

$$F(\vec{\mathbf{E}},\vec{\mathbf{H}}) = F_0 - P_i^S - M_i^S H_i - \frac{1}{2}\epsilon_0\epsilon_{ij}E_iE_j - \frac{1}{2}\mu_0\mu_{ij}H_iH_j - \alpha_{ij}E_iH_j - \frac{1}{2}\beta_{ijk}E_iH_jH_k - \frac{1}{2}\gamma_{ijk}H_iE_jE_k - ... \quad (1.1)$$

Where $\vec{E}$ and $\vec{H}$ are the electric field and magnetic field respectively. Partial differentiation with use of the epsilon tensor gives the following term for the polarization, P_i:

$$P_i(\vec{\mathbf{E}},\vec{\mathbf{H}}) = -\frac{\partial F}{\partial E_i} = P_i^S + \epsilon_0\epsilon_{ij}E_iE_j + \alpha_{ij}H_j + \frac{1}{2}\beta_{ijk}H_jH_k - \gamma_{ijk}H_iE_j - ... \quad (1.2)$$

Applying the same procedure for the magnetization, M_i, gives:

$$M_i(\vec{\mathbf{E}},\vec{\mathbf{H}}) = -\frac{\partial F}{\partial H_i} = M_i^S + \mu_0\mu_{ij}H_j + \alpha_{ij}E_i + \beta_{ijk}E_iH_j - \frac{1}{2}\gamma_{ijk}E_jEk - ... \quad (1.3)$$

Here $\vec{P^S}$ and $\vec{M^S}$ denote the spontaneous polarization and magnetization, the magnetic and electric susceptibilities are denoted by $\hat{\epsilon}$ and $\hat{\mu}$ which begin to form the linear ME effect (10). The higher-order ME effects are parameterized by the tensors β and γ. For the ME effect to exist, the cross polarization ability described in equations (1.2) and (1.3) are governed by the existence of symmetry breaking: time and spatial inversion symmetry.

The diagram shown in figure 1.2 gives three cases of time and spatial inversion operations. In the case of a ferromagnet shown in figure 1.2a, the local magnetic moment, m, in this case can be represented classically by a charge that dynamically traces an orbit, indicated by the arrow heads. A ferromagnet produces no change in the spatial inversion, but time reversal switches the charges orbit and therefore the magnetic moment, m. The second case of a ferroelectric, shown in figure 1.2b with a local dipole moment, p, can be treated as a positive point charge that lies asymmetrically within a crystallographic unit cell, with no net charge. In this instance there is no net time dependence, but spatial inversion reverses the dipole moment, p. It is clear from the first two cases of a ferromagnet and ferroelectric, that they are mutually exclusive. A ferromagnet breaks time inversion symmetry, conversely, a ferroelectric breaks spatial inversion symmetry. Therefore the final case of a multiferroic, shown in figure 1.2c

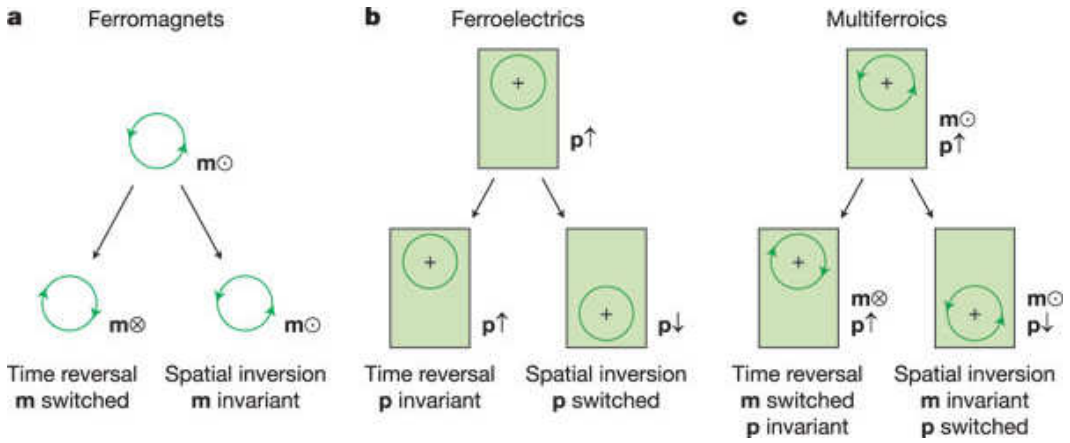

Figure 1.2: Time and Spacial Inversion Symmetry
Time and inversion symmetry breaking for (a) Ferromagnets, (b) Ferroelectrics and (c) Multiferroics. Reproduced from Ref (11).

which is both ferromagnetic and ferroelectric must break both time and spatial inversion symmetry in order to exist (11).

There is only a small group of multiferroics which exhibit magnetoelectric coupling ($\alpha \neq 0$). Not all materials which display the magnetoelectric effect are multiferroic, (figure 1.3 (12)), for it to be deemed as a multiferroic material it must break both time and inversion symmetry (12). The existence of the magnetoelectric effect is not surprising based on the strong internal electromagnetic fields which some ferromagnetic and ferroelectric materials exploit through large magnetic susceptibilities and dielectric constants.

1.1.0.1 Proper and Improper Multiferroics

There are two types of multiferroic materials: proper and improper which form the type I and type II multiferroics. The table in figure 1.4 (1) gives a description of the types of proper and improper multiferroic mechanisms and compounds which exhibit these characteristics.

To understand the difference between proper and improper multiferroic materials, the answer lies in the driving force (the primary order parameter) that leads to fer-

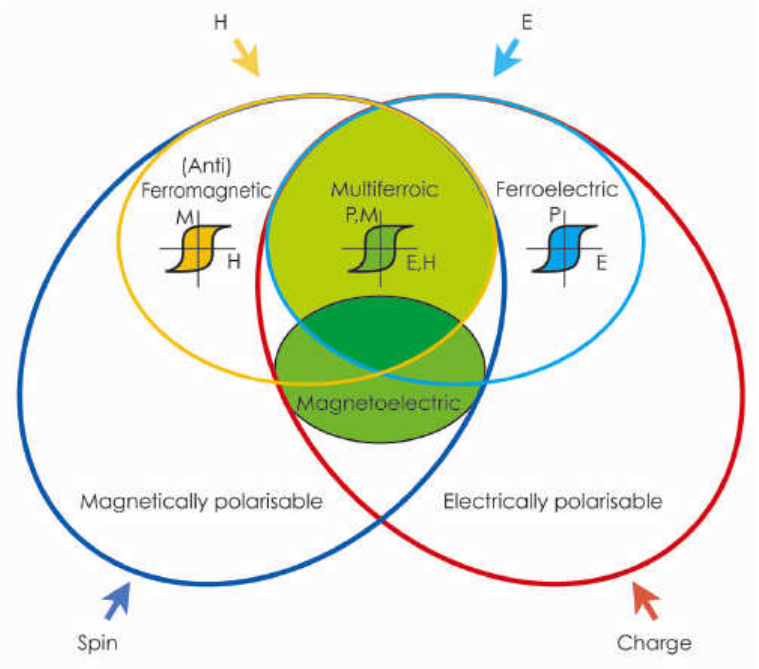

Figure 1.3: Multiferroic Coupling
Schematic of multiferroic cross over between ferroelectric and ferromagnetic materials. Reproduced from Ref (12) and adapted by ESRF.

Table 1 Classification of ferroelectrics

	Mechanism of inversion symmetry breaking	Materials
Proper	Covalent bonding between $3d^0$ transition metal (Ti) and oxygen	$BaTiO_3$
	Polarization of $6s^2$ lone pair of Bi or Pb	$BiMnO_3$, $BiFeO_3$, $Pb(Fe_{2/3}W_{1/3})O_3$
Improper	Structural transition 'Geometric ferroelectrics'	K_2SeO_4, Cs_2CdI_4 hexagonal $RMnO_3$
	Charge ordering 'Electronic ferroelectrics'	$LuFe_2O_4$
	Magnetic ordering 'Magnetic ferroelectrics'	Orthorhombic $RMnO_3$, RMn_2O_5, $CoCr_2O_4$

Figure 1.4: Classification of Mulitferroics
Table with compounds which exhibit either proper or improper multiferroicity though the specific type of ferroelectric mechanism. Reproduced from Ref (1).

roelectricity. In the case of proper ferroelectricity, the primary order parameter is ferroelectric distortion. The first example given in figure 1.4 (1) of proper ferroelectricity is $BaTiO_3$, here it is the covalent bonding between the transition metal and the oxygen which allows for a polar state. The ferroelectric distortion occurs due to the displacement of the B-site cation (Ti) with respect to the oxygen octahedral cage. Here the transition metal ion (Ti in $BaTiO_3$) requires an empty d shell, since the ferroelectric displacement occurs due to the hopping of electrons between Ti d shell and O p shell. The second origin of proper ferroelectricity is seen in $BiFeO_3$ through polarization of a $6s^2$ lone pair. In this case the A cation (Bi^{3+}) drives the displacement of the partially filled d shell on the B anion site, Fe^{3+}, contributing to the magnetism (3).

The classification of improper multiferroic materials stem from non-conventional ferroelectric induction in which electron pairing is the main driving force of the transition. Improper multiferroic materials induce ferroelectricity from some complex structural change or magnetic ordering. In geometrically frustrated multiferroics, for example, the hexagonal RMnO$_3$ system, where R=Ho-Lu,Y, the ferroelectricity is induced by a lattice transition. Below this transition temperature an electric dipole moment develops, inducing ferroelectricity (13)-(15). Ferroelectricity in charge ordered multiferroics originate from the geometric frustration of mixed valance ions positioned in a bilayer, allowing for a cross polarization inducing a ferroelectric state (16). The final type of improper ferroelectricity occurs through magnetic ordering, specifically with collinear and spin spiral magnetic structures. During a spin spiral or collinear magnetic ordering, both time and spatial inversion symmetry are broken. A prime example of this type ferroelectric mechanism is seen in the RMn$_2$O$_5$ system, where R denotes the rare earth elements Pr to Lu, Bi and Y (1). This particular compound goes through four magnetic transitions; during the second commensurate antiferromagnetic ordering at T_2=38-41 K the onset of ferroelectricity occurs, which is seen as a peak in the dielectric constant measurement (17)-(22).

1.1.0.2 Type I Multiferroics

The main focus of this thesis is the investigation of multiferroic materials which exhibit ferroelectricity through charge ordering. This particular type of multiferroic mechanism

is classed as a type I multiferroic, which does not require the existence of magnetic order to induce ferroelectricity. These types of multiferroic materials are often very good ferroelectrics, where the critical temperatures of the magnetic and ferroelectric transitions can be well above room temperature. The only issue with this particular class of multiferroic material is the coupling between magnetism and ferroelectricity is often weak (12).

Charge ordered multiferroics: Ferroelectricity within the $R\mathrm{Fe_2O_4}$ system, where *R=Y, Ho, Er, Tm, Yb* and *Lu*, stems from a result of charge ordering, where certain non-centosymmetric arrangements of ions induce ferroelectricity. In the theoretical case of $R\mathrm{Fe_2O_4}$ it is the charge transfer between the single Fe layers within the bilayer that produce a cross polarization; where one layer is more rich in Fe^{2+} and the second layer more rich in Fe^{3+}, therefore giving rise to ferroelectricity 1.5 (23).

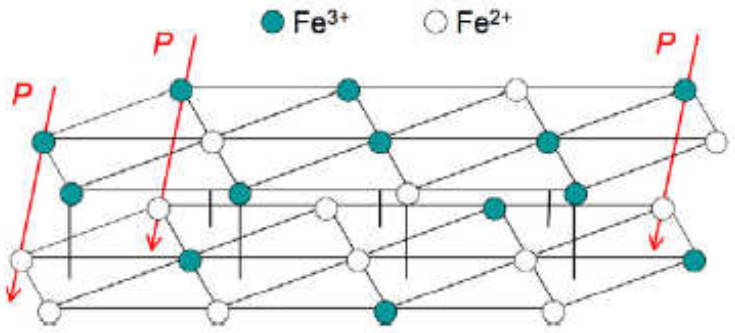

Figure 1.5: Charge Ordering Bilayers
Bilayer of $\mathrm{FeO_2}$ triangular lattice in candidate CO multiferroic $\mathrm{LuFe_2O_4}$. Red arrows indicate the direction of electric polarization. Reproduced from Ref (23).

There are different charge arrangements which induce ferroelectricity based on site centered and charge centered coupling. If we first focus on a neutral one dimensional chain of ions, with equal charge on each site shown in figure 1.6a, the first type of charge ordering which can occur is from site centering. Site centering stems from inequivalent sites, where one set of sites has charge e^- and the other e^+ (see figure 1.6b), for example sodium chloride, NaCl. This particular type of charge ordering does not break spatial inversion symmetry, and therefore does not induce ferroelectricity. An-

other type of charge ordering based on bond centering is shown in figure 1.6c (23), also known as lattice dimerization. The lattice dimerization stems from a spin Peierls magneto-elastic transition, which couples the one-dimensional electronic structure and three dimensional lattice vibrations. The origin of this coupling originates from the exchange energy of the chains, in which a distortion of the lattice influences the magnetic energy. It is this elastic distortion which occurs below a spin Peierls transition that results in a dimerization, producing two unequal alternating exchange constants (24). This type of lattice dimerization was first discovered the in $CuGeO_3$ system (25). The situation changes drastically when simultaneous site- and bond-centered CO is brought together, inversion symmetry is broken, which in this case is on each molecule and develops a net dipole moment inducing ferroelectricity, schematically shown in figure 1.6d.

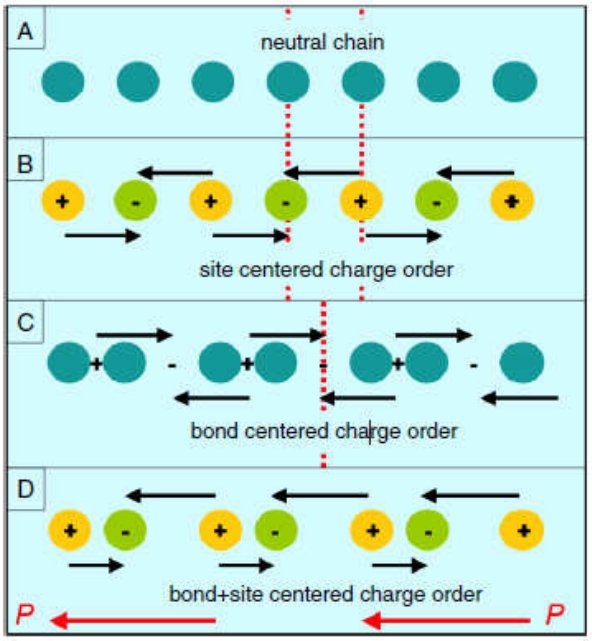

Figure 1.6: Bond-centred and Site-centered Charge Ordering
(a) One dimensional neutral chain, (b) site-centered charge ordering, (c) bond-centered charge ordering, (d) linear combination of (b) and (c) producing a ferroelectric state. Reproduced from Ref (23).

Lone pair multiferroics: As described briefly in section (1.1.0.1) a prime example of multiferroicity through electronic lone pairs is $BiFeO_3$. The Bi^{3+} 'A' cation has a stereochemically active $6s^2$ lone pair, shown in figure 1.7 (26). The A cation drives a displacement of the partially filled *d* shell on the 'B' anion site which is Fe^{3+} in the case of $BiFeO_3$ and contributes to the magnetism. The Bi^{3+} stereochemically active 6^{s2} lone pair causes the Bi 6p (empty) orbital to come closer in energy to the (oxygen) O 2p orbitals. This process leads to a hybridization between the Bi and O orbitals and drives an off-centering of cations towards neighboring anions resulting in ferroelectricity (27).

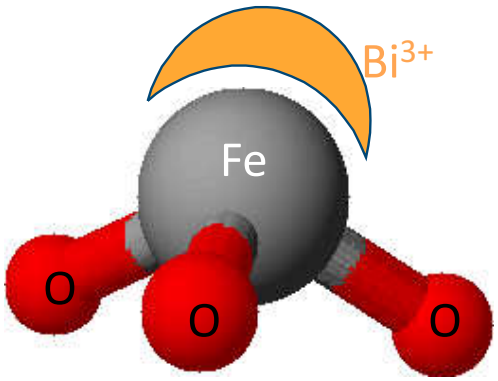

Figure 1.7: Multiferroic $BiFeO_3$ Lone Pair
Diagram of $BiFeO_3$ electronic lone pair and driven distortion between the Fe-O ligands. Reproduced from Ref (26).

Geometrically frustrated multiferroics: Materials which possess ferroelectricity from geometric frustration through atomic positioning is still under investigation. The candidate compound $YMnO_3$ has a complex structure which provides a basis for the onset of ferroelectricity through net electric polarization. The hexagonal structure of $YMnO_3$, consists of non-connected layers of MnO_5 trigonal bipyramids, corner-linked by in-plane oxygen ions which form a closed packed plane separated by a layer of Y^{3+}, shown in figure 1.8a (14). For the structure to form an energy favorable state, close packing of the MnO_5 polyhedra between the the Y^{3+} layers occurs. This 'buckling' of the MnO_3 polyhedra influence a long range dipole-dipole interaction, where rotation of oxygen atoms generate a stable ferroelectric state, see figure 1.8b (12).

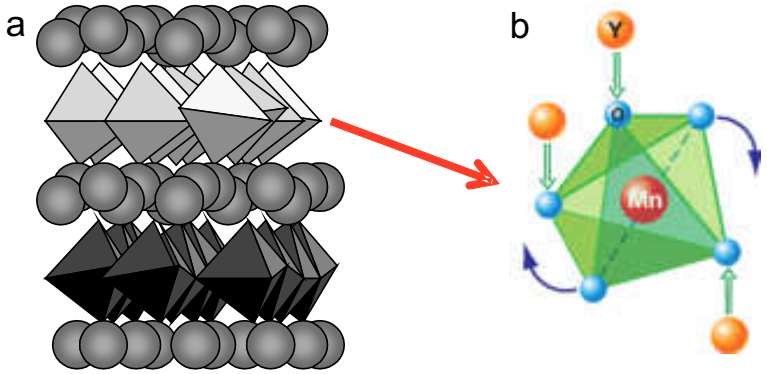

Figure 1.8: Geometrically Frustrated $YMnO_3$
(a) Unit cell of $YMnO_3$ with distorted MnO_3 octahedra between monolayers of Y^{3+}. (b) Buckled MnO_3 octahedra due to close packing Y^{3+} driving long range dipole-dipole interaction. Reproduced from Ref (12) and (14).

1.1.0.3 Type II Multiferroics

Spiral magnetic structures: Ferroelectricity induced by spiral magnetic ordering originates from an effect of exchange-stiction, which can be described as lattice relaxation in a magnetically ordered state. The exchange between the spins of a transition metal ion is, in most cases mediated by ligands (surrounding oxygen atoms, often coordinated in trigonal or octahedral arrangement). These ligands form bonds between pairs of transition metals which bring into play the Dzyaloshinskii-Moriya interaction (DM). As shown in figure 1.9, there are two transition metal ions in coordination with an oxygen bond. Based on the spin frustration within a system and the strength of the spin spiral magnetic interaction, the distance, x, denoted on figure 1.9a will increase or decrease (1). The change in x is representative of the DM interaction which pushes negative oxygen ions in one direction perpendicular to the spin chain formed by positive ions. It is this process which induces electric polarization perpendicular to the chain, and demonstrated clearly in the $RMnO_3$ system, shown in figure 1.9b.

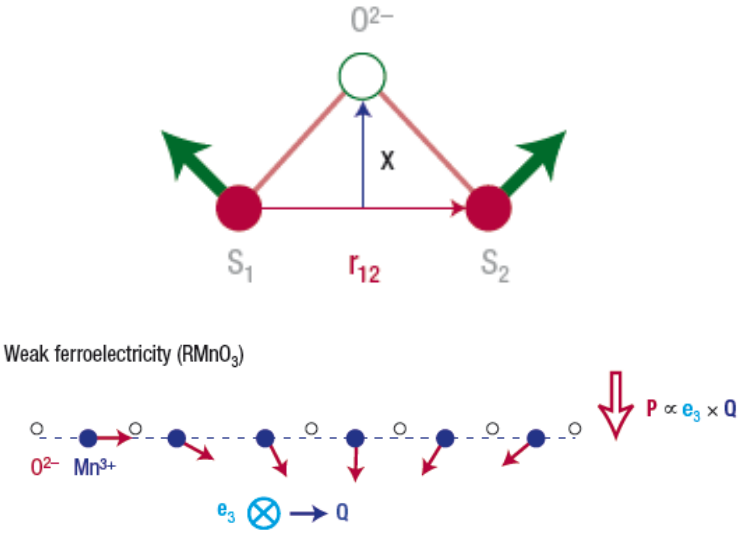

Figure 1.9: Effects of the Antisymmetric Dzaloshinskii-Moriya Interaction
(a) The interaction H_{DM}=$\mathbf{D}_{12} \cdot [\mathbf{S}_1 \times \mathbf{S}_2]$, where the DM vector D_{12} is proportional to the spin-orbit coupling constant λ, and depends on the position of the oxygen ion (open circle) between two magnetic transition metal ions (filled circles), $\mathbf{D}_{12} \propto \lambda \mathbf{x} \times r_{\hat{12}}$. (b) Weak ferromagnetism in spin spiral magnetic structures, brought on by the DM interaction. Reproduced from Ref (1).

Collinear magnetic structures: Collinear magnetic structures originate from the existence of frustrated Ising spins with a ground state spin coordination ↑↑↓↓. This competing nearest neighbor ferromagnetic and next-nearest neighbor antiferromagnetism is shown clearly in figure 1.10 (1). This specific type of magnetic ordering leads to the breaking of inversion symmetry through alternate charges of magnetic ions and oxygen octahedra on magnetic sites, which induce electric polarization. A prime example of this magnetic order is seen in YMn_2O_5 (28).

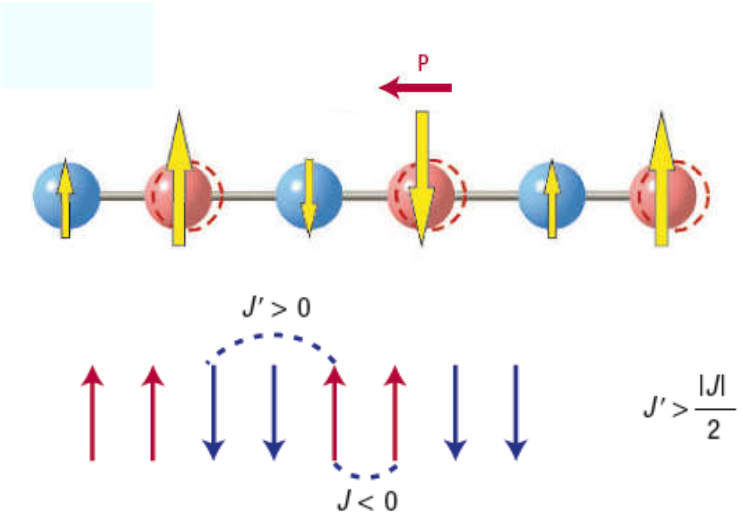

Figure 1.10: Collinear Magnetic Ordering
(a) Polarization induced by coexisting site-centered charge and collinear magnetic ordering. (b) Collinear chain of Ising spins: $\sigma_n = \pm 1/2$, with nearest-neighbor ferromagnetic and next nearest neighbor antiferromagnetic coupling. Reproduced from Ref (1).

1.2 RFe_2O_4 System

Crystals with the structure $R\mathrm{Fe_2O_4}$, where R=Y, Ho, Er, Tm, Yb and Lu belong to the the rhombohedral structure, with space group R$\bar{3}$m. The system is commonly described as an alternate stacking of triangular lattices of R, Fe and O along the c axis. The crystallographic unit cell can be separated in to two sections a W and T layer, consisting of $\mathrm{Fe_2O_{2.5}}$ bilayers separated by $R\mathrm{O_{1.5}}$ monolayers, respectively, shown in figure 1.11 (29). The coordination of the Fe and O in each W bilayer form two triangular lattices of Fe^{2+} and Fe^{3+} with five fold oxygen coordination, resulting in a triangular bipyramid structure. The T layers separate the W bilayers with a single triangular lattice of rare earth and oxygen ions, forming distorted oxygen octahedra (30).

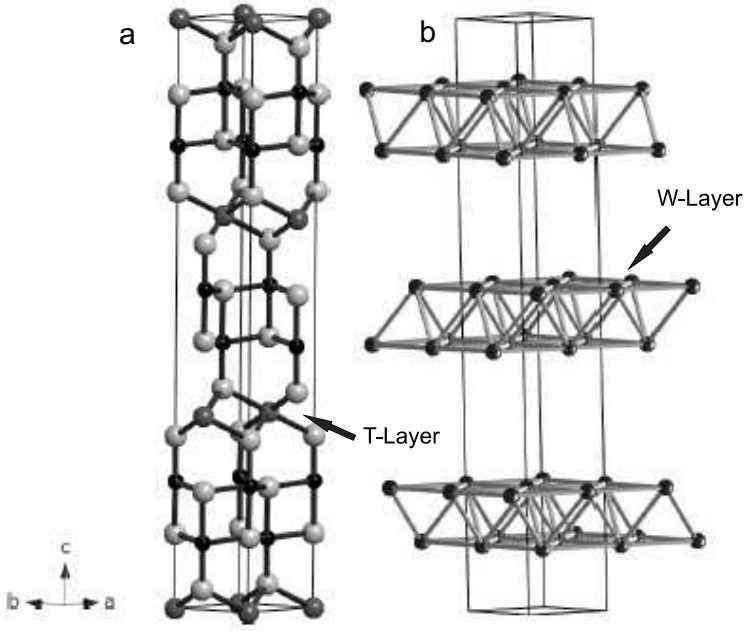

Figure 1.11: Crystal Structure of $R\mathrm{Fe_2O_4}$
(a) Unit cell of $R\mathrm{Fe_2O_4}$ with R atoms (dark grey circles), Fe atoms (black circles) and O atoms (white circles) positioned in triangular layers along the c axis. (b) Shows Fe bilayer coordination within unit cell, denoted by W-layer. Reproduced from Ref (29) and adapted.

This system is particularly interesting based on the $R\mathrm{Fe_2O_4}$ chemical formula and the occurrence of a mixed valance state:

$$LuFe_2O_4 = Lu^{3+} + Fe^{2.5+} + O^{8-} = 0 \tag{1.4}$$

From the deduction shown in equation (1.4) it is clear that in order to balance the oxidation state of this compound the average valance of the Fe ions must be $Fe^{2.5+}$. This cannot be the case in reality as there is no half electron state. The necessity for a half valance state to balance the overall oxidation state of the system, implies that the system must contain both Fe^{2+} and Fe^{3+} ions, as mentioned previously. The result of the mixed valency infers that the two Fe valance states occupy equivalent Fe sites on the hexagonal net plane with an equal probability when averaged out, shown in figure 1.12 (31).

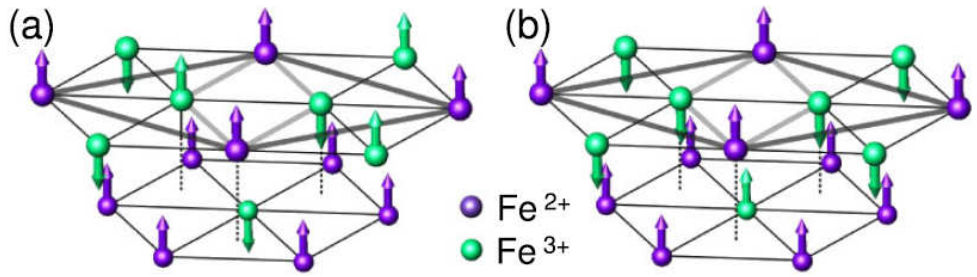

Figure 1.12: Fe Bilayers
Parallel Fe^{3+} spin in (a) Fe^{3+} rich bilayer and (b) Fe^{2+} rich bilayer. Reproduced from Ref (31).

The nature of the $R Fe_2O_4$ structure type and the Fe^{2+} and Fe^{3+} bilayers separated by monolayers of Lu atoms, ultimately produce a spin and charge coupling which is stronger in the a-b plane than along the c axis. The result of this arrangement forms an anisotropic ordering process of the spin and charges (30). The magnetic anisotropy originates from inter magnetic dipole-dipole interaction, the shape of the crystals and spin orbit coupling (24). The arrangement of Fe^{2+} and Fe^{3+} ions within each of the bilayers form a charge frustrated triangular arrangement, see figure 1.13 (32). The neighboring atoms within each triangular lattice have a negative exchange, one up spin, S=1/2, and one down spin, S=-1/2, which pair according to Hunds rule (24). In this system only two of the three spins can be simultaneously aligned antiparallel on the triangular lattice, the third spin can take either an up or down spin configuration.

The effect of this spin coordination forces a geometric magnetic frustration with the two neighboring antiparallel spins. In such a frustrated spin arrangement there is no unique ground state but a variety of low energy states in which the non-minimization energy is shared, leading to a degenerate ground state (33).

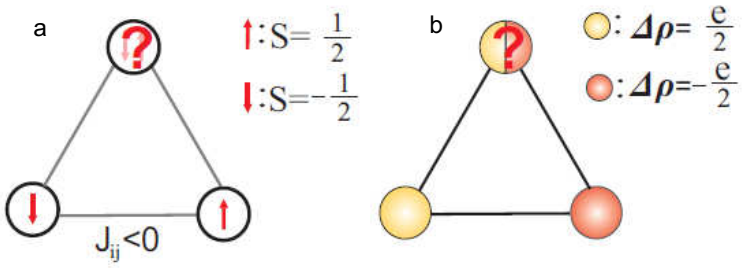

Figure 1.13: Geometric Spin Frustration
(a) Spin frustration on triangle lattice. (b) Charge order frustration (denoted by $\Delta\rho$) of 2D hexagonal lattice. Reproduced from Ref (33) and adapted by (32).

The charge order within this system stems from a resultant effect of both charge frustration with the arrangement of Fe ions and Fe^{2+} and Fe^{3+} enriched monolayers producing a cross polarization between the bilayer, resulting in a ferroelectric state.

1.2.1 Effects of Stoichiometry

During the many years of investigation into the RFe$_2$O$_4$ series, there have been a multitude of puzzling results regarding the type of magnetic and charge ordering effects observed. During synthesis and crystal growth of the RFe$_2$O$_4$ system, the use of a partial pressure oxygen atmosphere is needed to provide the mixed Fe^{2+} and Fe^{3+} valance state. This process makes this series of compounds extremely sensitive to oxygen stoichiometry, where even slight changes in the oxygen deficiency can produce a large difference in the magnetic and charge order behavior. Another factor which can effect the oxygen stoichiometry within a single crystal growth is the type of crystal growth furnace used. Floating zone furnaces come in two specific forms: a four mirror furnace and a two mirror furnace. A two mirror furnace with two halogen lamps, provides a more focused heat distribution at two parts of the polycrystalline rod: left and right. As a result, the light energy which is reflected onto the feed and seed rod which turn

counter clockwise to each other, (refer to section 2.2) is distributed more evenly. The four mirror furnace with a concentration of four halogen lamps can cause slight inconsistencies with heat distribution on the feed and seed rod, where some parts of the molten zone may be at a slightly higher temperature than the rest of the zone. This can effectively cause changes in the stoichiometry of the crystal, particularly with the evaporation of oxygen within the stoichiometric polycrystalline rod. This effect alone can cause a notable difference in the macroscopic characteristics, with sample to sample dependence within one single crystal growth. The first initial realization of stoichiometric effects within the $R Fe_2O_4$ system came from the intense studies of YFe_2O_4.

1.2.1.1 $YFe_2O_{4-\delta}$

In 1975 $YFe_2O_{4-\delta}$ was found as a new phase within the Fe-Fe_2O_3-Y_2O_3 system (34). Through x-ray diffraction and thermogravimetric measurements a phase diagram of the Fe-Fe_2O_3-Y_2O_3 at 1200°C was established, see figure 1.14a. It was at this point, the evidence of off-stoichiometric forms of $YFe_2O_{4-\delta}$ were uncovered. Further investigation into the heating effects during synthesis in 2004 produced a phase diagram of the Y-Fe-O system at 1100°C. This small reduction in temperature to 1100°C renders the $YbFe_2O_4$ completely absent, and is clearly shown in figure 1.14b (35).

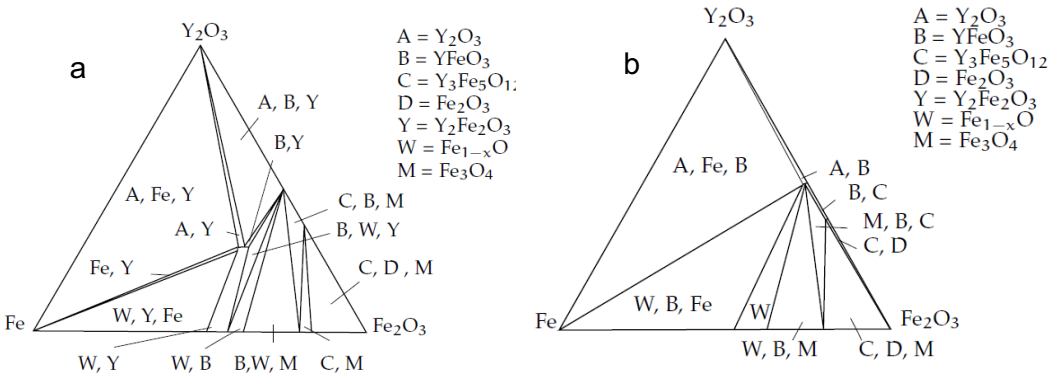

Figure 1.14: YFe_2O_4 Phase Diagrams
(a) Phase diagram of Fe-Fe_2O_3-Y_2O_3 at 1200°C. (b) Phase diagram of Fe-Fe_2O_3-Y_2O_3 at 1100°C. Reproduced from Ref (34) and (35).

The first single crystal of $YFe_2O_{4-\delta}$ was grown in 1976 (36), and has been fully studied by Mössbauer, neutron diffraction and importantly magnetization (37). Magnetization measurements with an externally applied magnetic field of 9.5 T is shown in figure 1.15.

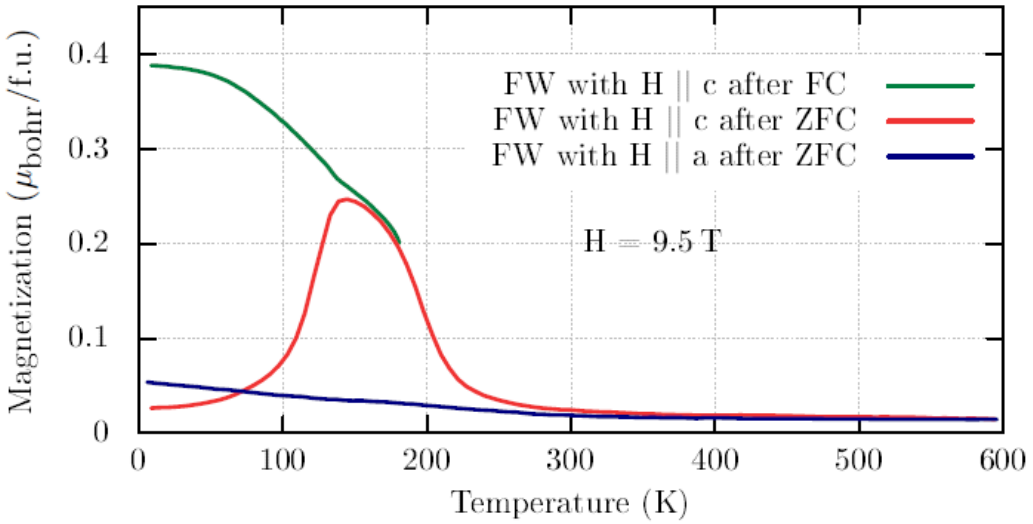

Figure 1.15: Magnetization of First $YFe_2O_{4-\delta}$ Single Crystal
Magnetization data of non-stoichiometric $YFe_2O_{4-\delta}$ single crystal. Data taken from Ref (36) and adapted by (37).

On measuring the ZFC magnetization the appearance of one broad transition peak at 150 K with a maximum magnetization of 2.4 μ_B/f.u was recorded and later described as parasitic ferromagnetism (38). The magnetization past 150 K drops steeply and levels off at approximately 270 K. Interestingly, the FC data exhibits identical behavior on cooling to 150 K but on further cooling the magnetization increases to a maximum at approximately 0.39 μ_B/f.u.

It was slightly later in the development period of $YFe_2O_{4-\delta}$ single crystals that magnetization measurements provided a detailed insight into the crystal quality, more specifically the off-stoichiometry of each crystal. The experimentation with oxygen deficiency was essential to understand the effects it has on the the magnetic and electrical properties. It was clearly shown in figure 1.14b that by reducing the synthesis

temperature by 100°C, $YFe_2O_{4-\delta}$ was no longer present. Therefore subsequent powder synthesis of $YFe_2O_{4-\delta}$ at 1200°C in varying oxygen partial pressure environments were performed (39). Figure 1.16 shows the magnetization data for three different polycrystalline samples synthesized with oxygen deficiencies of δ=+0.040, δ=+0.031 and stoichiometric $YFe_2O_{4-\delta}$ with δ=0.000. It is immediately clear that the stoichiometric $YFe_2O_{4-\delta}$ has a much sharper transition with a magnetization twice as large as that of the oxygen deficient samples, with particular reference to that with δ=+0.040. The appearance of a second smaller transition at approximately 225 K, later seen as 2D magnetic order through Transmission Electron Microscopy (TEM) (40), is much more profound in the stoichiometric sample, compared to that of the off-stoichiometric sample.

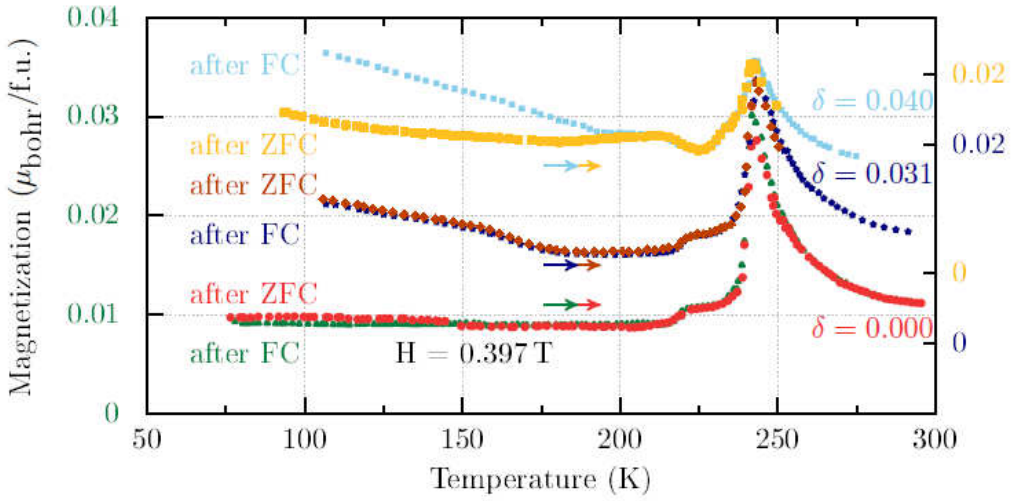

Figure 1.16: Magnetization curves of Polycrystalline $YFe_2O_{4-\delta}$
$YFe_2O_{4-\delta}$ polycrystalline samples synthesized in various oxygen partial pressure atmospheres, the upper four curves are shifted by 0.007 μ_B/f.u and 0.014 μ_B/f.u for clarity. Data taken from (39) and adapted by (37).

1.2.1.2 $LuFe_2O_{4-\delta}$

Due to the extensive progress made with $YFe_2O_{4-\delta}$ and controlling the oxygen partial pressure resulted in a regained interest within the remaining rare earth series. Early polycrystalline synthesis by Iida *et al.* (41) of stoichiometric and off-stoichiometric $LuFe_2O_{4-\delta}$ samples lead to the discovery that polycrystalline samples with an oxygen deficiency of δ=0.00-0.065 did not show the Verway transition. This is very different compared with $YFe_2O_{4-\delta}$, where stoichiometric δ=0.000 produced clear evidence of the Verway transition at 200 K and was not observed in oxygen deficient samples (δ=0.005).

The first clear magnetization data was first presented in 1986 by Iida *et al.* (41), with a polycrystalline sample of $LuFe_2O_{3.986}$. A clear observation between high and low field magnetization indicated that transition peaks smear out at relatively low fields, in this case 4.5 kOe, shown in figure 1.17, exhibited a distinct broadening of the transition at ∼190 K compared to the magnetization data taken at 105 Oe (see figure 1.17).

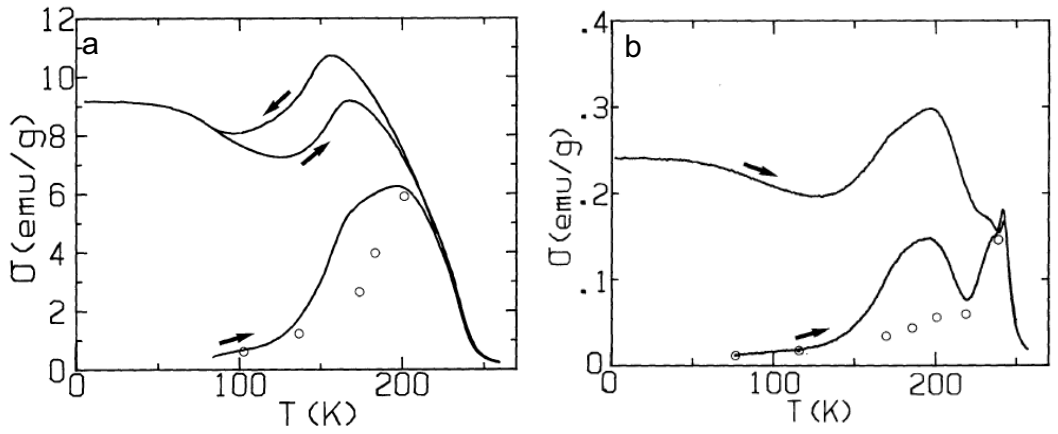

Figure 1.17: Magnetization of $LuFe_2O_4$ Single Crystal
(a) Magnetization data taken FC-FW-ZFC with an applied field 4.5 kOe. (b) Magnetization data measured with an applied field of 105 Oe for the upper and lower curve show FC-FW in 105 Oe, circles represent ZFC data. Reproduced from Ref (41).

It is clear that $LuFe_2O_{4-\delta}$ and $YFe_2O_{4-\delta}$ have very different pre-requisites for producing broad or sharp transitions in magnetization data. $YFe_2O_{4-\delta}$ must be stoichiometric (δ=0) in order to exhibit the two main transitions at 250 K and 225 K, however

$LuFe_2O_{4-\delta}$ must be oxygen deficient to gain an insight into the transitions at 230 K and 175 K.

A detailed stoichiometric study of $LuFe_2O_{4-\delta}$ was performed much later in 2009 by Ikeda *et al.* (42) which provided a better insight into the oxygen partial pressure environments required to produce oxygen varying samples.

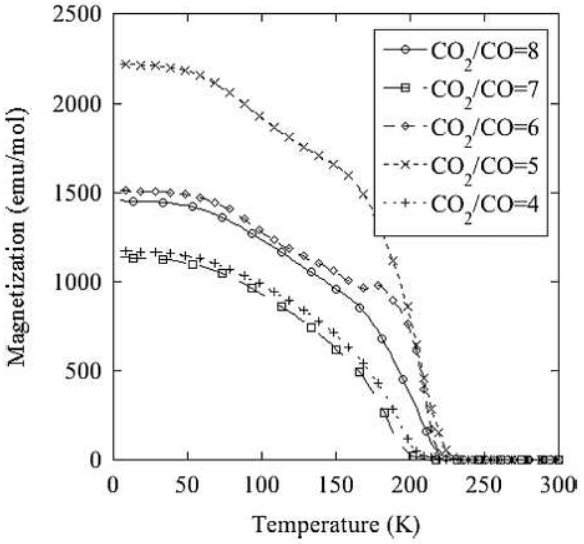

Figure 1.18: Stoichiometric Study of $LuFe_2O_{4-\delta}$
Temperature dependence of the thermo-remanent magnetization of crystals grown in different oxygen partial pressure atmospheres. The sample was cooled to base temperature in an applied field of 1 kOe and heated in zero magnetic field. Reproduced from Ref (42).

The data in figure 1.18 shows the temperature dependence of the thermo-remanent magnetization of single crystals grown in different oxygen partial pressures, and provides an initial insight into the existence of spin glass transitions. The data was taken by cooling the sample in a magnetic field of 1 kOe and measuring on warming from base temperature in zero field. It is evident that there is a fine point between atmospheres which are both highly reducing and highly oxidizing, based on the curves measured with the crystals grown in $CO:CO_2$=1:8 and $CO:CO_2$=1:4 gas atmospheres. The crystal grown in $CO:CO_2$=1:4 exhibits a broad transition over the temperature range 200 K to base temperature and no real transition points. The more oxygen deficient sample grown in the $CO:CO_2$=1:8 has a smeared out transition at approximately 150 K

which is shifted from the 175 K transition seen in the figure 1.17 magnetization data. The crystal grown in the $CO:CO_2$=1:6 provides the closest value to the optimal gas ratio and exhibits a sharper peak at the 175 K transition as well as the ferrimagnetic transition at 230 K.

In section (3) of this thesis, the investigations into magnetization, specific heat and single crystal x-ray diffraction of $LuFe_2O_4$ single crystals, grown in $CO:CO_2$=1:3 and $CO:CO_2$=1:5 gas atmospheres will be discussed, along with a detailed comparison to that of recently published results to provide a new understanding into stoichiometry and its effects on macroscopic characteristics.

1.2.1.3 $YbFe_2O_{4-\delta}$

The considerable focus on YFe_2O_4 and $LuFe_2O_4$ have lead to a better understanding of stoichiometric effects within the rare earth series. Despite early investigations into $YbFe_2O_4$, a thorough look at the effects of oxygen deficient $YbFe_2O_{4-\delta}$ have yet to be uncovered. The first synthesis and crystal growth of $YbFe_2O_{4-\delta}$ was performed in 1974 by Kimizuka *et al.* (43). Using an oxygen partial pressure of H_2:CO_2=1:2 and heating initially to 1450°C, the powder was then cooled slowly to 1350°C at a cooling rate of 0.5°C. The powder was then equilibrated to 1200°C for two days before quenching to ice temperature, where the formation of platelet crystals of $YbFe_2O_{4-\delta}$ were obtained. Shortly after the successful synthesis of $YbFe_2O_4$, an accurate phase diagram was obtained for Fe-Fe_2O_3-Yb_2O_3 to determine the standard free energy of $YbFe_2O_4$, $Yb_2Fe_3O_7$, $YbFeO_3$ and $Yb_3Fe_5O_{12}$ at 1200°C (44), shown in figure 1.19.

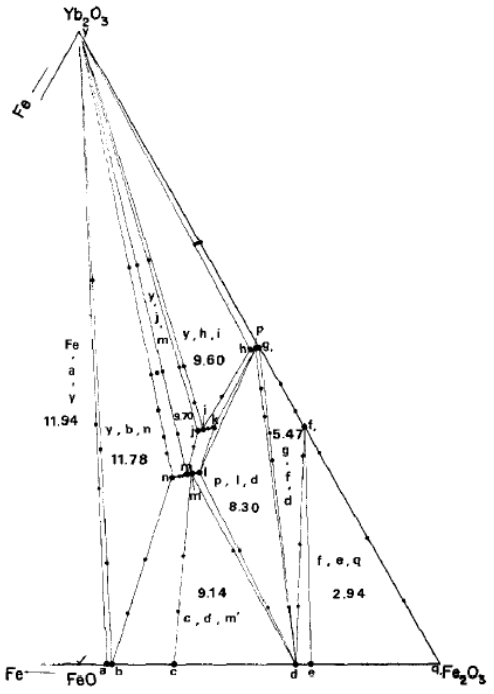

Figure 1.19: $YbFe_2O_{4-\delta}$ Phase Diagram
Phase diagram of Fe-Fe_2O_3-Yb_2O_3 system at 1200 °C. Reproduced from Ref (44).

Experimentation with various oxygen partial pressure came much later in 1982, with

polycrystalline samples of $YbFe_2O_{4-x}$, with x=-0.0027, -0.003 and 0.015 (45). For each of the polycrystalline samples, the temperature dependence of the magnetization was measured during heating in a field H, after being cooled from room temperature to 77 K with and without an applied field of H=205 kOe, (see figure 1.20 (45)). By applying H=20.5 k Oe, on both cooling and heating a small feature at 260 K is present. On further cooling the magnetization increases to a maximum of 20 emu at 77 K when x= +0.015 and ∼18 emu and 15 emu for the oxygen deficient samples x=-0.003 and x=-0.027, respectively. The thermo-remanent magnetization (denoted as H_{cool}=0) shows very different behavior. The three curves show two transitions, the small feature at 260 K and a large transition at 175 K. The sample with excess oxygen, x=+0.015, exhibits the highest magnetization of ∼13 emu before decreasing to 7 emu at 77 K. Interestingly, the oxygen deficient samples, where x=-0.003 and x=-0.027 have a slightly sharper transition but lower maximum magnetization, respectively.

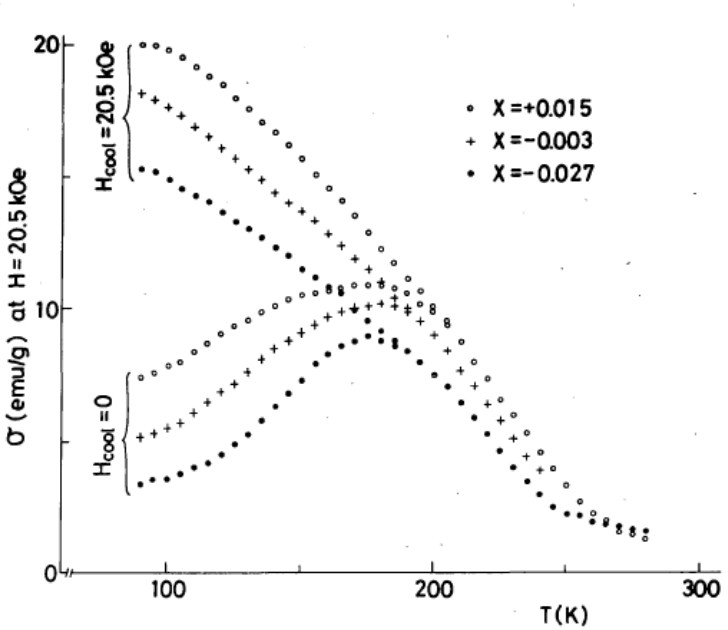

Figure 1.20: Magentization Curves of $YbFe_2O_{4-\delta}$
Temperature dependence of magnetization for three $YbFe_2O_{4-\delta}$ polycrystalline samples with different oxygen stoichiometry. The upper curves were measured with an applied field of 20.5 kOe on both cooling and heating, the lower set of curves were cooled in an applied field of 20.5 kOe and measured in zero field upon warming. Reproduced from Ref (45).

Amongst Mössbauer spectroscopy (46) and high field magnetization measurements in 1989 (47), the development in the understanding of $YbFe_2O_{4-\delta}$, under varying stoichiometric conditions came to a stand still. Much later in 2007, new studies were performed by Yoshii *et al.* investigating the magnetic and dielectric properties of polycrystalline $YbFe_2O_4$ (48). A detailed study later that year by Murakami *et al.*, focused on the origin of CO and provided evidence of a charge-ordered domain structure in $YbFe_2O_{4-\delta}$ with TEM (49). It was this investigation which prompted Hearmon *et al.* (50), to further investigate the type of CO present within $YbFe_2O_{4-\delta}$ with high energy x-ray diffraction at the beamline I19 at the Diamond Light Source.

Section (4) provides a more detailed look at the varying macroscopic results obtained from crystals $YbFe_2O_4$ grown in three different oxygen partial pressure atmospheres $CO:CO_2$=1:3 and $CO:CO_2$=1:3.5 and $CO:CO_2$=1:5, as well as a comparison to that of recently published data.

2

Experimental Methods

During the course of this study several types of experimental procedures were used to investigate the magnetic and CO properties of $LuFe_2O_{4-\delta}$ and $YbFe_2O_{4-\delta}$. The following chapter will give a brief overview of each experimental methodology.

2.1 Sample Preparation

Polycrystalline samples of $YbFe_2O_{4-\delta}$ were prepared by solid state reaction from high purity powders. The individual stoichiometric quantities were mixed and ground thoroughly before being heated in a tube furnace. The powders were heated in an oxygen partial pressure atmosphere twice, the first heating for 48 hours and the second heating period for 24 hours at 1200 ° C. Between heating stages the powder was reground to aid solid-state synthesis. The powder mixtures were then compressed into rods ranging from 6-8 cm in length via isostatic compression, where the loose powder mixture was packed into a waterproof balloon manually, in stages using a flat ended plastic rod. Once all the powder was in the balloon, it was sealed tightly with two knots and placed into a press and compressed isostatically in water at high pressure >150 kg/cm^2 to form rods for single crystal growth. The rods were then sintered for 12 or 24 h in the same gas ratio and temperature as the initial synthesis.

2.2 Crystal Growth

Single crystals of $YbFe_2O_{4-\delta}$ were grown via floating zone method using a Crystal Systems Inc. F-ZT-10000-H-IV-VPS four mirror furnace, see figure 2.1a. This method of crystal growth requires two polycrystalline rods; one feed rod roughly 6-10 cm long,

and a seed rod around 1-2 cm long. The seed rod is fixed at the bottom of the crystal growth shaft with nickel chrome wire and the feed rod is suspended above it with platinum wire. The platinum wire is used based on its physical properties: it is inert and has a high melting point of 1768 ° C, to avoid contaminating the crystal growth. The wire suspension of the feed rod on the upper shaft allows for accurate positioning above the seed rod. A thick quartz tube is then inserted into the crystal growth area and tightly sealed, this enables the use of specific gas environments in which the crystal must be grown, see figure 2.1b.

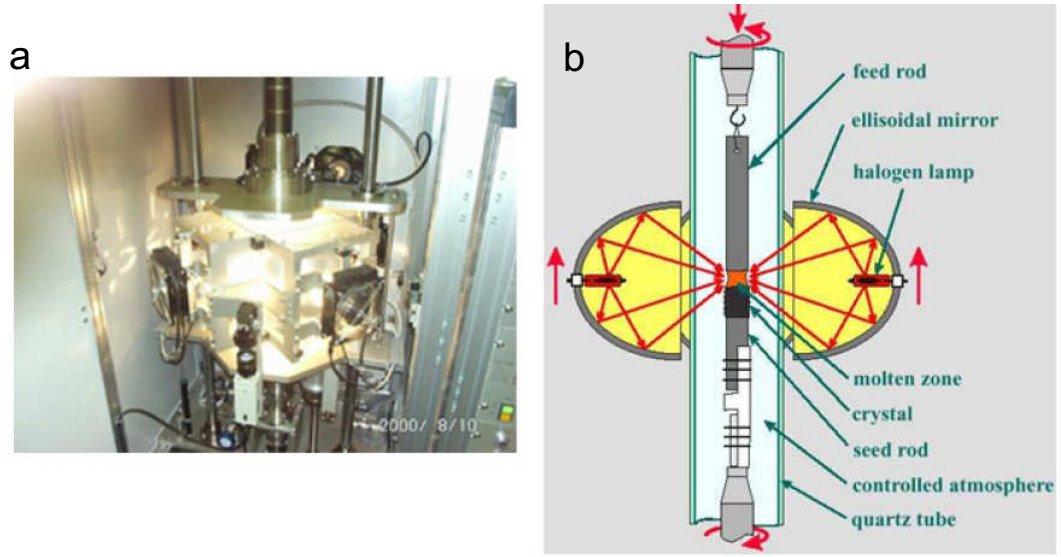

Figure 2.1: Mirror Furnace Composition
(a) Image of four mirror furnace used for $YbFe_2O_4$ crystal growth. (b) Schematic view of crystal growth set-up.

A molten zone between the feed and seed rod is created by the heat from the four halogen lamps around the quartz tube at right angles to each other. The heat is focused by the four mirrors which completely encloses the quartz tube and creates a molten zone between the two rods. The temperature is controlled by the power input of the lamps and the zone stability is maintained via power input and zone length; the latter can be altered by moving the upper shaft up or down. To allow for a homogenous distribution of heat in the molten zone, both the upper and lower shaft rotate in opposite directions to each other, see figure 2.2. As the lamps move up the shaft, the focus of the molten zone is passed through the feed rod and the material left behind cools onto the seed

rod. The rate at which the lamps move up the feed rod is variable for each compound, where some crystal growths require a very fast growth of 10 mm/h and others 1 mm/h. The pressure of the gas atmosphere in the quartz tube can be finely tuned for each crystal growth with a maximum pressure of 10 bars.

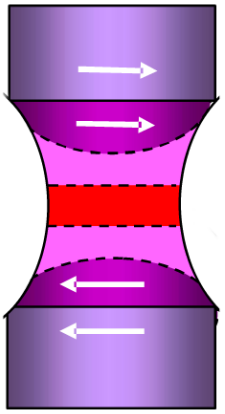

Figure 2.2: Molten Zone
Molten zone area with stable centre; produced by upper and lower shaft counter rotation.

2.3 X-ray Diffraction

In order to investigate the phase purity during powder synthesis and any structural changes of single crystal $YbFe_2O_{4-\delta}$ it was essential to use the following x-ray techniques.

2.3.1 Powder X-ray Diffraction

The phase purity during each stage of synthesis was determined by powder x-ray diffraction. During the powder synthesis, a powder diffraction was taken after the 2nd heating to check the phase purity and formation of the compound. The powder diffraction patterns obtained were compared with already published data of the required final compound and also those of different stoichiometric ratios of the primary starting elements, to check for phase impurity. Powder x-ray diffraction is a powerful tool to probe the atomic structure, it uses the simple principle of Braggs law.

$$n\lambda = 2d\sin\theta \tag{2.1}$$

The incident beam of x-rays with wavelength λ hit the surface of the crystalline material at an angle θ and are then scattered at an angle dependent on the number of wavelengths n and the spacing d between the atomic layers, see figure 2.3 (51).

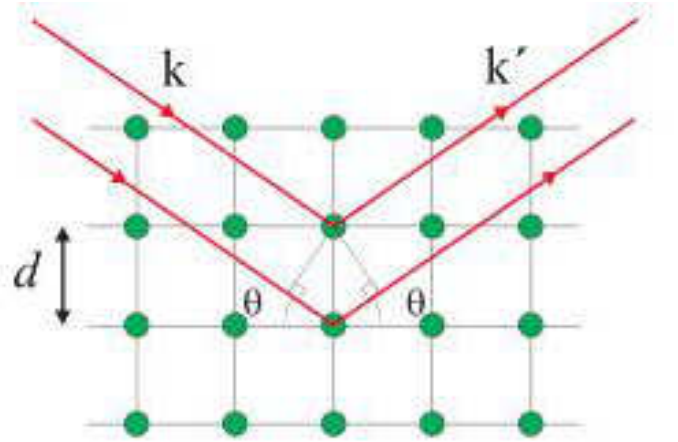

Figure 2.3: Bragg Condition
Schematic of Bragg condition between lattice planes, where κ and κ' are the incident and reflected wave vectors, respectively. Reproduced from Ref (51).

Three x-ray diffractometers were used for the powder x-rays patterns presented in this thesis: Philips PW1720 X-ray diffractometer, Bruker D5005 and Huber Guinier G670 which all use CuK$_{alpha}$, with λ=1.5418 Å.

In order to refine the phase purity and lattice parameters of powder diffraction patterns a readily available program *Fullprof* was used. *Fullprof* uses a Rietveld method for powder refinement (the refinement of magnetic structures can also be achieved with this method) which uses the original data from the x-ray measurement and compares it to a calculated fit. This calculated fit is determined from already refined lattice parameters from crystallographic databases, which give a good estimation of where all the Bragg reflections should be when processing the observed data. To run a refinement, both calculated and observed information are prerequisite; then by gradually opening various parameters which affect the shape of the diffraction pattern and lattice parameters, a close match between the observed and calculated pattern can be obtained. This is an important process as depending on the compound of interest, the lattice

parameters may alter at certain temperatures due to a structural transition (magnetostructural) and this is one way in which to determine the changes in structure and search for impurity phases.

2.3.2 Laue Diffraction

The sample quality and crystallographic orientation of each crystal was determined by Laue diffraction. The crystal is placed on a triple-axis goniometer and positioned within the diffractometer: A beam of *white* x-rays are incident on the crystal sample from the centre of the scintillator. The wide range of wavelengths are then back scattered onto a screen, shown in figure 2.4 (52). The image is then recorded on a charged-coupled device which is controlled by image pro software.

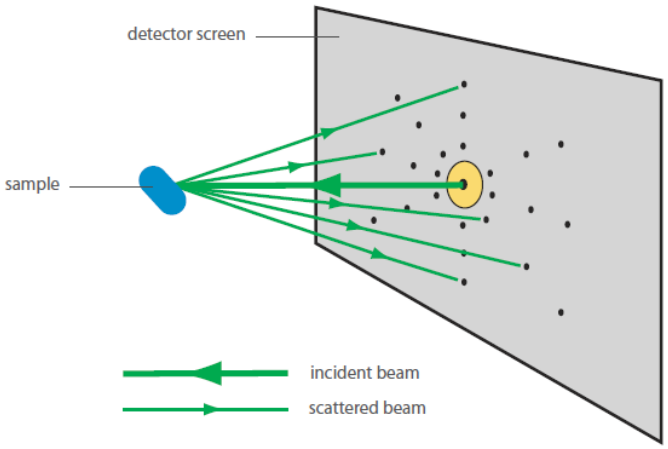

Figure 2.4: Laue Diffraction
Diagram of Laue camera showing incident white x-rays on sample with back scattered intensities on the detector screen. Image taken from reference (52).

The images obtained from the Laue camera can then be compared to simulated patterns using *OrientExpress* software. By moving the crystal according to the simulated pattern, exact orientations along each crystallographic axis can be obtained. Once an area with a consistent pattern has been isolated the crystal is cut along the plane normal to the required axis using a low speed diamond saw.

2.3.3 Single Crystal X-ray Diffraction

In order to gain a more detailed insight into the crystallographic structure and charge order at different temperatures, single crystal x-ray diffraction is essential. A Supernova dual source diffractometer was used for all single crystal diffraction measurements, see figure 2.5a (32). The dual source is equipped with two micro source x-ray tubes for the option of two x-ray radiation wavelengths; molybdenum (λ_{Mo}=0.709 Å) and copper (λ_{Cu}=1.540 Å). The scattered x-ray beam is collected on a high sensitivity Atlas area Charged Coupled Device (CCD) detector. To measure a range of temperatures, a Cryojet cooled with nitrogen gas with an obtainable temperature range of 100 to 490 K can be used.

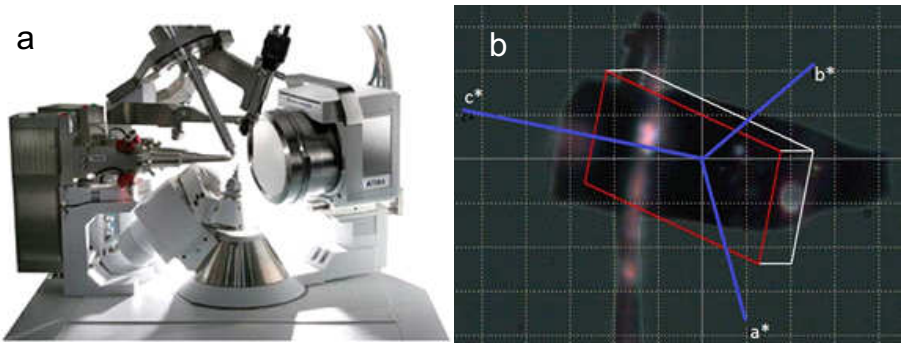

Figure 2.5: Single Crystal X-Ray Diffraction
(a) Oxford Diffraction Supernova diffractometer. (b) Orientated crystal of $YbFe_2O_4$ on sample holder. (a) reproduced from Ref (32).

The instrumental software CrysAlis^{Pro} is used to orientate the crystal shown in figure 2.5b, run the experiment and analyze the data. Before running a long experiment to capture all the observed reflections from the CCD, a short experiment of 5 minutes is used to check the crystal quality and lattice parameters. Usually the parameters will need altering depending on the crystal system and is done by entering the crystallograpic lattice parameters from a known database, for example the ICSD (international Crystallograpic Database). Once the correct structure has been determined a full measurement can be programmed for one or a series of temperatures.

2.4 Magnetization

The magnetization measurements performed on both $LuFe_2O_{4-\delta}$ and $YbFe_2O_{4-\delta}$ were conducted on two different magnetometery measurement systems, an MPMS (Magnetic Properties Measurement System) and a CCMS (Cryo Cool Measurement System) using the VSM (Vibrating Sample Magnetometer) option which will be described in the following two subsections.

2.4.1 MPMS (Magnetic Properties Measurement System)

The MPMS uses a SQUID (Superconducting Quantum Interference Device) magnetometer to measure the magnetic response of the sample in a temperature range of 1.85 to 400 K. The advantage of using a SQUID magnetometer for certain measurements is it's great sensitivity to low magnetic fields based on it's composition. The SQUID superconducting chip consists of two superconductors separated by thin insulating layers which form two parallel Josephson junctions. These parallel Joseph junctions create an indefinite current flow without any applied voltage, known as the Josephson effect. The SQUID is attached to the pick-up coils which is positioned inside the superconducting magnet. The sample is then mounted in such a way that it lies within the pick-up coils of the SQUID, see figure 2.6 (52). The sample is glued with GE (General Electric) varnish to a non-magnetic Tufnol sample holder. The GE varnish can be easily removed with the use of acetone for reorientation of the sample or complete removal from the holder. The magnetic response of the sample is then determined by the SQUID magnetometer which measures the current generated in the pick-up coils by the moving the sample in a series of 32 steps. The current is induced by the magnetic moment of the sample. Before starting a measurement the system is degaussed: a small program is written which applies positive and negative fields ranging from the maximum field to the lowest field and then to zero to remove any remnant field from a previous measurement. This is specifically important with samples very sensitive to small applied fields. Measurements in the Zero Field Cooled (ZFC) mode ranging from 10 to 300 K and Field Cooled (FC) mode ranging from 300 to 10 K was collected for both single crystal samples.

The SQUID magnetometer used to collect the data for this thesis on both $YbFe_2O_{4-\delta}$ and $LuFe_2O_{4-\delta}$ is a Quantum Design MPMS-5S. The temperature range for this model is 1.85 to 400 K with a magnetic field range of up to ±50 kOe.

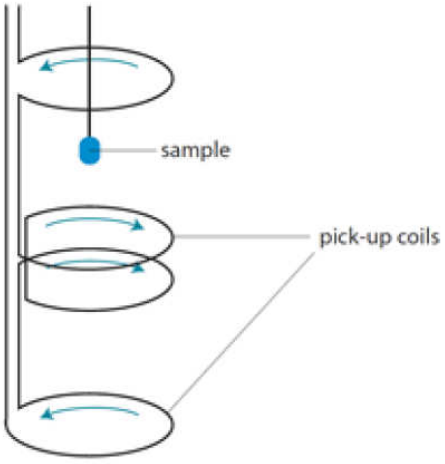

Figure 2.6: MPMS SQUID Pick-Up Coils
Schematic of MPMS pick-up coils and sample within coil boundary. Reproduced from Ref (52).

2.4.2 CCMS (Cryo-Cooled Measurement System) VSM Option

The VSM (Vibrating Sample Magnetometer) works on a very similar basis as the MPMS but in comparison, has a reduced sensitivity. This method of measuring the magnetization is however, much quicker, as the sample is vibrated very quickly between the pick up coils, see figure 2.7. The CCMS also has many other measurement possibilities with various inserts for specific heat, AC susceptibility and thermal conductivity.

2.5 Specific Heat

The specific heat option of the PPMS (Physical Properties Measurement System) is used to view the thermal response of a sample by measuring the heat capacity as a function of temperature. The heat capacity C, of a sample is the heat required to change a samples temperature to a given amount and can be written in the following way:

$$C = \frac{Q}{\Delta T} \tag{2.2}$$

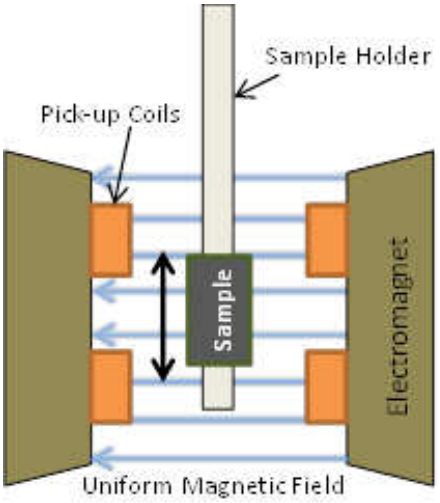

Figure 2.7: VSM
Annotated diagram of VSM, with sample positioned within range of the pick up coils.

where Q is the heat energy and ΔT is the change in temperature. This is the very basic definition of heat capacity. The specific heat capacity of a sample takes into consideration the molar mass which for different compounds vary greatly. This will affect the rate at which the sample can be heated. For the more dense compounds containing Lu and Yb, the specific heat measurement can take days based on the mass of these heavier elements to that of Mg and Ca for example. To measure heat capacity a sample is positioned on a platform in the sample puck insert and fixed with Apiezon-N grease, shown in figure 2.8 (53). To ensure that there is good thermal contact between the sample and the puck platform, the crystal is polished so that it is a thin square or rectangle with usual dimensions of 2x2x1 mm. A heater and thermometer are also attached to the platform which is suspended by contact leads from the middle of the puck. The contact leads connect the heater and thermocouple to the puck while isolating the platform from effects of thermal contact with the PPMS sample chamber. The heat capacity is then recorded by heating the sample to a specific temperature increment and measuring the relaxation time after heating. The platform is heated at a constant rate until the system has reached a percentage increase of the set point (usually 5%). The heating power is then removed and the sample and platform is left to cool back to the set temperature. The grease and the puck will have an added

contribution to the sample heat capacity, therefore an initial empty puck known as an Addenda measurement is performed. This measurement consists only of the empty puck and the Apiezon grease needed for the sample contact.

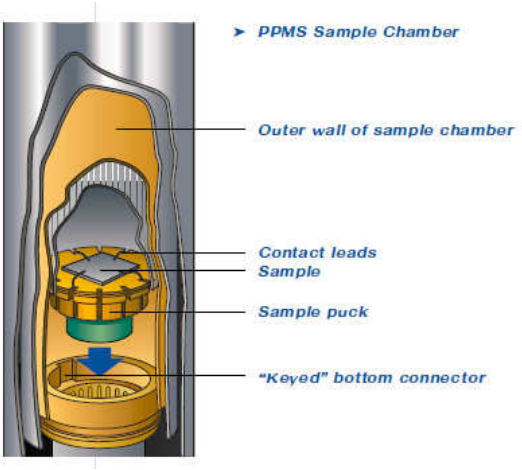

Figure 2.8: Specific Heat Insert
Annotated schematic of PPMS insert with puck and sample. Reproduced from Ref (53).

2.6 a.c Susceptibility

The ACMS (Alternating Current Measurement System) option is another independent insert for the PPMS. With d.c magnetometery, as described in a previous section the moment is measured by the voltage induction of the sample movement through the pick up coils either via vibration of the sample (VSM) or the extraction method (SQUID). In a.c susceptibility measurements, a small alternating current is applied to the dc field which causes a time-dependent moment in the sample. The field of this time dependent moment induces a current in the pick up coils, allowing measurement of the sample without motion. The frequency range which can be applied is between 10 Hz-10 kHz. At very low frequencies H_{AC} (amplitude of the driving field) is very small and the measurement is similar to d.c magnetometery such that the magnetic moment will follow an M(H) relation, shown in the following equation:

$$M_{AC} = \left(\frac{dM}{dH}\right) \cdot H_{AC} sin(\omega t) \tag{2.3}$$

Where M_{AC} is the induced a.c moment, H_{AC}, the amplitude of the driving frequency, ω is the driving frequency and χ=dM/dH is the susceptibility. As the frequency increases the d.c field is altered and the magnetization begins to lag behind the driving field, therefore the a.c susceptibility option can probe two quantities: the magnitude of the susceptibility, χ, and the phase shift denoted by φ (which is relative to the drive signal). These two quantities can also be described as a real in-phase component, χ' and an imaginary out of phase component χ'' which are related in the following way:

$$\chi' = \chi cos\varphi \tag{2.4}$$

$$\chi'' = \chi sin\varphi \tag{2.5}$$

or alternatively rewritten in terms of the d.c susceptibility and phase shift respectively:

$$\chi = \sqrt{\chi'^2 + \chi''^2} \tag{2.6}$$

$$\varphi = \arctan\left(\frac{\chi''}{\chi'}\right) \tag{2.7}$$

The a.c susceptibility option is an essential way of viewing small magnetic shifts correspondent to possible spin glass transitions in a sample below freezing, when applying different driving frequencies. For spin glass behavior, where magnetic spins experience random interactions with other magnetic spins, in a sense freeze into these positions at a certain freezing temperature. The freezing temperature of a sample is determined by the real part of the a.c susceptibility vs temperature, which will show a distinct transition temperature. From here a frequency dependence at that temperature in the imaginary part of the a.c susceptibility is a good indication of spin-glass characteristics; based on the irreversibility in a spin-glass state which leads to a non-zero moment in the imaginary part below the freezing temperature (54).

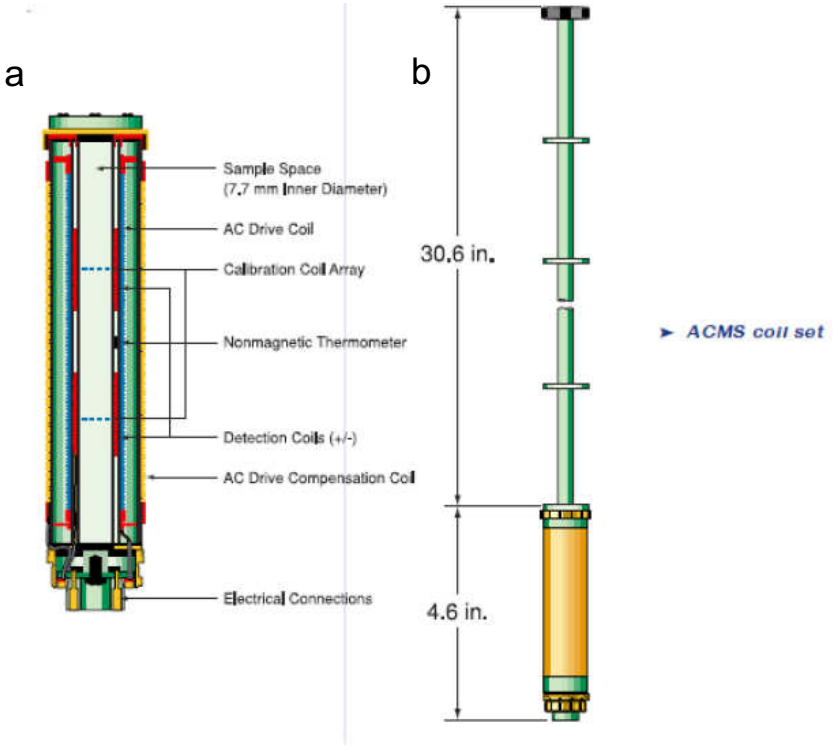

Figure 2.9: ACMS Insert
(a) PPMS Dewar. (b) Main a.c susceptibility insert. Reproduced from Ref (55).

The experimental set-up for the ACMS option requires two probes, the main ACMS insert shown in figure 2.9a and the sample probe which is inserted into the ACMS probe 2.10b (55).

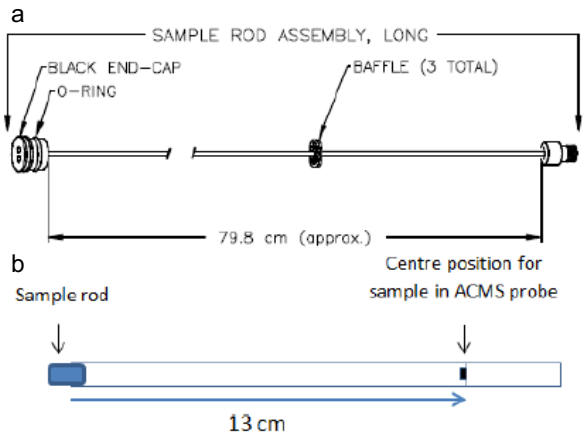

Figure 2.10: ACMS Sample probe and Sample
(a) Schematic of sample probe, (b) Sample holder for probe. (a) reproduced from Ref (55).

2.7 Mössbauer Spectroscopy

The use of Mössbauer spectroscopy provides detailed information about the Fe^{2+} and Fe^{3+} valence states in $YbFe_2O_4$ at various temperatures. Mössbauer spectroscopy works using the principle of the Mössbauer effect: a radioactive source of ^{57}Co nuclei decays slowly into an excited state of ^{57}Fe, where I=5/2. This then decays to either the ground state I=1/2 which happens 9% of the time or to a lower energy state I=3/2 which occurs 91% of the time (24). Once at the lower energy state, it decays further to the ground state, however in the process emits a gamma ray with energy 14.4 keV in a very short time of 0.14μs, shown in figure 2.11 (56). The incident gamma ray can excite a transition in the sample if it is absorbed resonantly. In order for the gamma ray energy to match that of the energy gap in the sample, the ^{57}Co source is moved at a certain speed, v, to allow for a slight adjustment of the frequency based on the Doppler effect. This method was firstly employed with the initial testing of gases and molecules using the Mössbauer effect. An incident gamma ray with energy, $E\gamma$, would hit a freely moving atom or molecule displacing the emission and absorption lines from the nuclear transition energy, however because the atoms are not fixed, there would also be some recoil energy, E_R, which lowers the energy upon emission and to a higher energy upon absorption. This makes the observation of resonant absorption of gamma rays impossible. Therefore by using the Doppler effect and moving the source at some

velocity, v, to the sample allows for a precise tuning of the gamma ray frequency to match the energy gap of the sample in freely moving atoms and crystal structures.

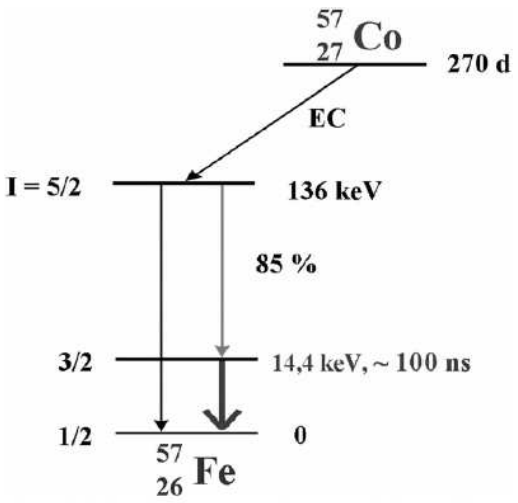

Figure 2.11: Mössbauer Source
Diagram of ^{57}Co decay to ^{57}Fe excited energy state, with further decay to Fe^{3+} lower energy state and Fe^{2+} ground state energy. Reproduced from Ref (56).

The set-up for Mössbauer spectroscopy can be seen in figure 2.12 (56), where the ^{57}Co source is positioned on a vibrator and vibrated at a velocity, v, typically for ^{57}Fe, the velocity v=0.096 mm.s-1 the linewidth Γ_o=4.7x10^{-9} eV and the transition energy E_γ=14400 eV. The incident gamma ray hits the Mössbauer absorber (the sample to be analyzed) and the information is read by the detector, where the source and absorber are moved relatively to each other with the Doppler velocity. The cryostat allows for low temperature measurements of the sample usually with a range of 300 K to 4 K. The gamma rays are collected in a scintillation counter, where pulses from the detector are then amplified before passing through a discriminator. The function of the discriminator enables the filtration of non-resonant background radiation from the input signal from the sample, therefore cleaning the output signal. The signal is then fed to the computer. The function of the multichannel analyzer, constant frequency clock, waveform generator and servo amplifier all work towards controlling the frequency of the vibrator to optimize the the resolution of the Mössbauer spectrum.

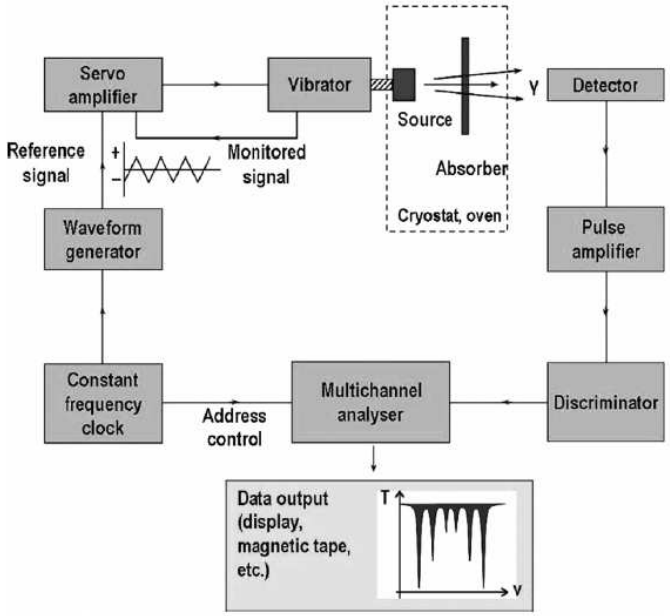

Figure 2.12: Mössbauer Spectroscopy Set-Up
Annotated schematic of Mössbauer spectroscopy equipment. Reproduced from Ref (56).

2.8 Neutron Scattering

Neutron diffuse scattering was performed at FRM II: DNS (Diffuse Neutron Scattering). DNS is a diffuse scattering cold neutron time-of-flight spectrometer with polarization analysis at the neutron guide NL6a (57). This type of polarized neutron scattering allows for a separation of the nuclear coherent, spin incoherent and magnetic scattering contributions over a large range of scattering vector $\boldsymbol{Q}$ and energy transfer E. The schematic in figure 2.13 shows a detailed view of the experimental set-up with neutron guide and monochromator for the selection of one particular wavelength of the neutron beam with a range of λ=2.4-6 Å. Depending on the sample size, the wavelength can be altered to focus the beam. The beam is then sent through the beam tube and chopper 1, once the neutron beam reaches this stage it passes through a polarizer which flips all the neutrons to one specific polarization. The polarized neutrons then pass through a second chopper which records the polarization of the neutrons after they have passed though the polarizer. This is important as it allows for a detailed calculation of the neutrons which are scattered by the sample at a range of angles in Q and collected

by the xyz coils. If the neutron polarization is known before they are incident on the sample it is then possible to determine any magnetic structure as these will be flipped on scattering from the sample.

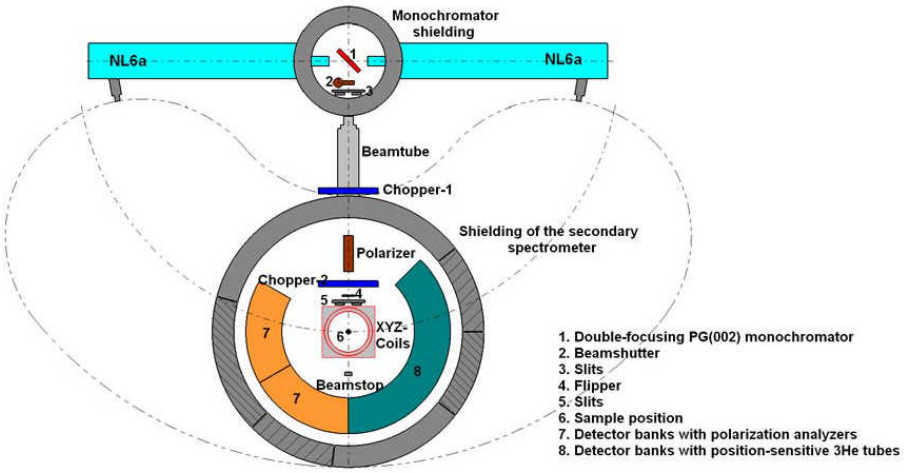

Figure 2.13: Diffuse Neutron Scattering Set-Up
Annotated schematic of DNS layout. Reproduced from Ref (57).

3

Investigations into $LuFe_2O_4$

3.1 Charge Ordered $LuFe_2O_4$

The mechanisms which form the basis of the charge ordering were described in detail in the introduction. The following section will provided a brief but well informed overview of the experimental results which lead to the conclusion that $LuFe_2O_4$ was in fact the first material which provided evidence of ferroelectricity through charge ordering.

$LuFe_2O_4$ has a rhombohedral structure with hexagonal lattice parameters: a=b=3.44 Å, c=25.28 Å, α=β=90 °C and γ=120 °C. In 1988-1989 the first single crystals of $LuFe_2O_{4-\delta}$ were grown via floating zone method in varying oxygen partial pressures (58) (59). Shortly after this, magnetization measurements were performed by Iida *et al.* of M(H) at 4.2 K with an applied field of 230 kOe, and highlighted the presence of a 2:1 ferromagnetic structure in a triangular lattice (47). In order to gain a better in sight into the magnetic structure, neutron scattering at 14 K of a single crystal orientated along the *c* axis, provided the first evidence of magnetic peaks along the (1/3, 1/3, l) line (47), which were later confirmed with measurements performed by Ikeda *et al.* (60) (see figure 3.1).

Further work by Ikeda *et al.*, gave the first detailed magnetic phase diagram for off-stoichiometric $LuFe_2O_{4-\delta}$ within the temperature range 150-500 K, shown in figure 3.2. Above 500 K all the Fe sites appear to have a charge of $2.5e^-$, caused by the thermal movement of valance electrons (61). With decreasing temperature the system transforms into a two-dimensional charge density wave state (2D-CDW) from complete

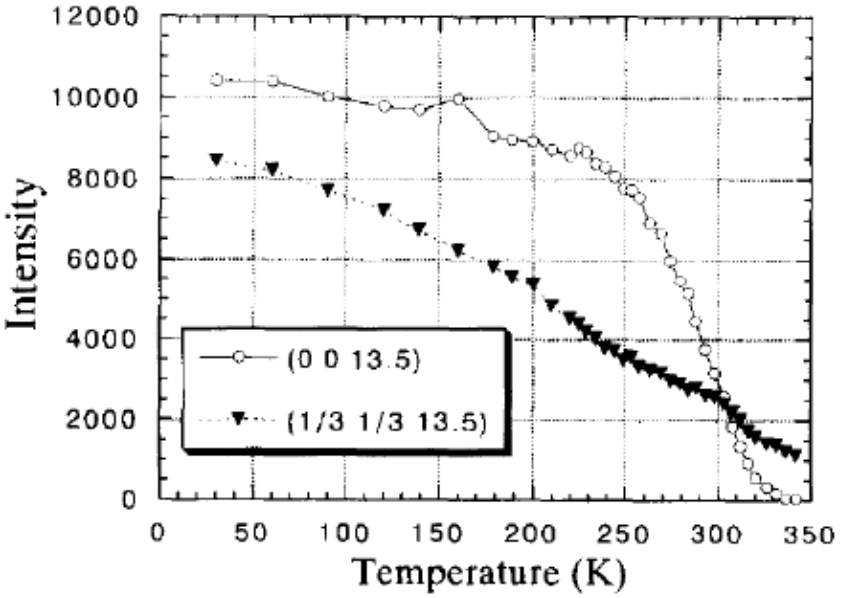

Figure 3.1: Early Neutron Scattering on $LuFe_2O_4$
Temperature variation of the scattered intensity of the two superlattice spots (1/3, 1/3, 3.5) and (0, 0, 13.5). Reproduced from Ref (60).

disorder above 500 K. The 2D-CDW was seen clearly in electron diffraction measurements, where diffuse Bragg lines along the (1/3, 1/3, l) line appeared before the onset of 3D charge order spots below 330 K (62).

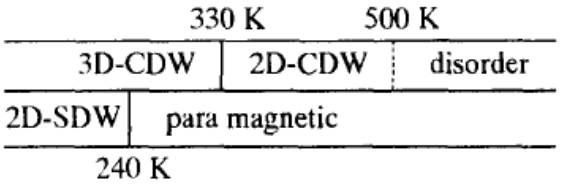

Figure 3.2: Magnetic Phase Diagram
Magnetic and CO phase diagram showing transitions at 500, 330 and 240 K. Reproduced from Ref (60).

Magnetic ordering within this system was not clearly clarified by Ikeda *et al.*; they stated that the system goes from a paramagnetic to a 2D-CDW, but at that time was not well defined experimentally (60). It was Christianson *et al.*, who much later, with neutron diffraction measurements, clarified the lower temperature magnetic phase to be 3D ferrimagnetic order. Therefore the system goes through two first-order magnetic phase transitions; paramagnetic to ferrimagnetic ordering at 230 K followed by a second magnetostructural transition at 175 K (62). The variation between 2D and 3D magnetic order stems from the quality of the single crystals being measured due to off-stoichiometry. The most ground breaking advancements into the understanding of $LuFe_2O_4$ were presented by Ikeda *et al.* in 2005 (2). From their initial neutron diffraction experiments (60) and the classification of charge and magnetic order along the (1/3, 1/3, l) line, lead to the first viable charge order model. As described in section (1.4) the charge frustration on each Fe monolayer drives a polar arrangement across each Fe bilayer, with one layer rich in Fe^{2+} and the second layer rich in Fe^{3+} inducing a cross polarization (2). The competing interaction between frustrated charges are settled by a $\sqrt{3}$ x $\sqrt{3}$ supercell, shown in figure 3.3, where the charge superstructure is enlarged by three times in the *a*-*b* plane along the (1 1 0) direction.

To further support their CO model, resonant x-ray scattering (RXS) was performed

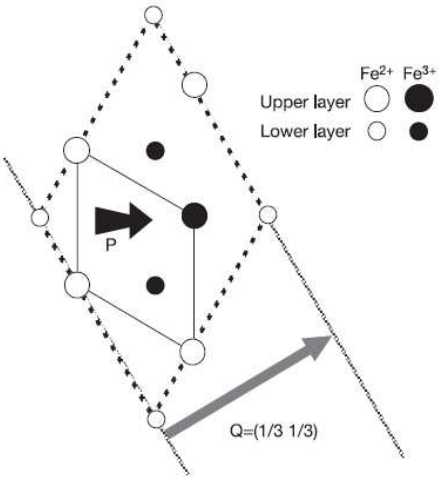

Figure 3.3: CO Superstructure
Chemical unit cell and $\sqrt{3}$ x $\sqrt{3}$ superlattice marked by solid and dotted lines, respectively. The arrows indicate the direction of polarization **P** and wave vector Q=(1/3, 1/3) representative of the charge wave. Reproduced from Ref (2).

on a $LuFe_2O_4$ single crystal oriented along the c axis. The data shown in figure 3.4 shows the x-ray energy dependence of the super lattice reflection along (1/3, 1/3, 5.5). The maximum peak at 7.113 keV and the minimum peak at 7.120 keV represent the in-phase component of the anomalous atomic scattering factors of Fe^{2+} and Fe^{3+}. This result clearly indicates that the structure factor of the super lattice point (1/3, 1/3, 5.5) is contributed by the positive atomic scattering factor of Fe^{3+} and the negative scattering factor of Fe^{2+}.This result therefore highlights that the structure factor at this Bragg point arises from the difference of atomic scattering factors Fe^{2+} and Fe^{3+}.

The final major turning point for the, at that time valid CO theory, came from the experimental proof of switchable polarization within this system. In order to test whether the system had a switchable polarity, the sample was cooled down to 77 K under an electric field of ± 10 kV cm^{-1} and orientated along the c axis, where the current flow from the sample was then measured upon heating without an electric field. The results of this experiment showed that the direction of current flow depends on the sign of the cooling electric field below 350 K, near the onset of 3D CO. The spontaneous polarization was estimated by calculating the integral of the current from the

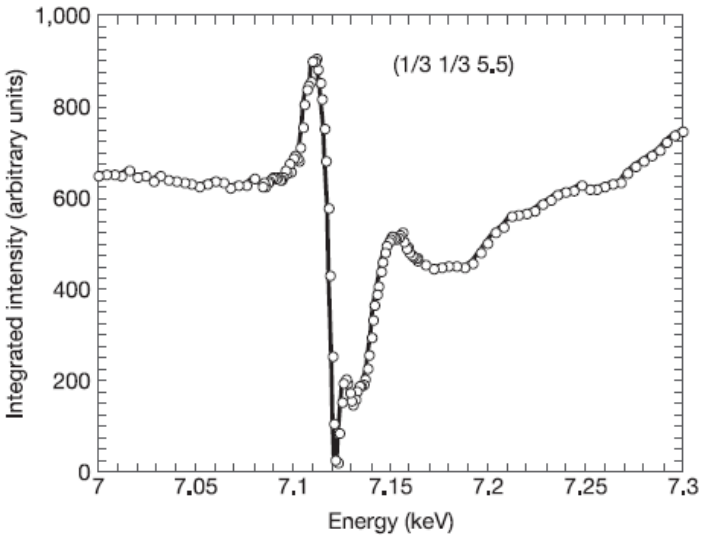

Figure 3.4: X-ray Energy Dependence of $LuFe_2O_4$ Superlattice
Integrated intensity as a function of energy along the (1/3, 1/3, 5.5) line, peak and minimum arise from the in-phase component of the anomalous scattering factor for Fe^{2+} and Fe^{3+}, respectively. Reproduced from Ref (2).

sample and is shown in figure 3.5, as a function of temperature. The large decrease in spontaneous polarization occurs when increasing the temperature to 250 K; the onset of the ferrimagnetic transition temperature. A further decrease in the spontaneous polarization is seen when the temperature reaches 330 K at which the CO superstructure of Fe^{2+} and Fe^{3+} appears. The broad shoulder of the electric polarization around 250 K indicates the coupling of magnetization with electric polarization, and shows that $LuFe_2O_4$ is a polar substance that can be switched by an external electric field, where the ferroelectricity is developed by a polar arrangement of Fe^{2+} and Fe^{3+} (2).

For many years $LuFe_2O_4$ was believed to be one of the first experimentally proven CO ferroelectric compounds in the rare earth series. Investigations by several groups uncovered that $LuFe_2O_4$, as well as other RFe_2O_4 compounds, were extremely sensitive to oxygen stoichiometry, which greatly effected the magnetic and charge order within each crystal growth. From a wide range of magnetization, neutron scattering and electron spectroscopy measurements it was discovered that single crystals grown in an oxygen reducing atmosphere exhibited 3D magnetic and CO order than being grown in a more oxidizing atmosphere ($CO:CO_2$=1:6) (42). Crystals grown in a non-oxygen

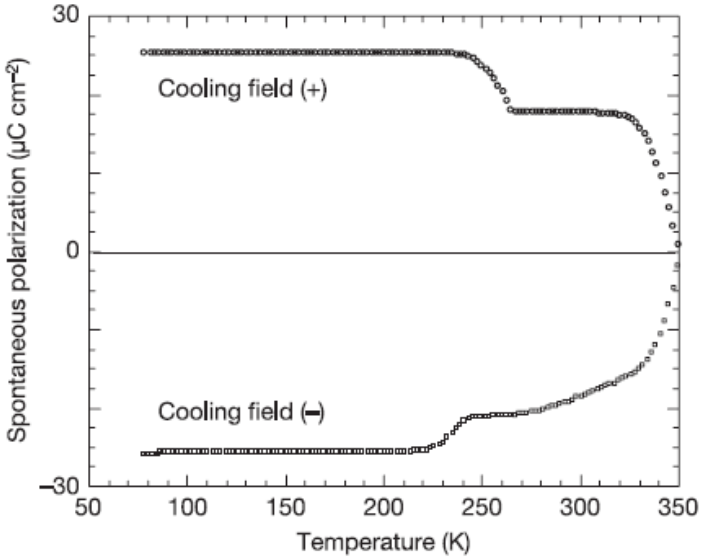

Figure 3.5: Spontaneous Electric Polarization
Temperature variation of the electric polarization of $LuFe_2O_4$. The current flow from the sample was recorded on heating after electric field cooling along the c axis. Image taken from reference (2).

reducing atmosphere were prone to 2D magnetic order and glassy behavior, with only diffuse charge order along the (1/3, 1/3, l) line (2)(58)(60)(62).

3.2 $LuFe_2O_4$ in a New Light

A few years after the definitive results by Ikeda *et al.*, clarifying that $LuFe_2O_4$ is in fact a CO ferroelectric material, investigations by Angst *et al.*, into $LuFe_2O_{4-\delta}$ lead to the ultimate conclusion that the system in not a CO ferroelectric, based upon a non-polar arrangement of ions, as a result of the iron valance ordering on each bilayer and alternative magnetic ordering. Through careful monitoring of the oxygen stoichiometry and fine tuning the oxygen partial pressure, they established three different kinds of crystal quality classifications with the use of temperature dependent magnetization. By performing extensive neutron diffraction and X-ray Magnetic Circular Dichroism (XMCD) measurements they uncovered the behavior of the magnetostructural transition at 175 K. Single crystal x-ray diffraction provided a solid understanding of the magnetostructural transition and highlighted a structural change from a rhombohedral to monoclinic unit cell below 210 K. The following section will provide a detailed insight into the current understanding into both the magnetism and CO within $LuFe_2O_{4-\delta}$.

3.2.1 Magnetic Behavior

Angst *et al.* performed a number of experiments on crystals with varying CO:CO_2, to investigate the changes in the magnetic characteristics as a result of oxygen stoichiometry. The initial test, as mentioned in section (1.2), is to perform ZFC, FW and FC magnetization measurements as a function of temperature with an externally applied field of 100 Oe and with crystals orientated such that H$\|c$. This process is necessary to establish a qualitative picture of the magnetic transitions, their temperature range and sharpness, which are all evidently affected by off-stoichiometry. The magnetization data shown in figure 3.6 was measured with three different crystals from one single crystal growth, as mentioned in section (1.2.1), there is notable sample to sample dependence in one crystal growth and this is seen clearly in the three types of magnetization curves (32).

The Type A magnetization curve represents a crystal of good stoichiometric quality, where the magnetization data exhibits a large, sharp transition at 238 K. The magnetization on cooling from room temperature is zero but during the onset of magnetic order around 250 K, the curve increases slightly above 0.000 μ_B/f.u. At the transition temperature a steep increase in the magnetization occurs and reaches a maximum of 0.0252 μ_B/f.u. The slope of this transition peak again decreases rapidly to a low magnetization of 0.005 μ_B/f.u before the onset of the second magnetostructural transition at 175 K, previously reported in (63). On cooling through this temperature almost no transition is visible, however, on warming a large broad transition with a maximum magnetic moment at 0.0152 μ_B/f.u occurs. This particular transition was first recognized and reported by Iida *et al.* (41) where it was called the 'anomalous field-heating-effect' and is described in more detail later. Type B magnetization curves present crystals of average quality and exhibits transitions as Type A, but at slightly shifted temperatures. The main Néel transition is shifted to a lower temperature of 230 K and does not exhibit the same sharpness and definition as the Type A curve. The magnetization of the magnetostructural transition in the Type B magnetization is slightly lower, with much less peak definition. The final type of magnetization curve C, represents a crystal of poor stoichiometric quality. On FC and FW, the ferrimagnetic transition is represented by a very broad transition at approximately 220 K with a magnetization of ~1 μ_B/f.u, which exceeds that of the previous two types A and B. There is a large shift in the magnetostructural transition temperature to 155 K and almost no difference between the FC and FW data. The third curve plotted on this magnetization curve is ZFC, which is acquired by cooling the magnetometer from room temperature in zero field and applying the desired magnetic field at base temperature, measuring the magnetization on warming. The main transition at ~240 K exhibits a considerably lower magnetization, indicating that there are ferro- or ferrimagnetic components stabilized in this sample type by cooling under moderate magnetic fields. The magnetostructural transition in the Type C magnetization is seen as only as a small broad hump at ~160 K.

A.c susceptibility measurements (refer to section 2) shown in figure 3.7 performed on both Type A and Type C samples, show quite contrasting behavior but corroborate well with their individual magnetization data. The Type A crystal, with very

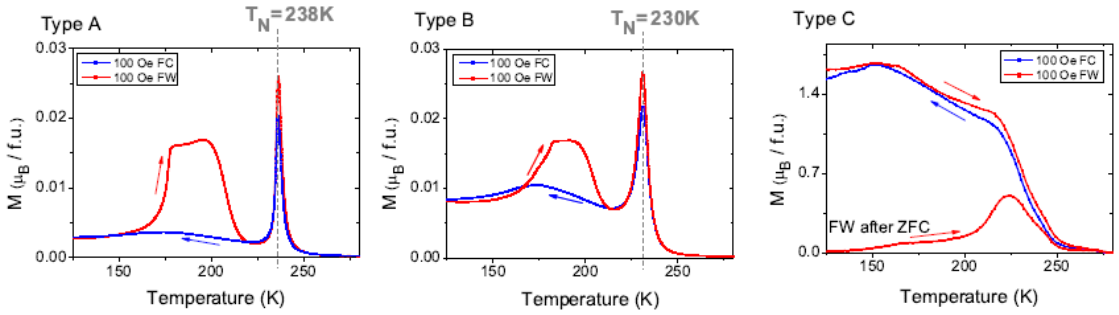

Figure 3.6: Crystal Quality Classification
Magnetization measurements as a function of temperature on cooling and heating, with magnetic field H=100 Oe applied parallel to c_{Hex}. Type A-C were taken from three varying $LuFe_2O_4$ single crystal qualities from the same batch. Reproduced from Ref (32).

sharp magnetic transitions present in the magnetization data, exhibits no frequency dependency in the a.c susceptibility. The type C crystal on the other hand presents a definitive frequency dependence at main Néel transition, which is a prime indication for spin glass behavior, where competing magnetic states exist (64).

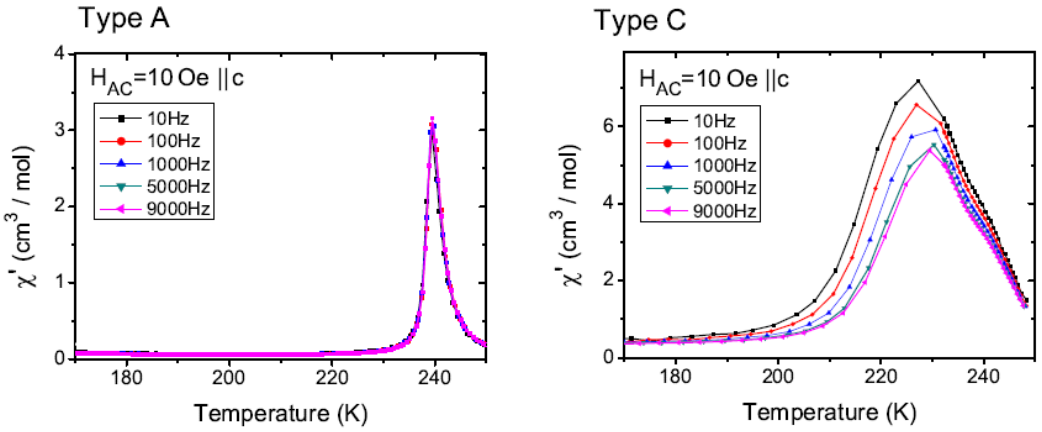

Figure 3.7: A.c Susceptibility of Type A and Type C $LuFe_2O_4$ Single Crystal
A.c susceptibility measurements with different driving frequencies on cooling, with increments of 0.1 K/min. The amplitude of the oscillating magnetic field was 10 Oe for all presented frequencies. Reproduced from Ref (32).

As mentioned previously, the magnetic ordering below room temperature goes through two magnetic phases at 238 K the Néel transition and 175 K the magneto-structural transition. The magnetic behavior at 175 K was first encountered by Iida *et al.*, 1976. Recent neutron scattering data by the Angst *et al.*, group (65) have uncovered the existence of two competing antiferromagnetism and ferrimagnetic phases. The data shown in figure 3.8 was measured on a crystal of comparable quality to that of Type A. Neutron diffraction was performed at 220 K (below the Néel temperature) along the (1/3, 1/3, l) line in H=2.5 T and H=0 T, shown in figure 3.8a. The data shown in figure 3.8b-c, show the integrated intensity scans along the (1/3, 1/3, l) in the anti and ferrimagnetic phase. The data clearly provides strong evidence of the existence of two magnetic phases, contradictory to the initial neutron diffraction measurements by Ikeda *et al.* (60) which presented data for only the ferrimagnetic phase.

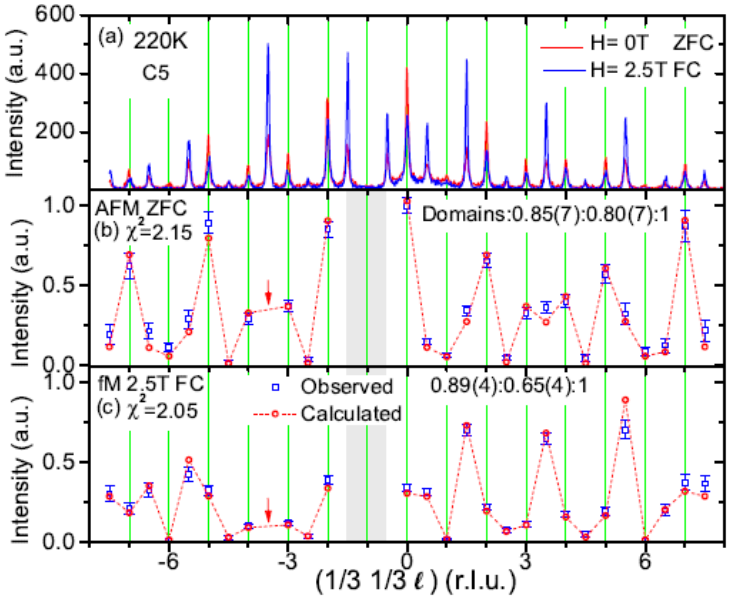

Figure 3.8: Neutron Scattering on Type A $LuFe_2O_4$ Single Crystal
(a) Neutron diffraction pattern along (1/3, 1/3, l) line in both H=2.5 T and H=0 T. (b and c) show the integrated intensity for scans along the (1/3, 1/3, l) in both the AFM and fM phase respectively. Reproduced from (65).

From the recent neutron scattering and magnetization data obtained by Angst *et*

al. (65), the first clear magnetic phase diagram was constructed, and is shown in figure 3.9. In this phase diagram the magnetic field H is a function of temperature, with the crystallographic *c* axis orientated parallel to the H field. The paramagnetic phase which sets in at 500 K remains until 240 K, before the onset of both ferrimagnetic (fM) and antiferromagnetic (AFM) ordering below 240 K. The hysteretic region below 225 K (marked with stripes) shows the region where either ferri or antiferromagnetic ordering can be stabilized. The anomalous field heating effect at T_{LT}=175 K shows a distinct jump in the magnetization on FW compared with the low magnetization of the corresponding FC data, which is shown clearly in the magnetization data (see figure 3.6).

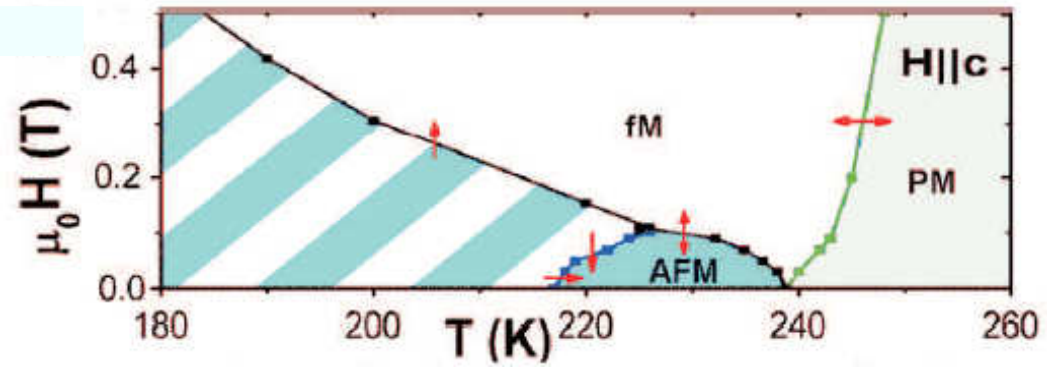

Figure 3.9: New Magnetic Phase Diagram for $LuFe_2O_4$
Magnetic field H - temperature T phase diagram between 260 K and 180 K, which exhibits paramagnetic, antiferromagnetic and ferrimagnetic ordering. The data was extracted from various M(H) and M(T) curves. Reproduced from Ref (65).

In order to understand this field heating effect we must first understand the magnetic ordering below 175 K. On warming above T_{LT}=175 K, the sample, according to the phase diagram shown in figure 3.9, enters a region in which both AFM and fM phases can be simultaneously stable in low-H (100 Oe). The mesoscopic AFM and fM regions within the sample have no driving force to fully settle into a single magnetic state, until one phase becomes unstable. Below T_{LT}=175 K, applying even a small magnetic field promotes the increase of the fM fraction, where the eventual disappearance of the structural distortion provides a sudden increase in the magnetization, shown clearly in

the magnetization data (see figure 3.6). The spin structure below 240 K with existence of both AFM and fM phases, stems from ordering between the bilayers within the unit cell. For the AFM order, one bilayer has majority spins pointing up and the lower bilayer contains majority spins pointing down. Due to the mixed valance state of this system, the fM phase has a majority of spins with in each bilayer pointing upwards, but based on the concentration of Fe^{2+} and Fe^{3+} a ferrimagnetic state is induced.

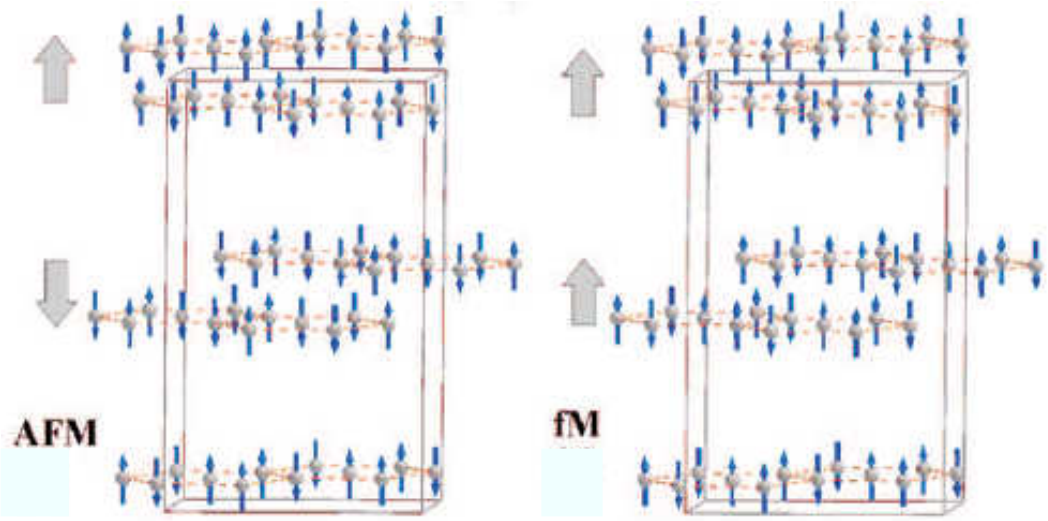

Figure 3.10: Spin Sructure of New Monoclinic Unit Cell
Spin structure of *C2/m* unit cell showing (a) AFM phase and (b) fM phase. Reproduced from Ref (65).

3.2.2 Charge Order

The charge order based ferroelectricity in $LuFe_2O_4$ due to Fe valance order through geometric frustration on the triangular Fe-O bilayers, had for some time, provided a definitive theory. However, the investigation into the Fe/O bilayer becoming polar upon CO was never fully challenged. Detailed measurements of single crystal x-ray diffraction with bond valance sum analysis (BVS) as well as XMCD measurements (66) performed by the Angst et al., group have uncovered a new CO pattern with the existence of charged Fe/O bilayers. Symmetry analysis of a hexagonal unit cell with a (1/3, 1/3, 3/2) propagation below 240 K, produced two irreducible representations of the inversion symmetry within the unit cell that are allowed and both of which lower the space group symmetry to *C2/m* (Monoclinic). The first central position is located at the Lu site between the Fe bilayers, this arrangement corresponds to the antiferroelectrically (AFE) stacked polar bilayers, initially proposed in (67). The second possible representation for positioning the inversion centre is located between the two Fe-layers of a bilayer, corresponding to a non-polar bilayer with net charge. In order to test each theory, single crystal x-ray diffraction was performed on a good stoichiometric crystal at 210 K and refined in the hexagonal and monoclinic unit cell, shown in figure 3.11 (66).

Single crystal x-ray refinement of the structure model with centre of inversion located in the Lu layers, corresponding to the antferroelectrically stacked bilayers, lead to a very anisotropic displacement parameter for Lu along the c_{hex} direction, which is unlikely, due to the heavy mass of the Lu ions. A poor refinement factor of $R[F^2 > 4\sigma(F^2)] \sim 5\%$ was achieved indicating that the presence of a Lu centered inversion symmetry leading to an antiferroelectric state would not provide a credible CO arrangement. For refinements of inversion symmetry located between the Fe layers, a much better refinement factor of $R[F^2 > 4\sigma(F^2)] \sim 5.96\%$ was achieved. This as well as in depth BVS and XMCD data (66) provided a solid basis for a new charge order theory for $LuFe_2O_4$. The new evidence for the centre position of inversion symmetry lead to a final structure determination below the Nèel magnetic ordering temperature, changing the initial hexagonal unit cell to a lower symmetry monoclinic unit cell. Moreover, the new structural refinements show that the Fe/O bilayers are charged rather than polar and not affected by electric fields, no longer making $LuFe_2O_4$ a CO ferroelectric. A

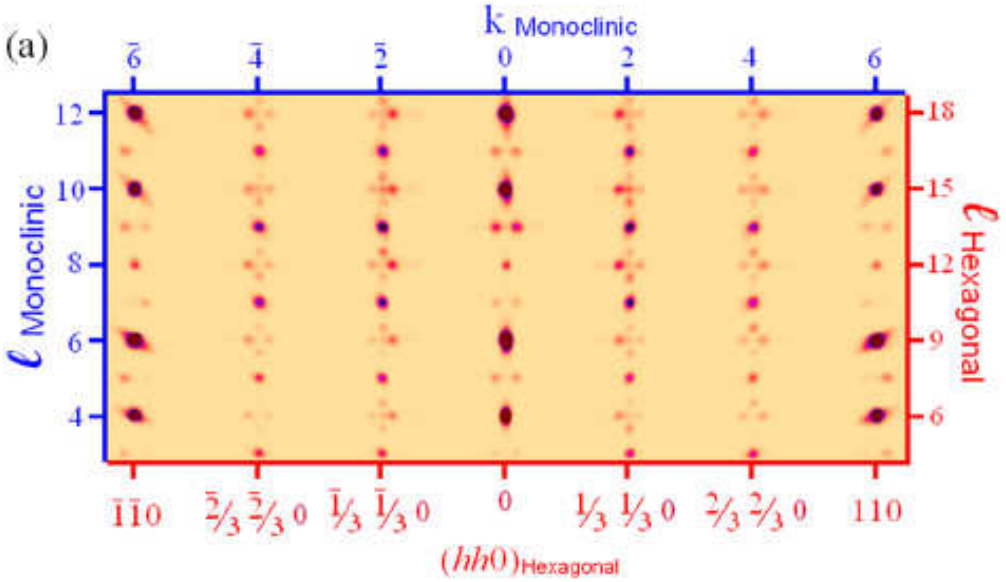

Figure 3.11: Single Crystal X-ray Diffraction of $LuFe_2O_4$
Single Crystal diffraction image in the (0KL)-plane indexed with both monoclinic and hexagonal cell along the (1/3, 1/3, l) line. Reproduced from Ref (66).

detailed diagram of the new monoclinic unit cell with a non-polar bilayer arrangement is shown in figure 3.12, with each bilayer containing either an Fe^{2+} rich valency or a Fe^{2+} rich valance state.

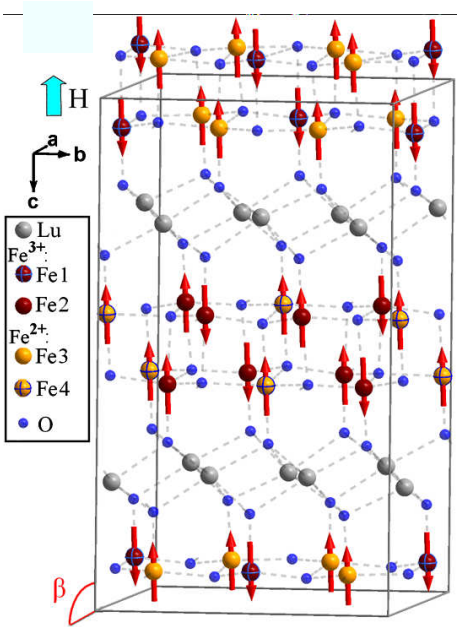

Figure 3.12: Monoclinic Unit Cell with New Spin Structure
Monoclinic structure *C2/m* of $LuFe_2O_4$ measured at 210 K with refined lattice parameters a=5.95 Å, b=10.30 Å, c=16.96 Å, β=96.72°. The ferrimagnetic high-field spin order and $Fe^{3+/2+}$ charge order is represented by arrows and different colours respectively. Reproduced from Ref (66).

The following results presented in this chapter will highlight some of the findings from the magnetization measurements with an applied field of 100 Oe, as well as new measurements on the specific heat and single crystal x-ray diffraction of $LuFe_2O_4$ single crystals, grown in both $CO:CO_2$=1:3 (1:3) and $CO:CO_2$=1:5 (1:5) gas atmospheres.

3.3 Results

3.3.1 Magnetization

The SQUID magnetometer described in section (2.4.1), was used to measure the magnetization of the samples with a temperature range of 10-300 K and an externally applied magnetic field of 100 Oe. The magnetization as a function of temperature was mea-

sured for both ZFC (10-300 K) and FC (300-10 K) data with a sweep rate of 2 K/min. The magnetization on both heating and cooling was measured with three crystals, two crystals grown in the (1:5) and one crystal in the (1:3) gas ratio, with the magnetic field applied parallel to the the c axis only, based on the previous finding described in chapter 1. The two crystals taken from the (1:5) growth weigh 2.33 g and 36.66 mg labeled (1:5A) and (1:5B), respectively. The measurement of the smaller crystal is necessary to provide a direct comparison to the specific heat, where the larger crystal is too large for the PPMS sample platform. Not only this, but a comparison between two single crystals of different mass will show any contrasts between the magnitude of the magnetization at each temperature transition.

The magnetization data shown in figure 3.13, contains ZFC and FC curves for $LuFe_2O_{4-\delta}$ grown in the (1:3) (a) and (1:5A) (b) gas ratios. The (1:3) crystal exhibits only one main transition at T=202 K, with ZFC and FC curves at that point reaching the same magnetization of 0.015 μ_B/f.u, where the curve below the Néel temperature is smooth with no lower temperature features. The (1:5A) crystal has a much higher Néel transition of 235 K, but the magnetization of the ZFC reaches a maximum of ∼0.048 μ_B/f.u whereas the FC data has a lower magnetization of ∼0.036 μ_B/f.u. Also present on the (1:5A) data but absent on the (1:3) data is a second, lower temperature transition at T_{LT}=175 K with a magnetization ∼0.023 μ_B/f.u on both heating and cooling. There is a noticeable hysteresis present at this transition with the ZFC maximum reaching T_{LT}=182 K and the FC maximum reaching T_{LT}=170 K. Below the low temperature transitions there is a small broad feature in the ZFC data at T∼100K and a general increase in magnetization in the FC to base temperature at 10 K.

A magnetization measurement on ZFC and FC on the second smaller (1:5B) single crystal is shown in figure 3.14. In comparison to the larger (1:5A) crystal, there is almost no temperature shift in the main Néel temperature at T_N=234 K, however the peak sharpness on ZFC and FC is slightly reduced. Interestingly, the overall magnetization at T_N is higher in the smaller crystal, which reaches ∼0.078 μ_B/f.u on ZFC compared to that of the larger crystal which reaches a maximum of ∼0.048 μ_B/f.u. The transition at T_{LT} is similar to that of the larger crystal with respect to the shape and temperature range, where only a small shift in temperature from 182 to 180 K on ZFC and 170 to 167 K on FC. However, a large difference is seen in the magnitude of the magnetization at

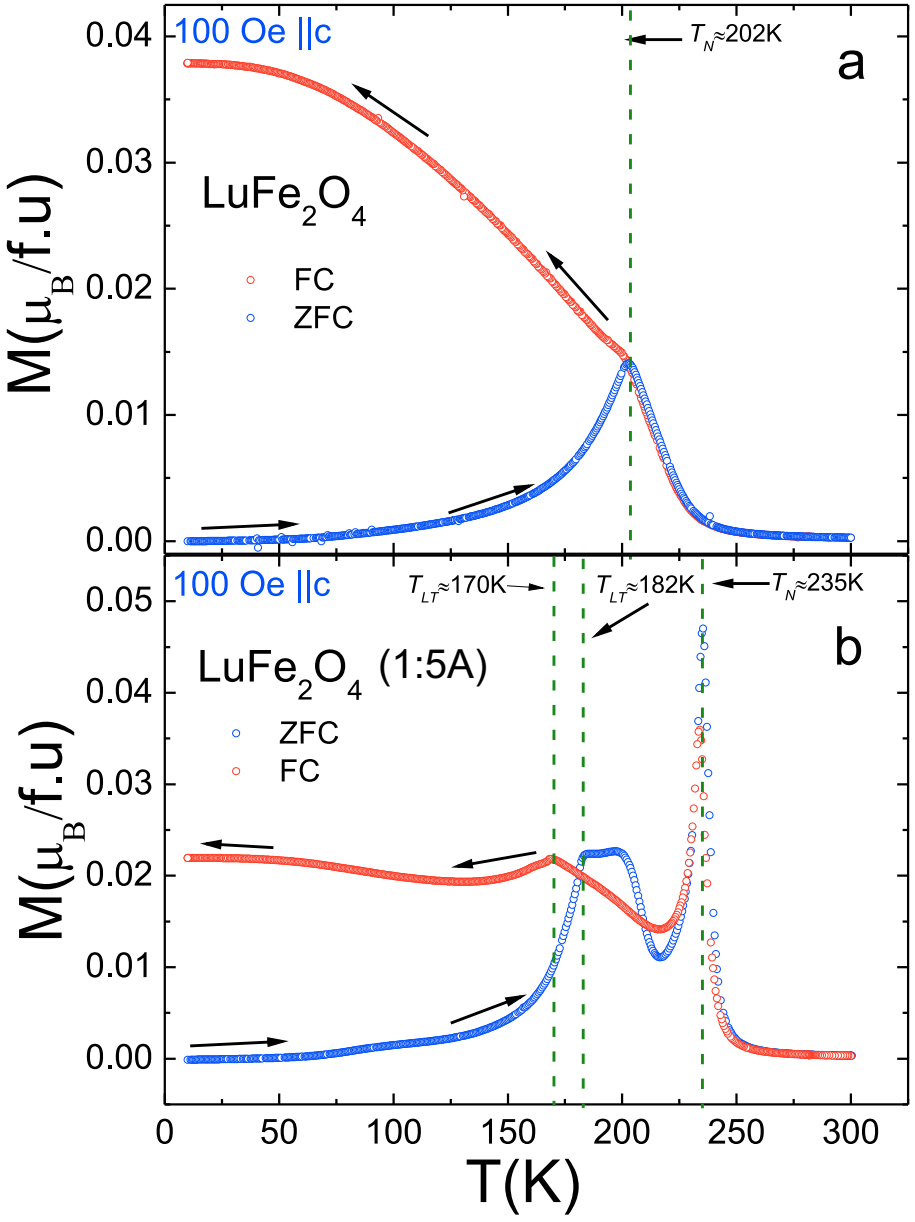

Figure 3.13: Magnetization
(a) ZFC and FC magnetization data of single crystal grown in CO:CO_2=1:3. (b) ZFC and FC magnetization data of single crystal grown in CO:CO_2=1:5 (1:5A).

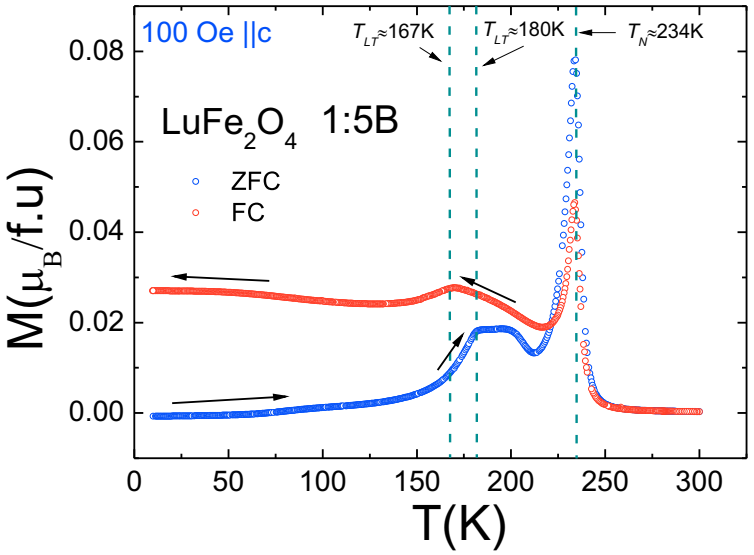

Figure 3.14: Magnetization
(a) ZFC and FC magnetization data of single crystal grown in CO:CO_2=1:3. (b) ZFC and FC magnetization data of single crystal grown in CO:CO_2=1:5 (1:5B).

T_{LT} on ZFC. The ZFC and FC curves no longer reach the same magnetization at T_{LT}, which was seen clearly in the magnetization data of the larger crystal. A notable change is also seen in the height of the magnetostructural transition in terms of magnetization range on ZFC (covers a range $\sim$1 μ_B/f.u), which is almost half compared to that of the range exhibited by the larger crystal.

3.3.2 Specific Heat

The specific heat measurements were performed in two stages, an initial empty puck measurement which is described in detail in section 2.5 followed by the sample measurement. For both experiments the puck was mounted and cooled to either base temperature of 1.85 K or the temperature desired (based on the temperature regime of interest) and the specific heat was measured on warming. The two data sets for the empty puck and sample measurement were analyzed by subtracting the puck data from the sample data, to gain only the sample heat capacity. The heat capacity was then converted to specific heat by dividing the heat capacity by the molar mass of the sample and plotted as a function of temperature.

The specific heat as a function of temperature for the 1:3 and 1:5B crystal is shown in figure 3.15. The data from the 1:3 crystal (see 3.15a) shows two smeared out transitions at T_N=230 K and a higher temperature, broad feature at T_{CO}=314 K, representative of CO. Despite a very slight shift in the Néel temperature, the 1:5B crystal (see 3.15b) shows both transitions but much sharper and defined. Both the 1:3 an 1:5B specific heat curves show no lower temperature transitions below the main Néel transition at 230 K.

3.3.3 Changes in Stoichiometry

During the specific heat measurement of the 1:5B $LuFe_2O_{4-\delta}$ single crystal the temperature of the crystal was taken to 400 K. According to previous publications on $LuFe_2O_{4-\delta}$, the oxygen stoichiometry is very volatile, where heating beyond 350 K can alter the magnetic and CO properties, either by changing the oxygen composition or content within the sample. The same experimental conditions used for the previous magnetization and specific heat data acquisition were also applied to this set of measurements.

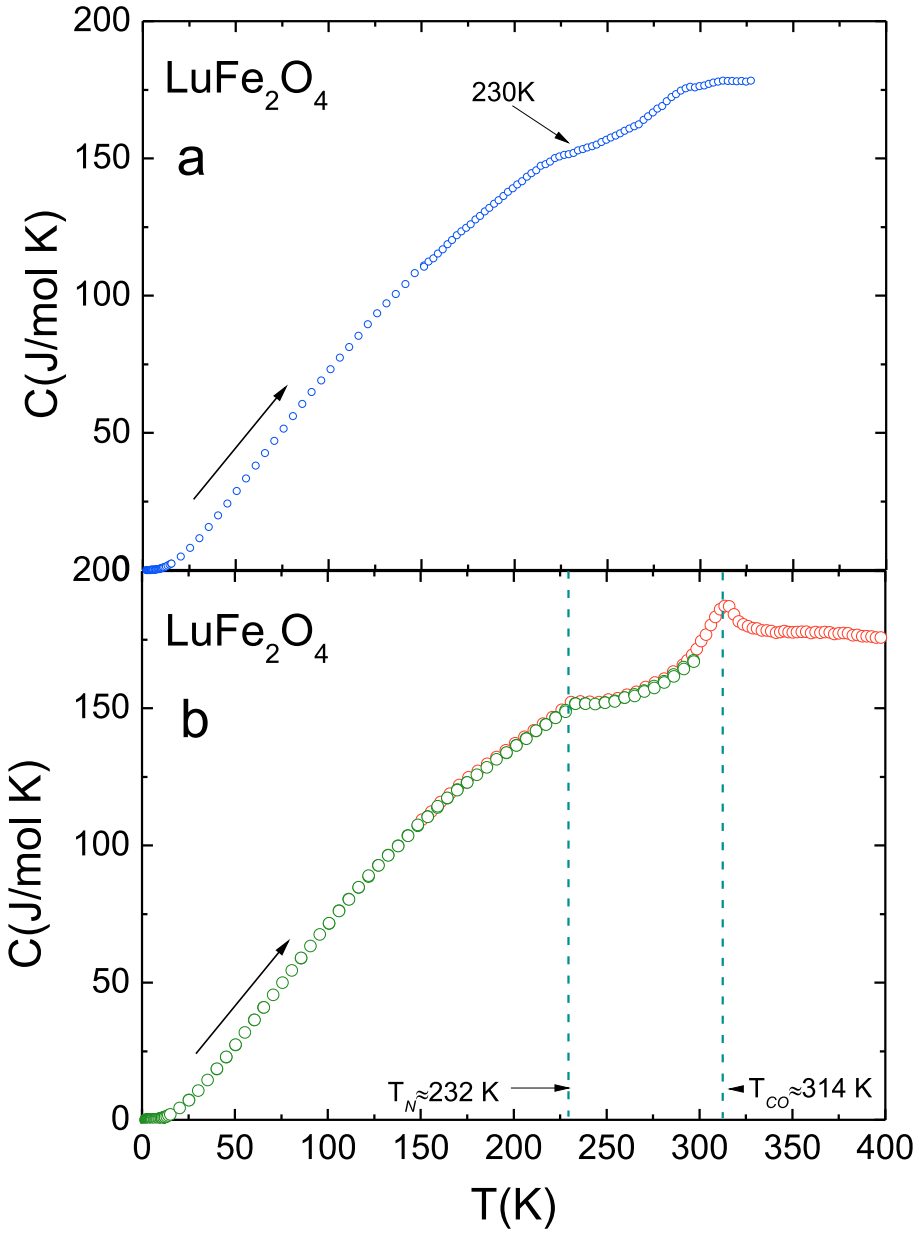

Figure 3.15: Specific Heat

(a) Specific heat curve of crystal grown in CO:CO_2=1:3. (b) Specific heat curve of crystal grown in CO:CO_2=1:5 (1:5B). Green curve has temperature range of 1.85-300 K, red curve has temperature range 150-400 K (black arrows indicate direction of warming).

3.3.3.1 Magnetization

The ZFC and FC magnetization data for the 1:5B single crystal after heating to 400 K is shown in figure 3.16. There is a large difference in the magnitude of the magnetization on both the FC and ZFC data, compared to the original magnetization measurement. The ZFC data reaches a higher maximum magnetization of ~0.086 μ_B/f.u at a slightly lower Néel temperature, T_N=232 K. The T_{LT}=175 K transition present in the ZFC data is very smeared out, with a lower magnetization of 0.01 μ_B/f.u, compared with the initial measurement before heating, which exhibits a maximum magnetization of ~0.018 μ_B/f.u. There is a large alteration to the FC data after heating the crystal to 400 K. On cooling, the FC curve reaches a maximum magnetization of 0.068 μ_B/f.u. at the Néel temperature and then begins to decrease for a few Kelvin, before increasing further to the lower temperature transition. The T_{LT} transition, present in the original data, is now shifted to ~150 K with a much higher magnetization of 0.098 μ_B/f.u. The curve continues to increase after the transition on cooling to 10 K.

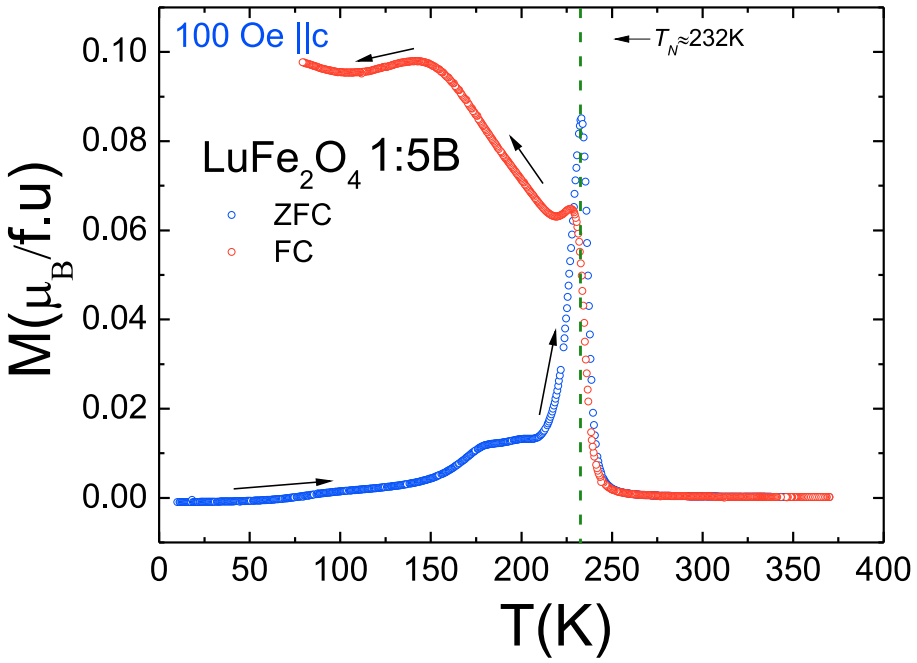

Figure 3.16: Remeasure of Magnetization
ZFC and FC data from the crystal grown in CO:CO_2=1:5 (1:5B), after heating to 400 K during the specific heat measurement.

3.3.3.2 Specific Heat

A remeasure of the specific heat was performed on the 1:5B crystal after the first measurement to 400 K, shown in figure 3.17. The red curve, measured between 150 and 400 K represents the specific heat before heating above 400 K, the black curve measured between 200 and 350 K shows the specific heat measured after heating to 400 K. There is only a very slight increase in the overall specific heat of the remeasured curve by approximately 3 %. There are no indications of any temperature shifts at both the main Néel temperature at T_N=232 K or the T_{CO}=314 K transition.

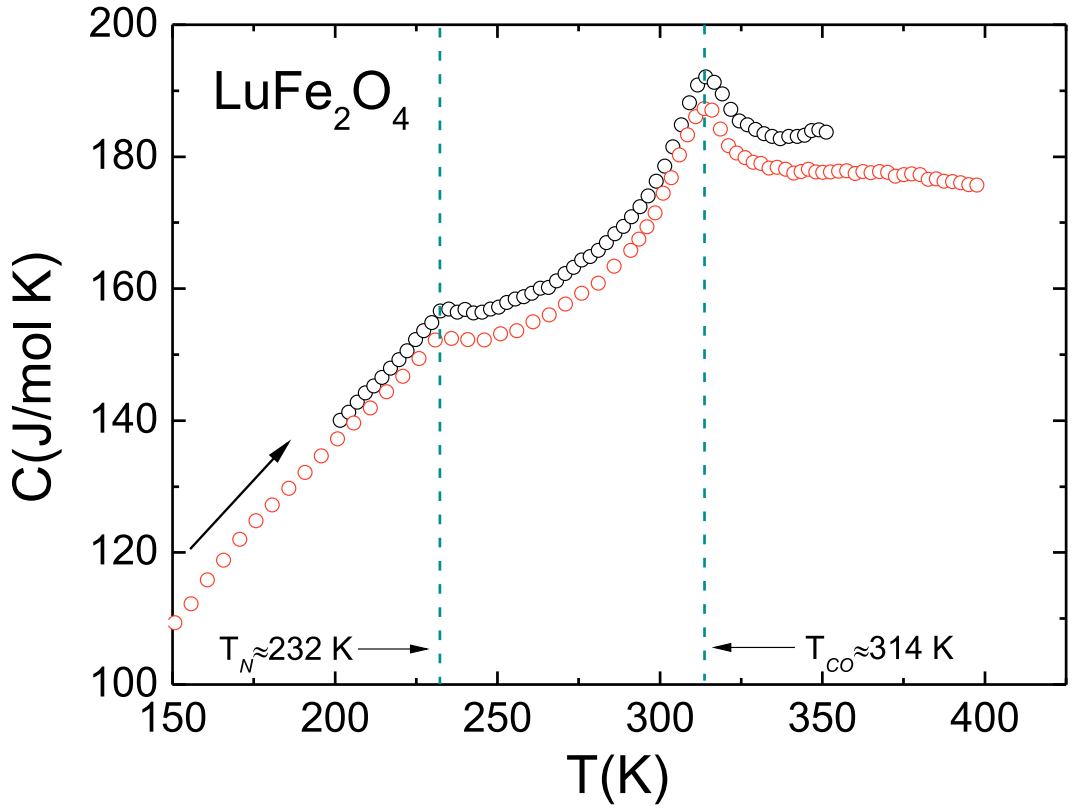

Figure 3.17: Remeasure of Specific Heat
A remeasure of the specific heat after heating the 1:5B crystal to 400 K. Red curve: initial specific heat measurement from 150 to 400 K. Black curve: remeasure of specific heat after heating crystal to 400 K (black arrow indicates direction of heating).

3.3.4 Single Crystal X-Ray Diffraction

Single-crystal x-ray diffraction was performed on small crystals (microgram range) of $LuFe_2O_4$ grown in $CO:CO_2$=1:3 and $CO:CO_2$=1:5 gas atmospheres. A crystal is mounted and measured initially with a test experiment, which collects a range of reflections from reciprocal space during a five minute scan. The reflections are then mapped out in reciprocal space to show a room temperature image of the Bragg reflections, allowing for the determination of single crystal quality i.e the absence of multiple grain boundaries and twinning. By inserting the known lattice parameters into the *Crysallis*^{Pro} software, the structure and lattice parameters can be allocated to the reflections recorded in the pre experiment, before running a longer measurement. The $LuFe_2O_4$ crystals selected from each growth for the longer measurement were initially cooled to 90 K (base temperature for the cryojet with nitrogen cooling), where a program is created to measure Bragg reflections at four temperatures on warming: 90 K, 230 K, RT and 350 K.

The data is then processed using the same *Crysallis*^{Pro} software, to collect all the Bragg reflections into a reciprocal map at each temperature. The data shown in figure 3.18 represents reciprocal maps taken along the hhl and hh0 direction at 90 K (top) 230 K, RT and 350 K. The CO present in the hhl plane (based on previous neutron scattering measurements, which indicated a strong spin alignment along the c axis, described in section (3.1)) is shown in figure 3.18a, and highlights the diffracted intensity in the hhl plane of the crystal grown in the $CO:CO_2$=1:3 atmosphere. The weak onset of 2D CO is present at 350 K along the (1/3, 1/3, l) and (2/3, 2/3, l) line. On cooling below 300 K the diffuse CO lines become stronger, reaching a maximum intensity at 90 K, but no sharp reflections, suggesting no long-range CO emerges at any temperature. This is very different to the results obtained from the single crystal x-ray diffraction performed on the crystal grown in $CO:CO_2$=1:5. For the latter, the first appearance of weak CO is seen at 350 K, but on cooling further to 300 K CO spots start to appear, indicating the presence of 3D CO order. Below 300 K at 200 K and 90 K the intensity of intricate CO pattern along the (1/3, 1/3, l) and (2/3, 2/3, l) becomes much more intense.

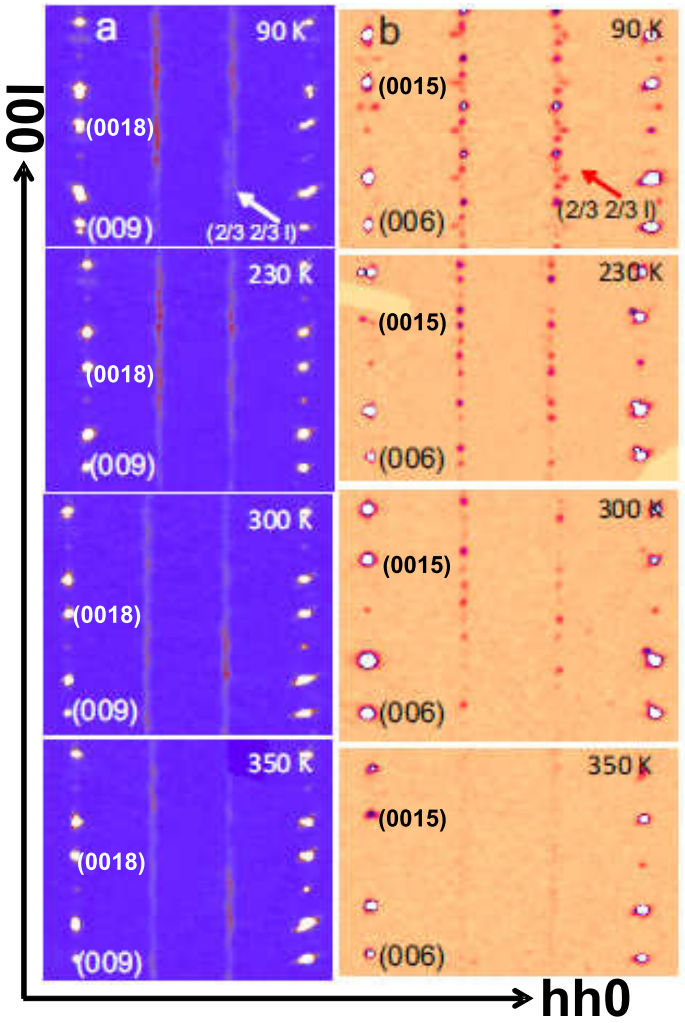

Figure 3.18: Single Crystal X-Ray Diffraction
Single crystal x-ray diffraction images at 90 , 230 , 300 and 350 K of (a) $LuFe_2O_4$ grown in $CO:CO_2$=1:3 and (b) $LuFe_2O_4$ grown in $CO:CO_2$=1:5

3.4 Discussion

3.4.1 $LuFe_2O_4$ grown in $CO:CO_2$=1:3

The challenge of growing good stoichiometric single crystals of $LuFe_2O_4$ has, in the past been difficult to achieve. However, based on these previous studies (41)(42) it has been possible to isolate the optimal $CO:CO_2$ gas ratio for synthesis and crystal growth. Macroscopic measurements of magnetization, specific heat and single crystal x-ray diffraction of two single crystals grown by (68) in $CO:CO_2$=1:3 (1:3) and $CO:CO_2$=1:5 (1:5) show very different characteristics. The magnetization data of the crystal grown in the 1:3 gas ratio exhibited only one transition at 202 K, as described in section (3.4). This broad feature does not occur at T_N=235 K or at T_{LT}=175 K and is more indicative of a spin glass state with the presence of more than one magnetic phase (69). Studies on $LuFe_2O_4$ conducted by Wang *et al.*(64), present similar results to that of the (1:3) crystal. Despite their use of traveling solvent floating zone method to prepare single crystals of $LuFe_2O_4$, which produced over-doped crystals with excess oxygen to that of the (1:3), presented macroscopic measurements of magnetization and specific heat that corroborate directly with our macroscopic measurements. Figure 3.19a shows magnetization data from Wang *et al.*, and figure 3.19b shows the magnetization data from the crystal grown in the 1:3 gas ratio. Although their main transition appears at 236 K compared to the 202 K apparent in our data, the peak shape and magnitude are very similar. Moreover, their a.c susceptibility results indicate a large frequency dependence at this temperature indicating the possibility of multiple magnetic states (64). The magnetization is slightly higher in the magnetization data from Wang *et al.*, where T_N reaches ~0.17 emu/g as apposed to the 202 K transition reaching ~0.08 emu/g. The only difference between our data and that obtained by Wang *et al.*, for the specific heat of $LuFe_2O_4$, is the main Néel transition which occurs at 237 K and 232 K in each data set, respectively. The peak is much sharper and well defined in their data representing a more ordered magnetic state than the crystal grown in the (1:3) gas ratio, at that temperature.

The absence of the CO transition below 330 K in the specific heat data also provides strong indications of off-stoichiometry, see figure 3.20a, as our crystal grown in the 1:5 gas ratio, which not only exhibits the main Néel and magnetoelectric structural

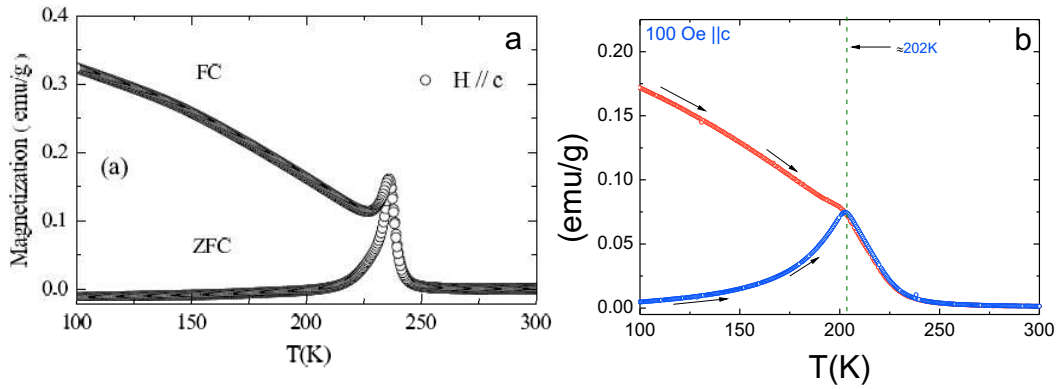

Figure 3.19: Magnetization Comparison for $LuFe_2O_4$
(a) ZFC and FC magnetization of single crystal $LuFe_2O_4$, with an applied field of 100 Oe parallel to the *c*-axis. Reproduced from Ref (64). (b) ZFC and FC data of $LuFe_2O_4$ grown in $CO:CO_2$=1:3.

transition in the magnetization data, but a sharp peak at 314 K is also present in the specific heat data (refer to section (3.4.1)). The CO transition, which appears as a very small, smeared out feature in our data at 314 K, is seen as a broad hump around 320 K in their data. It is however, evident from both sets of magnetization and specific heat data, that the stoichiometry obtained within the crystals grown by Wang *et al.*, is slightly better than that achieved with the crystal grown in the (1:3) gas ratio, but still exhibits very similar magnetic and CO behavior.

Both the specific heat and single crystal x-ray diffraction, which shows only diffuse scattering along the (1/3, 1/3, l) line, support the absence of a transition to long-rang order. Similar results were previously obtained by Yang *et al.*, through TEM (70). By growing crystals in two different gas ratios $H_2:CO_2$=1:7 and $H_2:CO_2$=1:1.9, they were able to see large differences in the CO modulations along the (1/3, 1/3, l) line at room temperature. They discovered that diffuse scattering was stronger with the crystals grown in the less oxidizing atmosphere $H_2:CO_2$=1:1.9 compared to that of the crystal grown in the more oxidizing gas ratio $H_2:CO_2$=1:7, which exhibited slightly weaker diffuse scattering. Nevertheless, its seems apparent that the prerequisite gas mixtures for both $H_2:CO_2$ and $CO:CO_2$ ratios produce very different outcomes with respect to off-stoichiometric crystals. It is evident from the macroscopic measurements performed

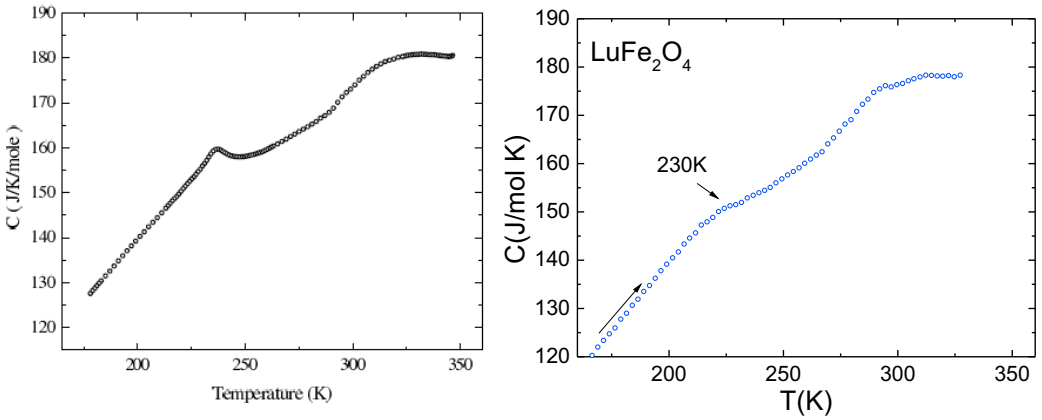

Figure 3.20: Specific Heat Comparison for $LuFe_2O_4$
(a) Specific heat of $LuFe_2O_4$ Single crystal, (b) Specific heat data of $LuFe_2O_4$ grown in $CO:CO_2$=1:3. (a) Reproduced from Ref (64).

on the (1:3) $LuFe_2O_4$ single crystal with a cross comparison of recently published data, that the use of a less oxidizing gas ratio promotes poor magnetization and CO within this system.

3.4.2 $LuFe_2O_4$ grown in $CO:CO_2$=1:5

Single crystals grown in the $CO:CO_2$=1:5 gas ratio provide a much better insight into both the magnetic and charge order present in the $LuFe_2O_4$ system. There have been few reports of crystals exhibiting both a magnetostructural transition and the main Néel transition in magnetization data, based on the difficulty to grow $LuFe_2O_4$ in the correct atmospheric conditions. However, it is clear from the data shown in figure 3.21a, that a near stoichiometric crystal grown in the (1:5) gas ratio was achieved. The initial reports by Iida *et al.* (41) on polycrystalline $LuFe_2O_4$ gave an indication of the T_{LT}=175 K transition and the anomalous field heating effect, as described in section (3.2.1). It was much later by Groot *et al* (65). that experimentation with different oxygen partial pressures during crystal growth, highlighted a crystal of similar but better stoichiometric quality to those initially obtained by Iida *et al.* The FC magnetization data shown in figure 3.21b, was taken from two crystals from the same growth, but show varying quality. Crystal 1 (red curve) is of poorer stoichiometric quality than that

of crystal 2 (blue curve) based on the absence of the magnetostructural transition at 175 K, which is present in crystal 2. The FC magnetization data shown in figure 3.21a was measured on the (1:5B) crystal and is directly comparable to crystal 2, where there is only a slight peak of shift of 1-2 K, in the main Neel temperature and magnetostructural transition. The peak definition in the low temperature transition is sharper in the (1:5B) crystal which also exhibits a slightly higher magnetization at the neel temperature compared to that of crystal 2, indicating slightly better stoichiometry than that produced by de Groot *et al.*. Despite this, both magnetization curves provide a crystal quality which is closer to the correct stoichiometry than all previous publications on $LuFe_2O_4$, highlighting the two transitions present, which has in the past been difficult to obtain through poor crystal quality.

The specific heat measurement of the (1:5B) crystal corroborates well with the magnetization data, showing a sharp transition at T_N=232 K. The sharp peak at 314 K indicates the onset of CO (refer to section (3.4.1)), with a notable improvement of the peak definition compared to that of the specific heat data taken from the (1:3) crystal. Single crystal x-ray diffraction further supports the presence of charge order below 350 K, shown in section (3.4.3), which is seen in the specific heat data at 314 K. Charge order spots on the diffraction images, reach the strongest intensity at 90 K and are indicative of 3D CO (66).

3.4.3 Changes in stoichiometry

On performing the specific heat measurement, the crystal was taken to 400 K. Based on this systems large sensitivity to oxygen stoichiometry, heating the crystal beyond 350 K can cause shifts within the oxygen coordination of the unit cell. Figure 3.22a shows the magnetization measurement performed on the (1:5B) crystal after the 400 K specific heat measurement. There is a large difference in the magnitude of the magnetization on both FC and ZFC data compared to the original magnetization measurement (refer to section (3.4). The FC data has the most notable change on cooling below the Néel temperature, where the original magnetization curve shows a decrease in the magnetic moment before the T_{LT} transition at 175 K. However, the FC curve reaches a maximum magnetization of 0.068 μ_B/f.u at T_N=232 K, and starts to decrease for a few Kelvin before exceeding the magnetization of T_{LT} in the original magnetization data.

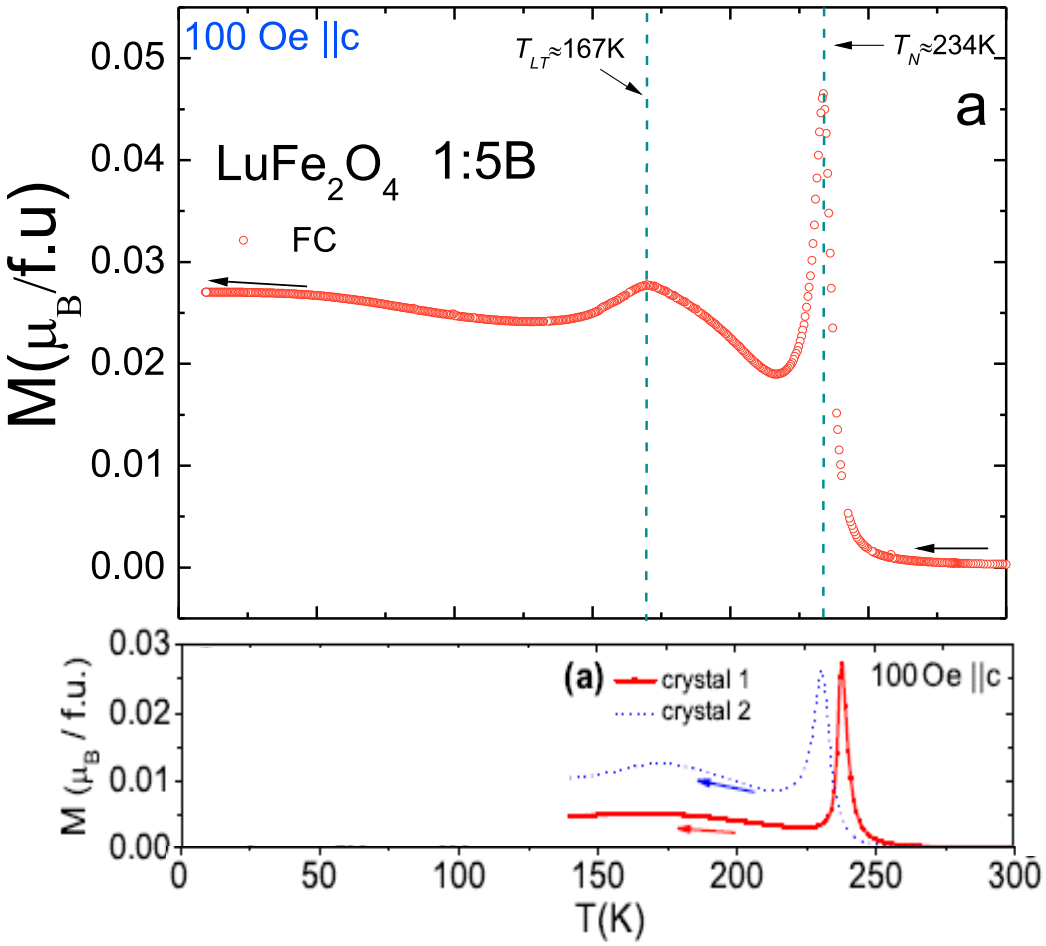

Figure 3.21: Magnetization comparison of $LuFe_2O_4$ grown in CO/CO_2=1:5 (a) FC magentization data of $LuFe_2O_4$ (1:5B) crystal, (b) FC Magnetization data of two crystals of varying stoichiometry, Reproduced from Ref. (65).

Moreover, the 175 K transition, present in the original data is now shifted to 150 K with a much higher magnetization, where the curve continues to increase after the T_{LT} transition on cooling to 10 K. Figure 3.22b shows magnetization and AC susceptibility (inset) of a $LuFe_2O_4$ single crystal grown in a $CO:CO_2$ gas atmosphere (71). The magnetization data of ZFC and FC in a temperature range 10-300 K, shows very similar characteristics to that of the (1:5B) crystal after heating to 400 K. Despite no previous report of heating the crystal above room temperature, the difference in the FC data is similar to that of recently published data (71). The affect on the FC data may stem from the use of a higher temperature during the crystal growth procedure, as well as the $CO:CO_2$ mixture. The AC susceptibility shows a strong frequency dependence indicating a spin glass state at 230 K, which contradicts measurements on $LuFe_2O_4$ single crystals exhibiting 3D magnetic order below 230 K (62).

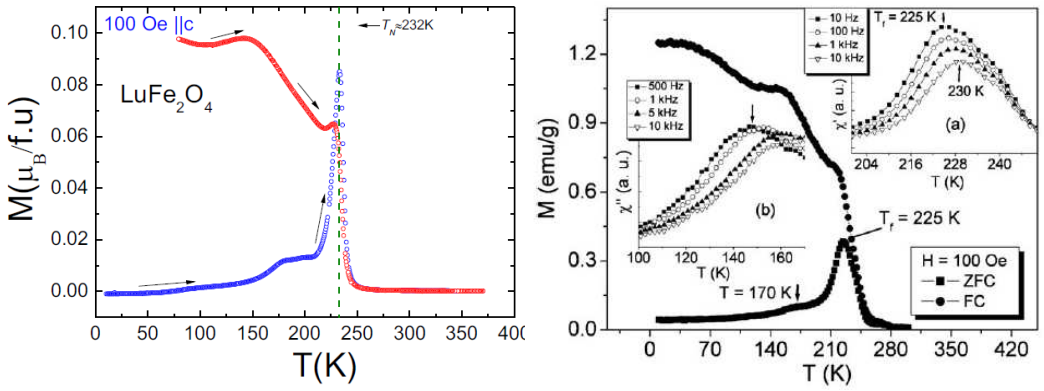

Figure 3.22: Change is Stoichiometry: A remeasure of the Magnetization
(a) a remeasure of the ZFC and FC magnetization after heating the crystal to 400 K, (b) Comparable magnetization data on ZFC and FC in applied field of 100 Oe: inset AC susceptibility results at four different frequencies. (b) was reproduced from Ref (71).

A remeasure of the specific heat, after initially measuring to 400 K shows only a small increase in the overall specific heat capacity, shown in section (3.4.2.2). Both curves follow the same trend, exhibiting sharp peaks at both T_N and T_{CO}.

3.5 Stoichiometry, Magnetism and CO

There is a large variation in the magnetism and CO between $LuFe_2O_4$ crystals grown in $CO:CO_2$=1:3 and $CO:CO_2$=1:5. From past experimentation into varying the oxygen

stoichiometry, by using an oxygen partial pressure environment during crystal growth has shown that; $LuFe_2O_4$ grown in more oxidizing gas ratio produces a sharper transition at T_N as well as exhibiting the T_{LT} magnetostructural transition, and is seen clearly in the magnetization data from (42)(32). A sharp peak in the the specific heat data and the presence of CO Bragg peaks along the (1/3, 1/3, l) support the evidence of 3D CO (62). In samples grown in an oxygen reducing atmosphere, in this case $CO:CO_2$=1:3, transitions present in the magnetization data are broad and often show an absence of the magnetostructural transition. The specific heat data exhibits only a broad maximum near T_{CO}, where single crystal x-ray diffraction shows diffuse lines along the (1/3, 1/3, l) line, indicating only 2D CO. Based on the the magnetization, specific heat and single crystal x-ray diffraction results from the single crystal grown in $CO:CO_2$=1:5 and those obtained by deGroot *et al.* (65) on a good quality crystal, a close comparison can be made. This indicates that the current investigations have produced the best stoichiometric $LuFe_2O_4$ crystals since its discovery. An oxygen deficiency is caused with the $CO:CO_2$=1:3 compared to that of the $CO:CO_2$=1:5. This deficiency causes a breakdown of CO based on oxygen vacancies within the crystal structure, causing a less energy favorable arrangement of Fe-O, i.e reduced order of ions preventing long range CO. Oxygen deficient samples will also greatly affect the magnetic properties due to a weaker coupling between the Fe and O ligands, reducing long range magnetic order. Vacancies within the Lu-O layer will cause possible deformations in the unit cell, promoting a less energy favorable arrangement of atoms, also reducing the magnetism and CO. Based on the magnetization data from both the (1:3) and (1:5) crystals, it seems evident that the (1:5) crystal is the closest to optimum oxygen stoichiometry, and supported by recent results from deGroot *et al.* (65). However, the use of an oxygen rich environment during crystal growth can cause an excess of oxygen, resulting in over-doped $LuFe_2O_4$, which also dampens the magnetic and CO features and was seen clearly by Michiuchi *et al.* (42)

Further investigation into the changes in stoichiometry within $LuFe_2O_4$ upon heating to 400 K are required, to understand the FC data shown in figure 3.22, and the change in magnetic behavior. The largest difference observed when heating to 400 K is seen in the magnetostructural transition, which may indicate a change in both the AFM and fM phases present, where a change in the oxygen position within the

crystal from heating causes a change in the Fe-O coordination. Although there are no current investigations to measure the true oxygen stoichiometry of both the (1:3) and (1:5) crystals, the final aim of this research is to quantify the correct oxygen content of $LuFe_2O_4$ in order to obtain the best quality crystal. Therefore careful analysis using TGA (Thermo-Gravimetric Analysis) on crystals grown in the (1:3) and (1:5) may begin to uncover the true oxygen content.

4

Multiferroic Properties of $YbFe_2O_4$

4.1 New Investigations into $YbFe_2O_4$

A renewed interest into the rare earth series resulting from extensive new findings within the $LuFe_2O_4$ system has prompted new investigations into $YbFe_2O_4$, to uncover the mechanisms which govern the magnetic and electrical properties. $YbFe_2O_4$ has a rhombohedral structure with lattice parameters a=b=3.455 Å, c=25.054 Å, α=β=90 °C and γ=120 °C and space group R$\bar{3}$m. The first crystals of $YbFe_2O_{4-\delta}$ were grown in 1974 by Kimizuka et al., where they produced platelet crystals using a H_2:CO_2 partial pressure (43). It was much later in 1982, when the first magnetization measurements were performed on $YbFe_2O_4$ single crystals grown in different oxygen partial pressure atmospheres (see section 1.2.1.3) (45). Mössbauer spectral studies in 1988 provided the first insight into the magnetic structure. They described $YbFe_2O_4$ as a two-dimensional antiferromagnet on a triangular lattice, where a simulation of three magnetic structure types were formed, based on the the Mössbauer spectrum measured at 4.2 K (46). In 2007, investigations of the magnetic and dielectric properties of polycrystalline RFe_2O_4 (R= Yb and Lu) series by Yoshii *et al.*, synthesized in a CO:CO_2 gas atmosphere, provided the first clear magnetization data, revealing three transition points between 10 to 300 K, shown in figure 4.1a (48). The first upturn of the magnetization at around 250 K indicates the appearance of ferrimagnetic order of the Fe spins. A measurement of the thermo-remanent magnetization marked by (TRM) in figure 4.1a was also performed. The point at which the TRM curve reaches a zero magnetization,

at ∼250 K, highlights the onset of the Néel transition.

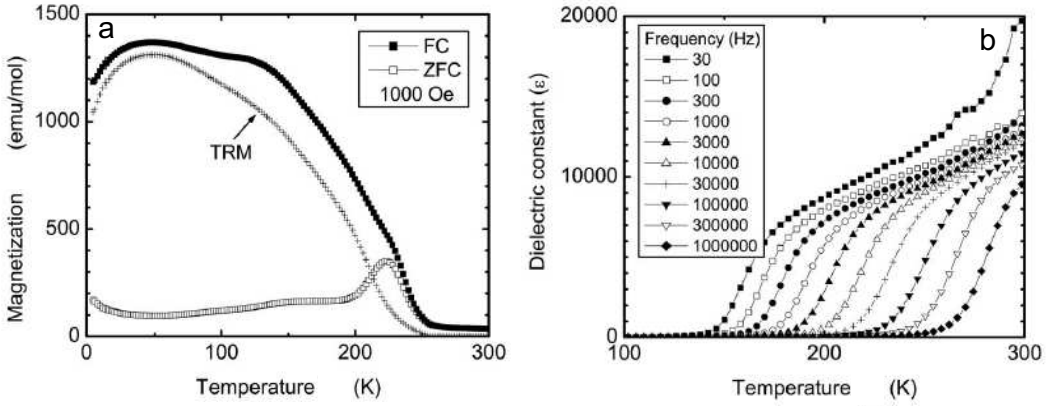

Figure 4.1: Recent Magnetization and Dielectric Studies on Polycrystalline $YbFe_2O_4$ (a) ZFC and FC magnetization data measured with an applied field of 1000 Oe, TRM curve marked with crosses. (b) Dielectric constant as a function of temperature, at ten different frequencies. (48).

Dielectric measurements were also performed by Yoshii *et al.*, on the same $YbFe_2O_4$ polycrystalline sample. The dielectric constant ε was measured in the frequency between 30 Hz and 1 MHz as a function of temperature. A small bump in the data is seen only in the low frequency of 30 Hz at ∼270 K, which corresponds to the main Néel transition at ∼225 K in the magnetization data, shown in figure 4.1b (48). A large dielectric distribution of frequencies is seen between 150 and 250 K and can be interpreted as the position in which each curve levels to ϵ∼0. $YbFe_2O_4$ also exhibits a very high dielectric constant of 20000 at 30 Hz and room temperature. Energy-filtered transmission electron microscopy was performed later that year by Murakami *et al.*, on $YbFe_2O_4$ single crystals grown in a CO/CO_2 gas atmosphere, via floating zone method. Through the use of dark field imaging, by using a spot of diffuse scattering along the (1/3, 1/3 l) line, the presence of nanometer-sized charge-ordered domains were revealed and are shown in figure 4.2, where Murakami *et al.*, discovered that on cooling from 353 K (a) to 295 K (b) the nanometer charge order domains do not increase in size on the dark field images (49).

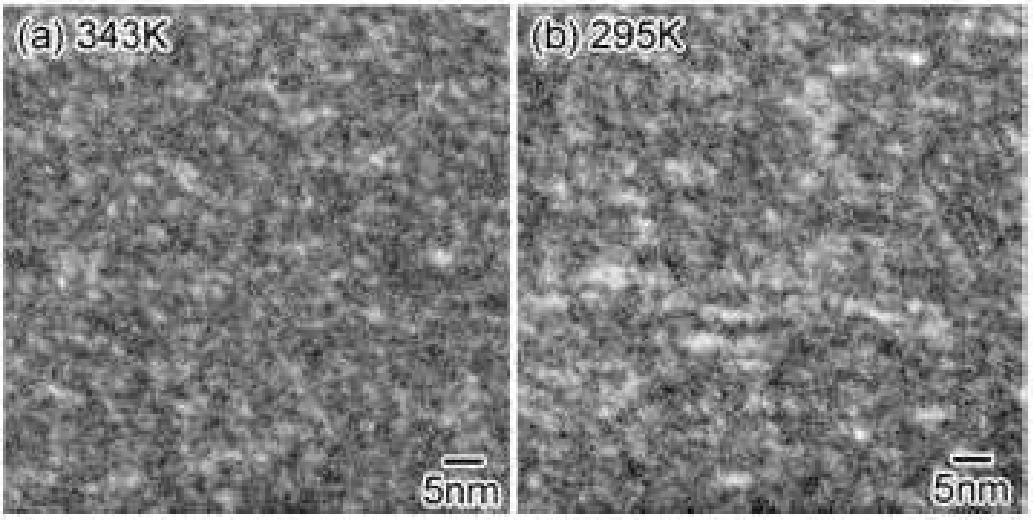

Figure 4.2: TEM Dark Field Images
Change in the dark-field image which was obtained by using a diffuse spot taken along the (1/3, 1/3, 11/2) at 343 and 295 K. Reproduced from Ref (49).

The Full Width Half Maximum of a peak taken from the electron diffraction intensity profile on cooling, shown in figure 4.3a was analyzed as a function of temperature, see figure 4.3b, and highlighted that the domain size, even at low temperatures does not exceed 10 nm. This result demonstrates that based on the small nano-sized charge order domains, it is difficult to develop long-range charge order in the presence of frustration on the triangular lattice, resulting in only diffuse Bragg lines along (1/3, 1/3, l) (49)(60).

A recent study by Hearmon *et al.* (50), focused on the CO present within $YbFe_2O_4$. Based on high energy x-ray diffraction, Hearmon *et al.* propose that the CO phase in fact exhibits an incommensurate charge-density wave and therefore cannot be ferroelectric, because the electrical dipole moments are also incommensurately modulated. The change between continuous and broad helices of scattering at the CO transition is attributed to three-dimensional fluctuations of the direction of the ordering wave vector, shown in figure 4.4. There is no real super structure peaks present, indicating an absence on long-range CO, likely due to imperfect stoichiometry similar to $LuFe_2O_4$ (see section (4.1)). This result corresponds to the initial investigations by Ikeda *et al.* into $LuFe_2O_4$ and their production of a magnetic and CO phase diagram, isolating the

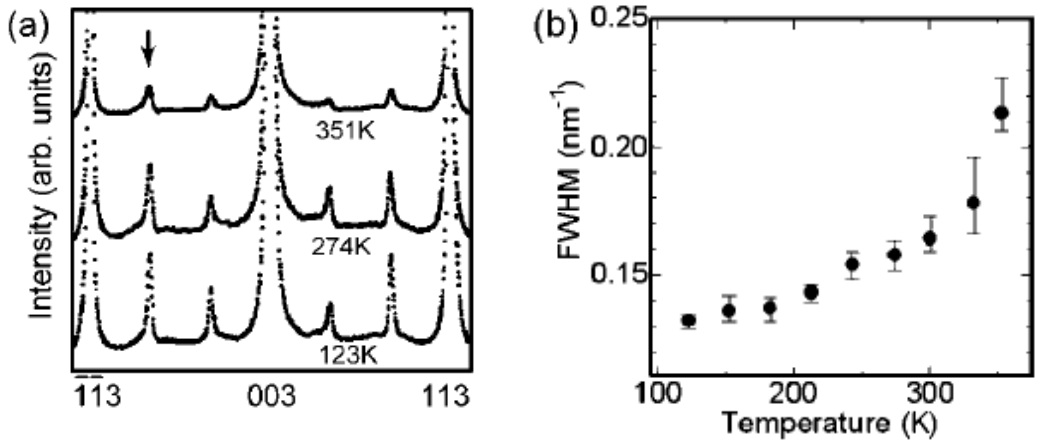

Figure 4.3: Electron Diffraction
(a) Change in the intensity profile of electron diffraction with cooling. (b) Temperature dependence of the full width at half maximum (FWHM) measured for the peak indicated by the arrow in (a). Reproduced from Ref (49).

CO phase below 230 K to be 3D-CDW (60).

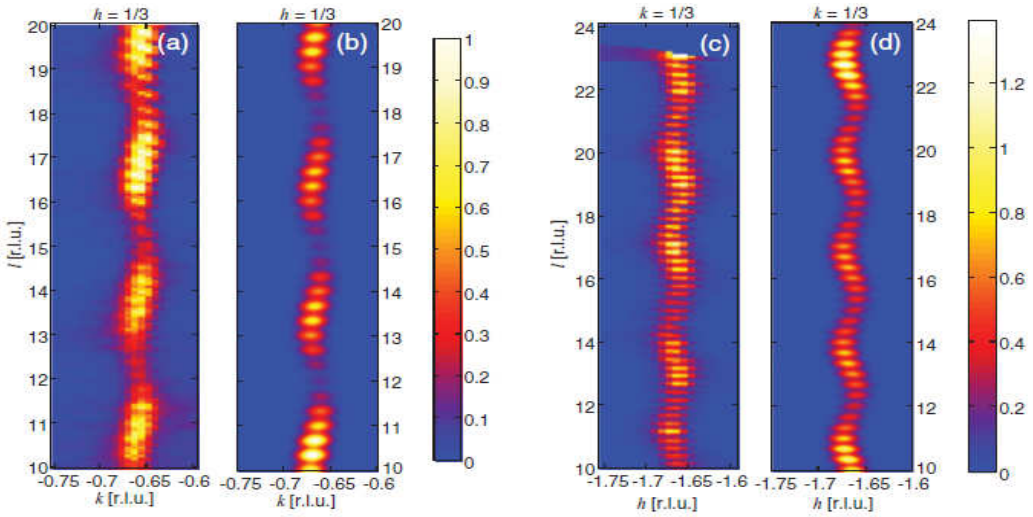

Figure 4.4: High Resolution X-ray Diffraction of $YbFe_2O_4$
Reciprocal space cuts (a) and (c) and simulations (b) and (d) at T = 150 K. Reproduced from Ref (50).

The current lack of available literature on $YbFe_2O_4$, suggests no samples of suffi-

ciently good stoichiometry to exhibit 3D CO were produced. The focus of this thesis is to produce samples of better stoichiometric quality to those previously published. The following sections will introduce magnetization data which exhibits many more features than those of previously published data (45)(48)(72). New macroscopic measurements of specific heat, single crystal x ray diffraction, ac susceptibility and Mössbauer spectroscopy of crystals grown in $CO:CO_2$=1:3 and $CO:CO_2$=1:3.5 will also be presented.

4.2 Results

Since the first successful synthesis and crystal growth of $YbFe_2O_4$ (43), very few subsequent investigations have been performed. Based on the difficulty of synthesis and crystals growth as well as the need to use a $CO:CO_2$ oxygen partial pressure atmosphere, the true nature of the magnetism and CO within this compound have never truly been uncovered. The first insight into stoichiometric properties of the rare earth series stemmed from polycrystalline growth of YFe_2O_4 in varying oxygen partial pressures, which lead to the realization that off-stoichiometric powders suppressed the magnetic and CO characteristics (39). This discovery provided a renewed interest into the rare earth series, in particular $LuFe_2O_4$, which highlighted that off-stoichiometric crystals, produced better quality crystals, in contrast to that of the YFe_2O_4 which must be near stoichiometric. After many years of experimentation and understanding, as to the effects of varying $CO:CO_2$ oxygen partial pressure during synthesis and crystal growth of $LuFe_2O_{4-\delta}$, new and recent studies on $YbFe_2O_4$ were performed. This provided the incentive to grow $YbFe_2O_{4-\delta}$ in three different oxygen partial pressure atmospheres: $CO:CO_2$=1:5, $CO:CO_2$=1:3.5 and $CO:CO_2$=1:3 to investigate the variation these gas ratios for synthesis would have on the characteristics.

Powder x-ray diffraction of $YbFe_2O_4$ grown in the $CO:CO_2$=1:3, highlighted that it was in fact single phase and directly comparable to the initial diffraction performed on the polycrystalline powder. This result was further supported by a Rieveld refinement, shown in section (4.3). In order to perform macroscopic measurements for magnetic and CO characterization, Laue diffraction was performed. While scanning the entire length of the crystal, it was clear that there were no large sections of single crystal, but rather an indication that a number of small domains were present. As it was not possible to isolate a crystal using this method, parts of the boule were cut and then smashed to find single crystals. With careful observation and the knowledge that boules grown within the rare earth series, cleave along the c-axis, small crystals ranging between 3-60 mg were obtained and checked with Laue diffraction. A single crystal of mass 3.5 mg was used for the majority of the macroscopic measurements performed, with the only exception of single crystal x-ray diffraction, which requires a much smaller crystal within microgram range. The Mössbauer spectroscopy of $YbFe_2O_4$ was measured using

powdered single crystal.

4.2.1 Sample Preparation and Crystal growth

Polycrystalline powders of $YbFe_2O_{4-\delta}$ were synthesized from stoichiometric quantities of Yb_2O_3 and Fe_2O_3. In total five batches were prepared using three different heating stages. The heating procedure, shown in table 4.1 gives the three different heating stages: batch A, B, and C which are in chronological order of production. All batches were subjected to an initial 48 h heating in order to aid synthesis before being removed from the furnace, reground and heated again. The second heating varied, for batch A a longer heating time of 24 h was used, whereas batch B and C were heated for only 12 h. This shorter heating time was used solely for increasing the speed of powder synthesis before rod formation and crystal growth. The powders were then reground after the second heating and formed into rods. The rods are then sintered for 12 h at the same temperature as during synthesis to strengthen them for crystal growth. Single crystals of $YbFe_2O_{4-\delta}$ were grown using the floating zone method, described in section 2.2. In order to obtain large single crystals of $YbFe_2O_{4-\delta}$ a slow growth rate of 1mm/h was used. Crystals were grown using three different gas ratios, $CO:CO_2$=1:5, $CO:CO_2$=1:3 and $CO:CO_2$=1:3.5.

Powder Batch	1st Heating	2nd Heating	3rd Heating (Rod)	Crystal Growth Atmosphere
A	1200°C, 48 h CO/CO_2=1:3	1200°C, 24 h CO/CO_2=1:3	1200°C, 12 h CO/CO_2=1:3	CO/CO_2=1:5
B	1200°C, 48 h CO/CO_2=1:3	1200°C, 12 h CO/CO_2=1:3	1200°C, 12 h CO/CO_2=1:3	CO/CO_2=1:3
C	1200°C, 48 h CO/CO_2=1:3	1200°C, 12 h CO/CO_2=1:3	1200°C, 12 h CO/CO_2=1:3	CO/CO_2=1:3.5

Table 4.1: Powder Synthesis Table
Powder synthesis table for each type of crystal growth. Columns 2, 3 and 4 describe the temperature, duration of heating and gas ratio used to synthesize the powders before rod formation and final sintering.

Single crystal growth via the floating zone method requires time, patience, and trial

and error in order to produce large single crystals. The use of a single crystal as a seed will maximize the chances of producing large single crystals by providing a specific orientation early as the polycrystalline feed rod passes through the molten zone and crystallizes. In the first floating-zone growth a polycrystalline seed of $LuFe_2O_{4-\delta}$ was used based on its isostructural properties. Previous crystal growth attempts with dense materials, in particular previous work completed on $LuFe_2O_{4-\delta}$ (68) evidenced difficulties with the stabilization of the molten zone. To improve the homogeneity of the rod a fast scan was performed during the first crystal growth of $YbFe_2O_{4-\delta}$. This technique passes the molten zone through the entire feed rod at a very fast speed, between 10-15 mm/h. This speed is too fast for the formation of a single crystal but will melt the polycrystalline powder evenly, producing a strengthened rod with a homogenous density along its length. The gas atmosphere used for the first fast scan and crystal growth was $CO:CO_2$=1:5 only for A and not for B and C.

Despite preemptive measures to improve the quality of growth using a fast scan, the first crystal growth A was not stable. Initial difficulties were encountered in forming the molten zone. The power input was adjusted regularly, reducing the heat power from a 77.7 %, just above the melting point of the material at the start of the growth to 74.3 % at the end of the growth, before separation of seed rod from feed rod. A second attempt at crystal growth using a $YbFe_2O_{4-\delta}$ seed from the first crystal growth was performed. The $CO:CO_2$=1:5 was maintained but with no initial fast scan. Problems occurred when melting the feed tip. The region just above the melted tip of the feed rod began to crack, therefore a higher power of 80.2% was used to melt the tip. Once the tip had become fully molten a zone was formed and the power was reduced to 79.9%. The temperature was again adjusted regularly as the zone was not completely stable, the growth rate was also increased and decreased for the duration of the crystal growth which improved the molten zone stability.

The third and fourth crystal growth from batch B was performed with CO/CO_2=1:3. A polycrystalline seed rod of $LuFe_2O_{4-\delta}$ was used for the third crystal growth. No fast scan was performed and a heating power of 73.7% was required to melt the tip of the feed rod, much lower than that of the two previous crystal growth attempts. Here a stable molten zone was formed and only small adjustments to the power were made

throughout the growth. The fourth crystal was grown using a $YbFe_2O_{4-\delta}$ polycrystalline seed, taken from the third crystal growth feed rod. The power input to melt the tip of the feed rod was slightly higher at 74% than with the previous growth and the temperature was eventually lowered to 70.4% by the end of the growth.

The fifth crystal growth from batch C was done in $CO:CO_2$=1:3.5 using a polycrystalline seed rod taken from the fourth growth. The molten zone was formed with a heating power of 73.2% and stable at that temperature until the last day of crystal growth. The zone broke with 1 cm left of polycrystalline feed rod. In order to ensure complete consistency during crystal characterization, the first crystal from batch A and B was selected for each macroscopic measurement performed.

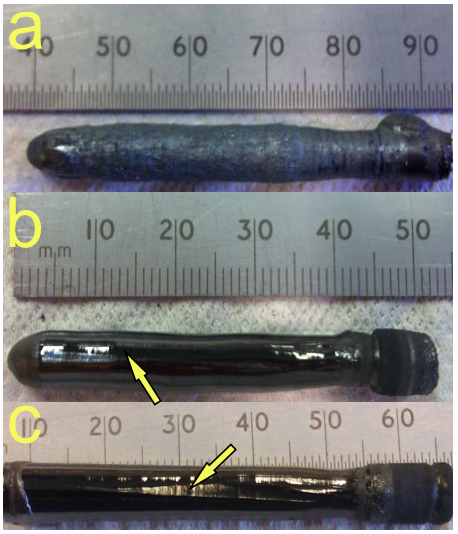

Figure 4.5: $YbFe_2O_{4-\delta}$ Crystal Boules
(a) Crystal grown in $CO:CO_2$=1:5, (b) crystal grown in $CO:CO_2$=1:3, (c) crystal grown in $CO:CO_2$=1:3.5.

The crystal boule grown in the $CO:CO_2$=1:5 atmosphere was ~40 mm in length with an average diameter of 6 mm. A crystal boule of length ~35 mm and a diameter of ~6 mm was grown in the $CO:CO_2$=1:3. A final crystal boule with a length ~42 mm and a diameter of ~6 mm was grown in $CO:CO_2$=1:3.5. These three boules are shown in figure 4.5. The boule grown in the $CO:CO_2$=1:5 atmosphere formed no

facets on cooling indicating a lack of crystallinity, however both boules grown in the $CO:CO_2$=1:3 and $CO:CO_2$=1:3.5 formed facets on cooling. Only one short facet of ∼15 mm was formed on the crystal grown in the $CO:CO_2$=1:3 however a large facet of ∼28 mm was formed on the crystal grown in $CO:CO_2$=1:3.5.

4.2.2 Powder X-Ray Diffraction

In order to check the phase formation and impurity levels of the synthesized $YbFe_2O_{4-\delta}$ samples, powder x-ray diffraction was used. Patterns were acquired at various stages throughout the synthesis and after crystal growth. During the preliminary synthesis stage, powder x-ray diffraction data were acquired using a Philips PW1720 x-ray generator, with 0.02° increments and a counting time of 3s/step. A Bruker D5005 was also used at times during the preliminary synthesis, with 0.02° increments and a counting time of 1s/step. For the refinement of the powder x-ray diffraction, more detailed data was collected at the end of the crystal growth on both the Bruker D5005 and a Huber Guinier G670 diffractometers. The preliminary x-ray diffraction patterns taken at the end of the sintering stage prior to rod formation and crystal growth are shown in figure 4.6. At this stage all three powders were prepared with the same initial heating period and gas ratio, the only exception being that the 2nd sintering time for batch B and C were shortened to 12 h.

The diffraction patterns were matched initially with the $YbFe_2O_4$ data published by Kato *et al.* (73) to see if the main phase was present. A comparison was also made with diffraction patterns of the initial stoichiometric constituents Fe_2O_3 and Yb_2O_3. Once these had been checked, all possible phases such as $Yb_2Fe_3O_7$, $YbFeO_3$ $Yb_3Fe_5O_{12}$, FeO and Fe_3O_4 which could be present were compared to each diffraction pattern from batch A, B and C.

The x-ray diffraction pattern from batch A, which was sintered for a total time of 72 hours, matched very well with the $YbFe_2O_4$ published data. There is one very small FeO peak at 35 °, and only slight peak splitting on the high intensity angles between 29 and 36 °, indicative of mixed stoichiometric phases of $YbFe_2O_4$. The x ray diffraction obtained for batch B is very similar to that of batch A. The overall intensity of the pattern is less than batch A by ∼50%, where this as well as peak splitting stems

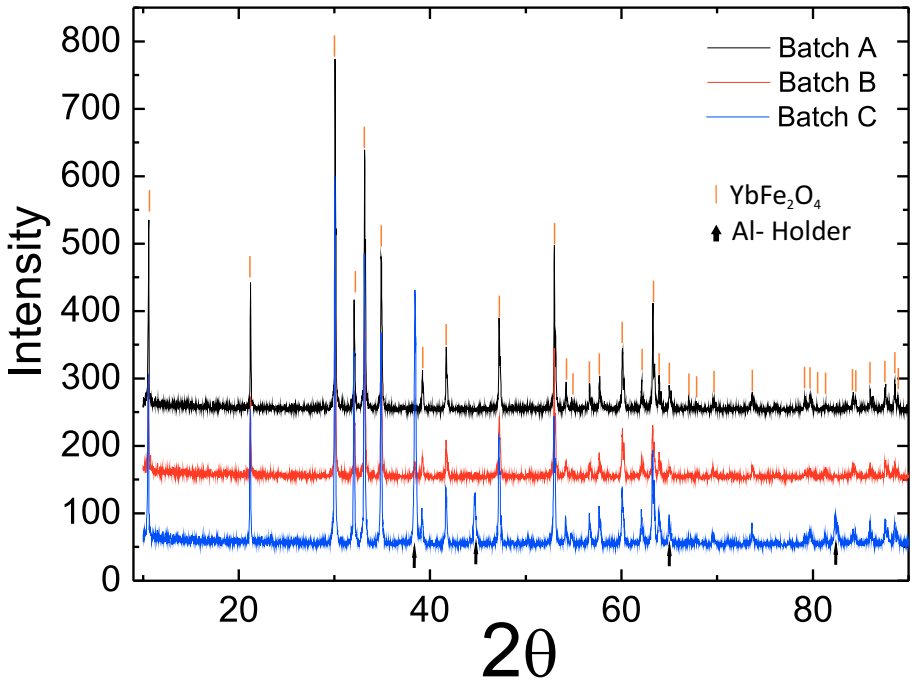

Figure 4.6: Powder Diffraction of Polycrystalline Batches.
Diffraction patterns from each method of powder synthesis, Bragg lines and arrows represent $YbFe_2O_4$ and Al phase peaks respectively.

from the shortened synthesis time of 60 h, reducing the solid state reaction time. The final diffraction pattern from batch C, which was synthesized in the same gas ratio and heated for the same duration of time as batch B, presented two large intensity peaks at 38.4 ° and 44.5 °, not from the main $YbFe_2O_{4-\delta}$ pattern. After comparing these peaks to the various phases described previously, there was no correlation to these two intense peaks. The sample holder used for D5005 x-ray diffractometer was made of aluminium and after comparing the diffraction pattern of Al from data published by Bourbia *et al.* (74), it was clear that the impurity peaks came from the sample holder. The powder diffraction data from batch A and B could be refinable to single phase $YbFe_2O_{4-\delta}$. Batch C can also be refined by including the Al impurity phase into the refinement to disregard those peaks from the main pattern.

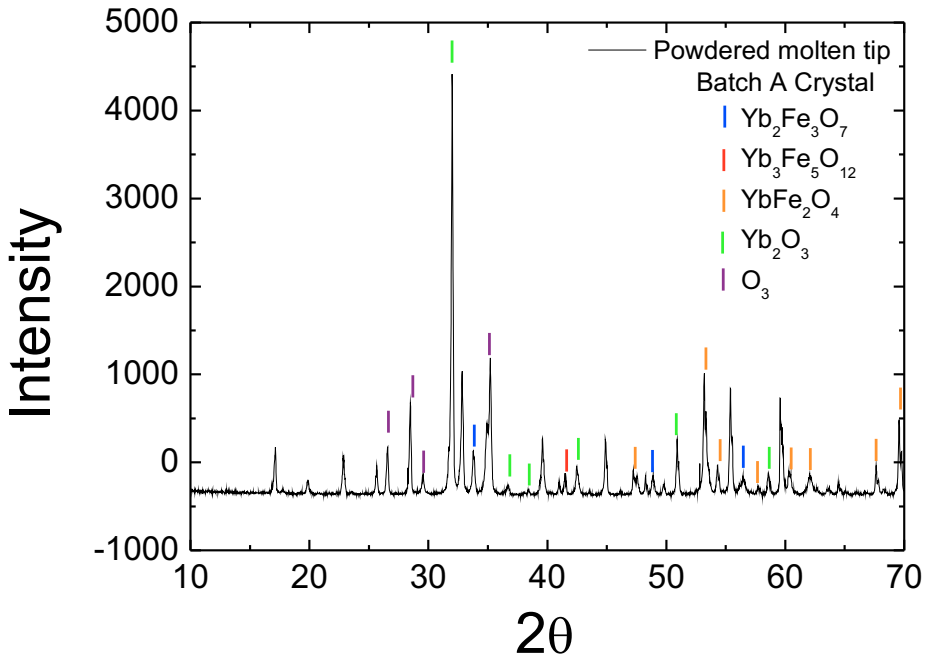

Figure 4.7: X-Ray Diffraction of Crystal Grown in $CO:CO_2$=1:5
Blue curve: powdered molten tip from crystal grown in $CO:CO_2$=1:5, different colored Bragg lines represent various phases present.

In order to check the phase purity of a newly grown crystal, a small section is cut

from the molten tip. This is the section of the crystal which is separated from the remaining feed rod at the end of the crystal growth. A diffraction pattern of the molten feed rod and the initial polycrystalline powder is shown in figure 4.7. It is clear that by using the $CO:CO_2$=1:5 gas atmosphere a complete phase breakdown is caused. A peak indexing of the powdered molten feed diffraction pattern reveals five phases; Yb_2O_3 , $YbFe_2O_4$, $Yb_2Fe_3O_7$ and $Yb_3Fe_5O_{12}$ and O_3 which are now present in the crystal. The $CO:CO_2$=1:5 gas ratio is more oxidizing than the $CO:CO_2$=1:3, which explains why there are so many high oxygen impurity phases. The first phase diagram of $YbFe_2O_4$ by Kimizuka *et al.* (44) highlights that phases beyond the stable $YbFe_2O_4$ denoted (n, m, l), (refer to section (1.2.1.3) for the $YbFe_2O_4$ phase diagram) will lead to oxygen deficient phases such as (p, l, y, h, i) or over-doped $YbFe_2O_{4.052}$, which may correspond to the peaks which were not identified for both binary and ternary phases.

The first successful crystal growth was achieved using batch B and growing the crystal in the $CO:CO_2$=1:3 gas ratio. The two diffraction patterns in figure 4.8 show both the polycrystalline powder and powdered molten tip from the crystal boule (separation of the feed from seed rod). The diffraction data of the powdered molten feed is comparable to that of published data from (75), only showing two small peaks at 36° and 42° (marked by purple lines in Fig. 4.8), related to the two most intense peaks in an FeO impurity phase. This is not uncommon when analyzing the molten tip as the temperature distribution in this part of the growth can be uneven, especially when cooling to separate the feed and seed rod. Impurity phases can occur due to cooling quickly, not allowing for crystal formation. Despite this, an initial x-ray diffraction of the molten tip provides a good indication of the phase purity of the sample, before taking Laue images and orientating the crystal for macroscopic measurements.

The diffraction pattern for the powdered molten feed from batch C was performed on the Huber Guinier G670 and is shown in figure 4.9. Due to the large intensity range, please refer to figure 4.6 for the initial batch C polycrystalline diffraction pattern. With a slight increase in oxygen, using the $CO:CO_2$=1:3.5, a larger FeO impurity phase is present. The batch B, powdered molten feed diffraction pattern presents only two of the largest FeO impurity peaks at 36°, 42.2°, whereas the crystal grown in $CO:CO_2$=1:3.5 exhibits the whole range of FeO impurity peaks, at 36°, 42.2° and 61.2°, 73.2° and

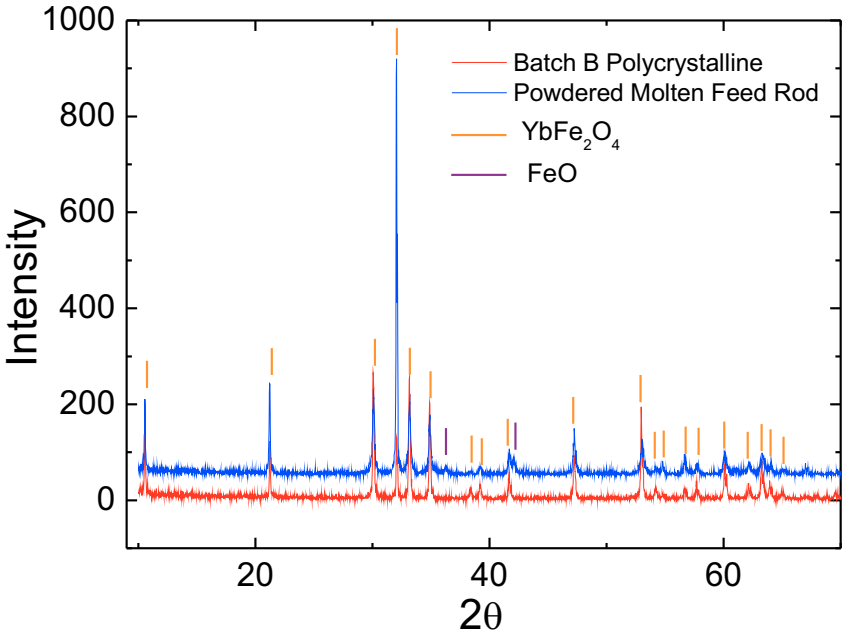

Figure 4.8: X-Ray Diffraction of batch B Polycrystalline and Powdered Crystal. Red curve: X-ray diffraction of batch B polycrystalline. Blue curve: powdered molten tip from boule grown in $CO:CO_2$=1:3. Orange and purple markers represent $YbFe_2O_4$ and FeO phases, respectively.

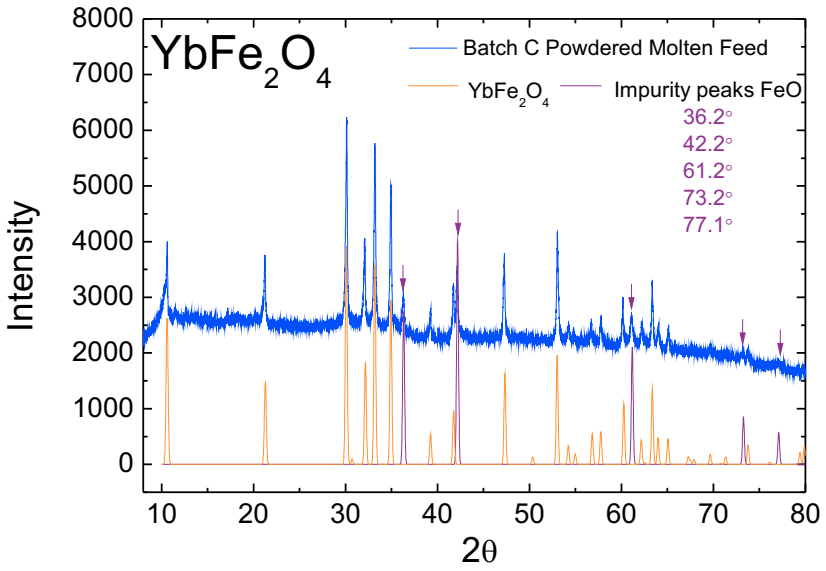

Figure 4.9: X-Ray Diffraction of batch C of Powdered Molten Feed
Blue curve: powdered molten tip from boule grown in $CO:CO_2$=1:3.5. Orange and purple diffraction patterns represent $YbFe_2O_4$ and FeO phases, respectively (data taken from ICSD database (73) (75)).

77.1°. To better analyze the initial diffraction patterns obtained for powdered crystal fragments taken from the middle section of the boules grown in the CO:CO_2=1:3 and CO:CO_2=1:3.5 gas atmospheres, powder refinements were performed. A repeat each x-ray diffraction with scans of 10 h were taken on the Huber Guinier G670, to improve the quality of the data for refinement. A refinement of the crystal grown in the CO:CO_2=1:3 atmosphere is shown in figure 4.10.

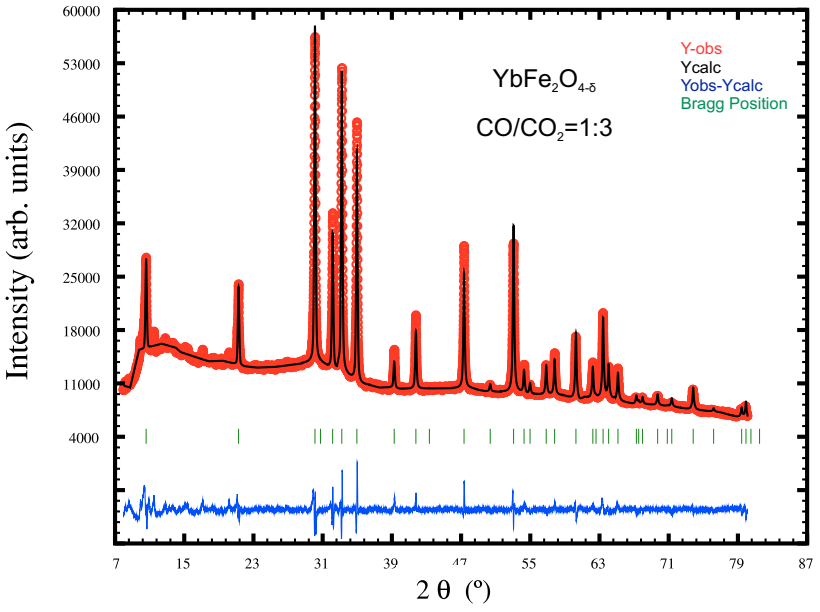

Figure 4.10: Rieveld Refinement
Powder x-ray diffraction refinement of the crystal grown in CO:CO_2=1:3.

From the refinement of the crystal boule grown in the CO:CO_2=1:3, a single phase $YbFe_2O_{4-\delta}$ profile with lattice parameters a=b=3.4511(9) Å and c=25.0566(7) Å is achieved with Bragg R Factor= 3.39 and χ^2=12.4. These values are slightly higher than the values aimed for when refining a structure, however they depend on the quality of the diffraction data and the length of the scan. There is a large background contribution from the sample holder between 9 and 20°, which can be smoothed with the use of *Winploter*, but will still effect final values of the diffraction data and theoretical fit.

A refinement of powdered crystal fragments taken from the centre of the boule

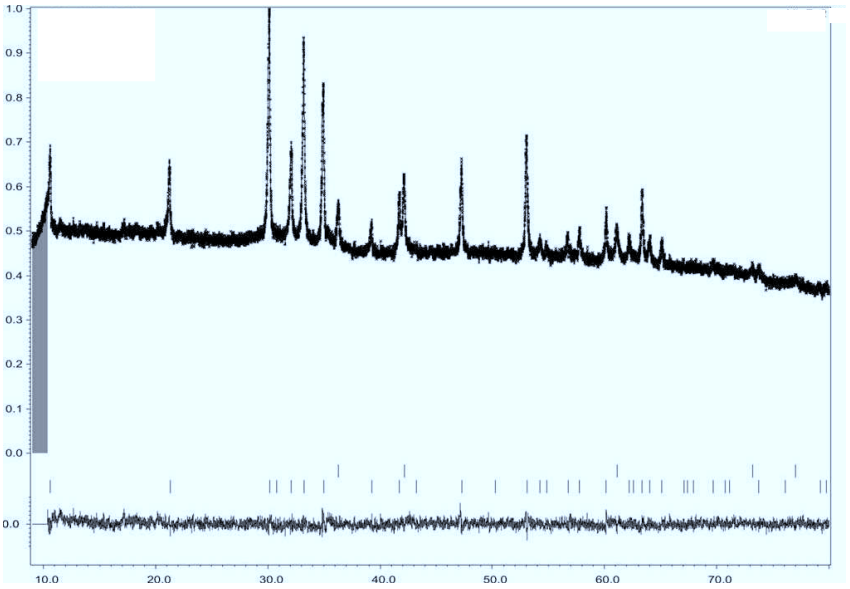

Figure 4.11: Jana Refinement
Powder x-ray diffraction refinement of the crystal grown in CO:CO_2=1:3.5. Red pattern: Observed data, black pattern: calculated pattern, green line: Bragg peak positions and blue line: Calculated data subtracted form observed data.

grown in CO:CO_2=1:3.5, is shown in figure 4.11. The x-ray data could not be refined as single phase $YbFe_2O_{4-\delta}$ but exhibited a complete FeO impurity phase. There are two sets of Bragg reflections shown in figure 4.11, the top line of Bragg positions represent the FeO peaks and the second line of Bragg positions are representative of the main $YbFe_2O_{4-\delta}$ phase. The lattice parameters obtained for $YbFe_2O_4$ are a=b=3.4523(2) Å,c=25.1228(7) Å and FeO a=b=c=4.2896(4) Å, where the lattice constants for $YbFe_2O_4$ are in good agreement with the refinement of the crystal grown in CO:CO_2=1:3 showing only a small discrepancy of 0.005 Å. The presence of the FeO phase is at first surprising as an excess of oxygen would result in a magnetite phase of Fe_2O_3 based on the phase diagram produced by Kimizuka *et al.* (44). However, the FeO phase is only present in the CO:CO_2=1:3.5 diffraction pattern, which contains only 0.5 more oxygen than the CO:CO_2=1:3. Therefore only a small phase breakdown will occur. The absence of any YbO or Yb_2O_3 within the diffraction pattern may be a result of the melting temperature of Yb in comparison to that of Fe. Fe has a much higher melting point of 1811 K compared to that of Yb which melts at 1097 K. Therefore the evaporation of excess Yb during growth is likely. The crystal grown in CO:CO_2=1:5

(see Fig 4.7) exhibits a complete phase breakdown, where the excess oxygen breaks down the initial polycrystalline single phase $YbFe_2O_4$ to a number of oxidizing phases to support the increase of oxygen atoms.

4.2.3 Magnetization

The magnetization of both $YbFe_2O_{4-\delta}$ single crystals grown in CO:CO_2=1:3 (1:3) and CO:CO_2=1:3.5 (1:3.5) were measured on the CCMS, using a VSM option, described earlier in section (2.4.2). The magnetization of the samples were measured in a temperature range of 10-300 K for ZFC, FC and FW (Field Warming) measurements, with an externally applied magnetic field of 100 Oe. The magnetization for both crystal stoichiometries was measured with the magnetic field applied parallel to the c axis only, based on the previous finding mentioned in chapter 1.

Magnetization data for the (1:3)a and (1:3.5)b crystals, respectively, is shown in figure 4.12. The magnetization data from (1:3) has three main, distinct features: a main Néel transition with a peak at 248 K on warming, a small peak on cooling at 219 K, and finally a large drop below 145 K on further cooling. The transitions are directly comparable to the magnetization data from (1:3.5) gas atmosphere. The features are slightly more smeared out, but within 1-2 K of the transition temperatures observed in the CO:CO_2=1:3 magnetization data. The largest transition at 142 K has a lower magnetic moment of $\sim 0.30 \mu_B$/f.u. Interestingly the ZFC line (noted with the 1 next to the arrow) has a higher overall magnetization on warming than that of the (1:3), despite having a lower overall field-cooled magnetization.

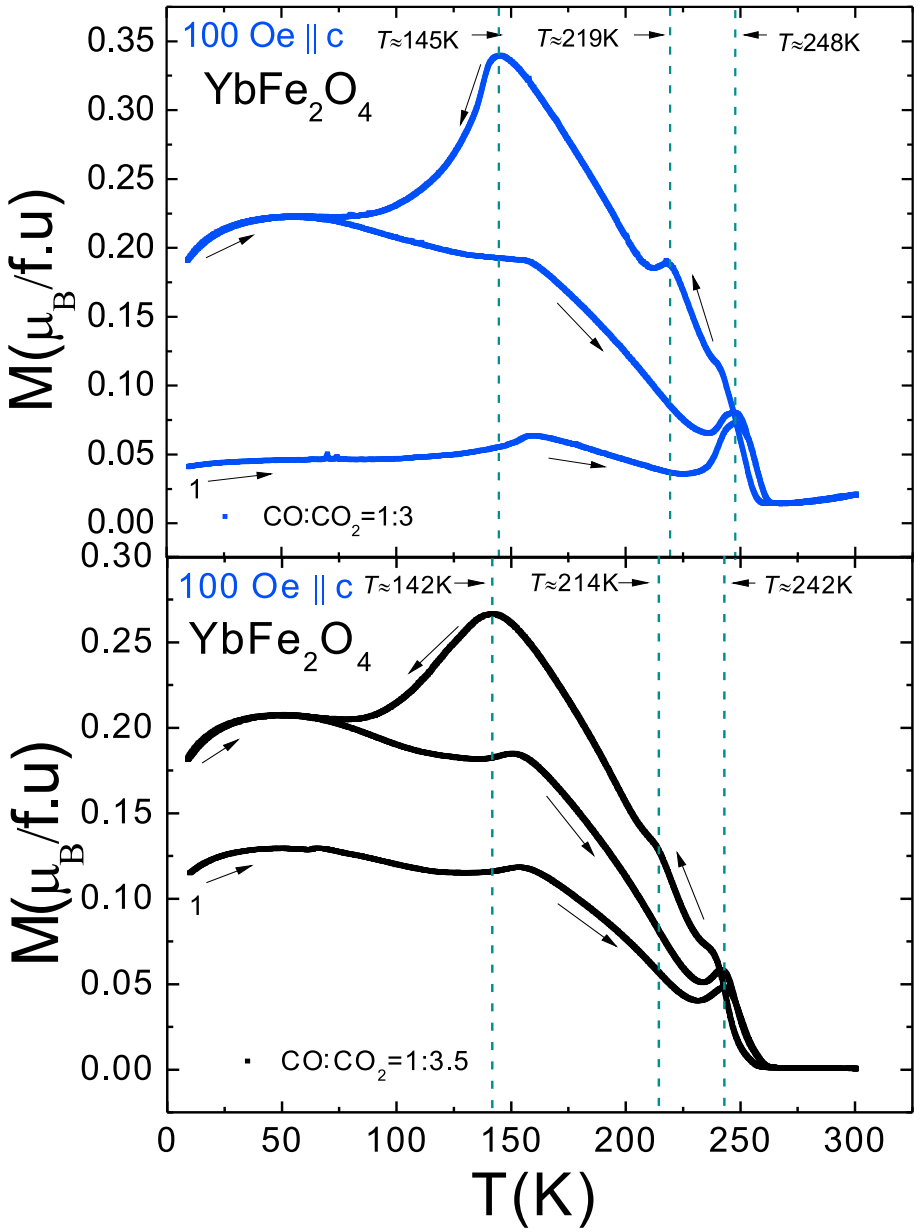

Figure 4.12: Magnetization Data
(a) ZFC, FC and FW data from single crystal grown in CO:CO_2=1:3. (b) ZFC, FC and FW data from single crystal grown in CO:CO_2=1:3.5.

4.2.3.1 Thermo-remanent Magnetization

In order to measure the thermo-remanence of $YbFe_2O_{4-\delta}$ and gain an initial insight into any spin glass behavior a thermo-remanent magnetization measurement was performed. The (1:3.5) sample used in the previous magnetization measurement was used for this measurement (refer to Fig. 4.12) . With the crystal mounted such that the crystallographic c axis is parallel to H, a large field of 5 T was applied to the sample at room temperature, and cooled at a rate of 2 K/min down to 10 K. At 10 K the magnetic field is reduced to 0 T and the sample is heated at 2 K/min back to room temperature.

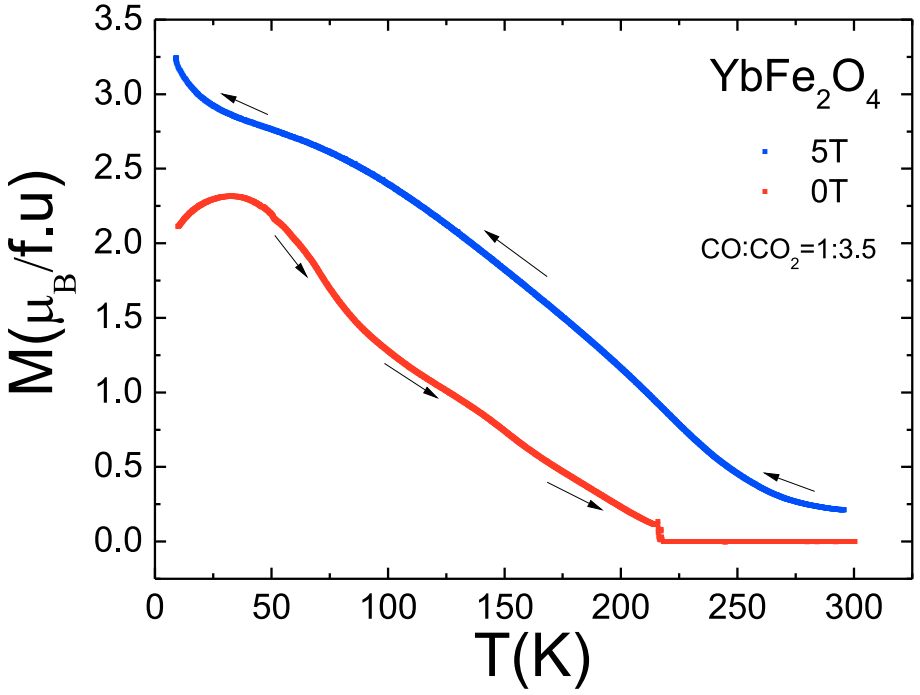

Figure 4.13: Thermo-Remanent Magnetization Measurement
Blue curve: cooling down to 10 K in an externally applied field of 5 T. Red curve: warming in zero field to room temperature.

The thermo-remanent and FC data is shown in figure 4.13. The magnetization on field cooling in 5 T exhibits a slow increase in the magnetization from 300-250 K followed by a constant increase in magnetization to approximately 90 K. From 90 K there is a broad maximum before the magnetization increases steeply from 30 to 10 K with a maximum magnetization of $\sim 3.25 \mu_B$ at 10 K. On reducing the magnetic field

to zero and warming to room temperature, there are more distinct features present. A broad maximum is now present at 30 K with a magnetization of $\sim 2.30 \mu_B$. On warming further to 90 K the magnetization decreases steeply. Beyond 90 K the curve levels out becoming more linear, with a small bump at 145 K. The magnetization continues to decrease with a sudden double peak at 215 K, which can be seen more clearly in figure 4.14. Beyond this point the magnetization drops to zero at 218 K.

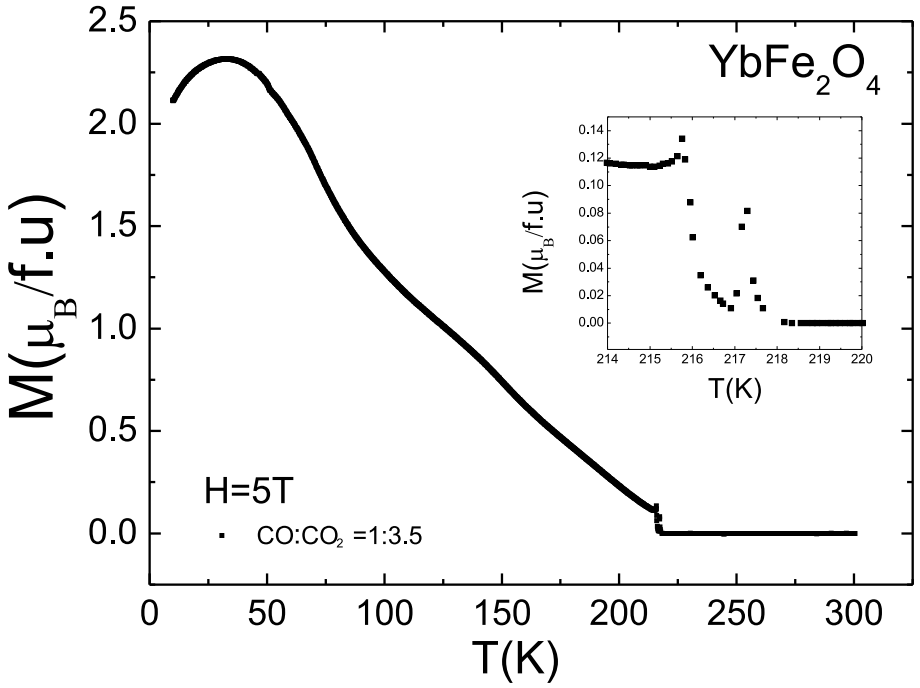

Figure 4.14: Thermo-Remanent Magnetization Heating Curve Measurement
Black curve: thermo-remanent magnetization on heating. Inset: zoomed in view of double peak transition at 218 K.

4.2.4 Specific Heat

The specific heat measurements performed on $YbFe_2O_{4-\delta}$ on both the (1:3) (blue curve) and (1:3.5) (black curve) crystals were done in the same way as the previously measured $LuFe_2O_{4-\delta}$, described in chapter 2. The temperature range covered for the specific heat of each crystal, ranged from 150 to 325 K. There is a large notable difference between the features present in the (1:3) crystal compared to that of the (1:3.5) crystal. Based on a time constraint when performing the specific heat measurement on the (1:3) crystal, not enough addenda points were taken of the empty puck measurement. Therefore the bumps in the curve ranging from 180 K to ∼290 K are an effect resulting from poor puck subtraction. This is clear when comparing this data to the data obtained from the (1:3.5) crystal, where the temperature increments measured on the empty puck and sample were kept consistent. Both specific heat curves show a relatively sharp peak at ∼304 K where the overall specific heat of the (1:3) crystal is higher than that of the (1:3.5) crystal, indicating that a transition to CO might take place.

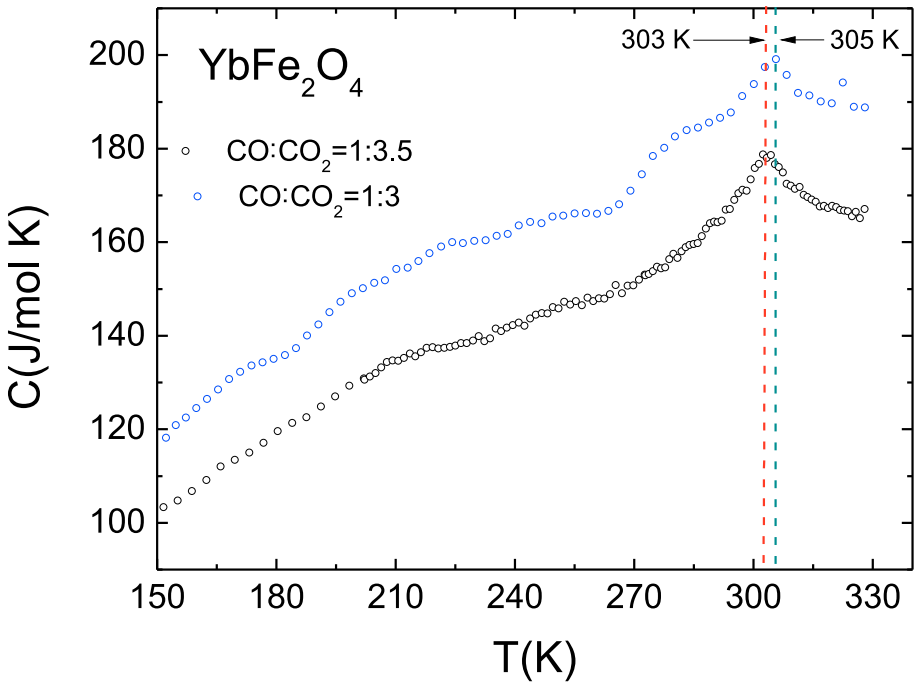

Figure 4.15: Specific Heat Data
Blue curve: specific heat data of the (1:3) crystal. Black curve: specific heat data of the (1:3.5) crystal.

4.2.5 Single Crystal X-ray Diffraction

Single-crystal x-ray diffraction was performed on a small crystal (μ range) grown in the $CO:CO_2$=1:3 gas atmosphere. The crystal is mounted and measured in the same way as that described in section (3.4.3). The data shown in figure 4.16, represents reciprocal maps taken along the hhl and hh0 direction at 90 (top) 230, RT and 350 K.

The CO present in the hhl plane (based on previous findings described in chapter 1) the CO is more distinct at 90 K well below the CO transition, which based on the specific heat data in section (4.4) occurs at $\sim$ 305 K. On warming to 230 K the CO along the (2/3, 2/3, l) line become more diffuse and weak. At 350 K only diffuse lines are present as in $LuFe_2O_4$ (1:3) crystal, where all peak strength which is seen at 90 K is no longer present. Notably, there is some alteration with the shape and size of the Bragg peaks, positioned at the (006) and (0015), when measured at lower temperatures. This may be representative of a structural transition where the rhombohedral unit cell describing the structure at RT may not fit the data at lower temperatures (similar to the $LuFe_2O_4$ structure), or it could be an artifact of the experiment itself due to insufficient sampling between 2 subsequent angles in a scan.

Despite seeing strong diffuse lines at 90 K, there is no indication of long range charge order, which is seen clearly in $LuFe_2O_4$ crystals grown in $CO:CO_2$=1:3. Moreover there is strong evidence from the specific heat data, with the presence of a sharp peak around 305 K, indicating the onset of CO from the $YbFe_2O_4$ (1:3) crystal, which is not clearly supported with the single crystal x-ray diffraction data. The crystal selected for the single crystal x-ray diffraction was a different crystal to the one used to measure the magnetization and specific heat, based on the small size of crystal required. The selected crystal from the boule grown in $CO:CO_2$=1:3 may not be of the same quality to that of those selected for the macroscopic measurements, due to variations in the oxygen stoichiometry of $YbFe_2O_4$, and therefore not portraying the true nature of the CO in this system. A refinement of the single crystal x-ray data at RT and 90 K and subsequent x-ray scans on different crystals are necessary to find the best stoichiometric crystal and possible 3D CO.

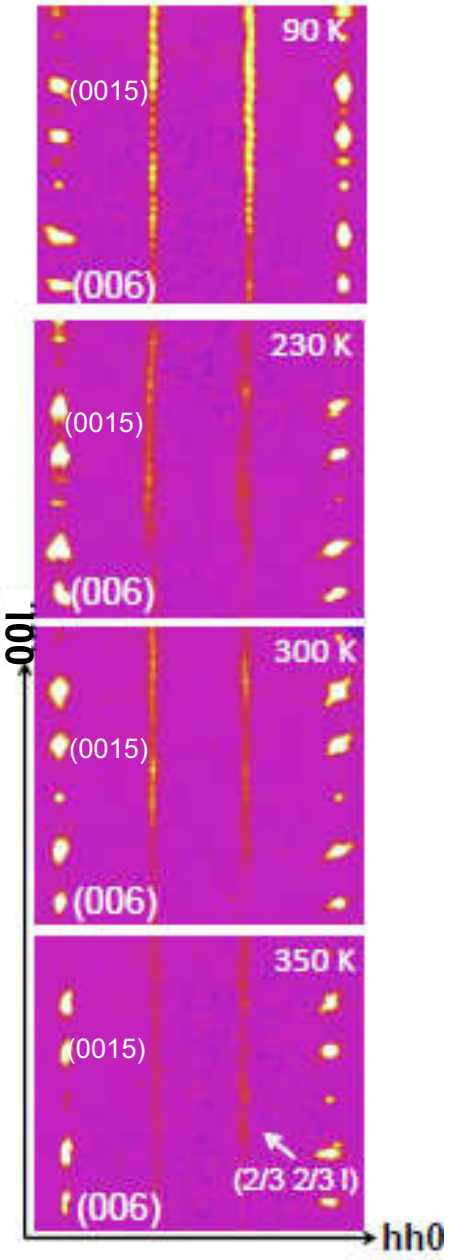

Figure 4.16: Single Crystal x-Ray Diffraction
Single crystal x-ray diffraction data of crystal grown in CO:CO_2=1:3 measured at four temperature increments.

4.2.6 A.c Susceptibility

In order to look for spin glass properties in $YbFe_2O_{4-\delta}$, an a.c susceptibility measurement of a crystal grown in the $CO:CO_2$=1:3.5 gas atmosphere was performed. As described in detail in section (2.6), both the real, $\chi\prime$, and imaginary, $\chi\prime\prime$, parts are recorded on cooling and heating, between 260 and 60 K with applied frequencies of 13, 110, 1010, 5020 and 9010 Hz.

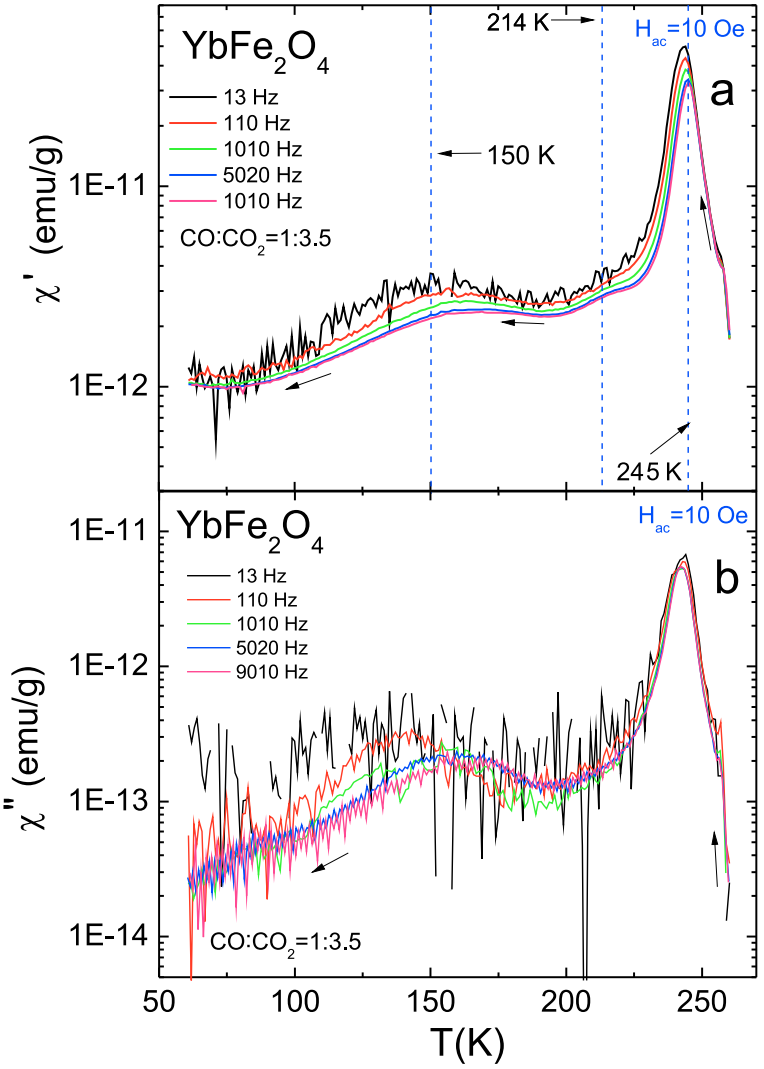

Figure 4.17: A.c Susceptibility of Crystal Grown in $CO:CO_2$=1:3.5 (Cooling) (a) Real part of a.c susceptibility. (b) Imaginary part of a.c susceptibility.

The data shown in figure 4.17a exhibits four main transitions present in the real data, $\chi\prime$, and correspond well to the magnetization data described in section (4.4), at the main Néel transition ∼240 K as well as 214 K and 150 K, where a small sharp peak, at ∼250 K is seen in the d.c magnetization data as a significant rise in magnetization upon cooling. The imaginary part on cooling shows a frequency dependence at the sharp peak present at 250 K, but no frequency separation at 240 K, see figure 4.17b. On cooling further there is a small frequency dependence at 214 K, with a large increase in the frequency dependence at 150 K and below. Another artifact, present only in the imaginary part of the a.c susceptibility is the shifting of a transition peak to a lower temperature for decreasing frequencies, which is consistent with 'glassy freezing'.

The a.c susceptibility with both real and imaginary parts on warming is shown in figure 4.18. The real part on warming is very similar to that on cooling. The imaginary part however, exhibits a larger frequency dependence at the 250 K transition compared to that of the cooling data as well as the frequency dependence to the main Néel transition. As with the data on cooling, there is a small frequency dependence at 218 K which increases below 150 K. Based on the sensitivity of the a.c susceptibility option with the PPMS, the low frequency at 13 Hz is extremely noisy compared to the higher vibrating frequencies applied. A careful analysis of the peak temperature shift present in the imaginary part of the a.c susceptibility would show if it was a spin glass or a cluster glass magnetic state, below T_N.

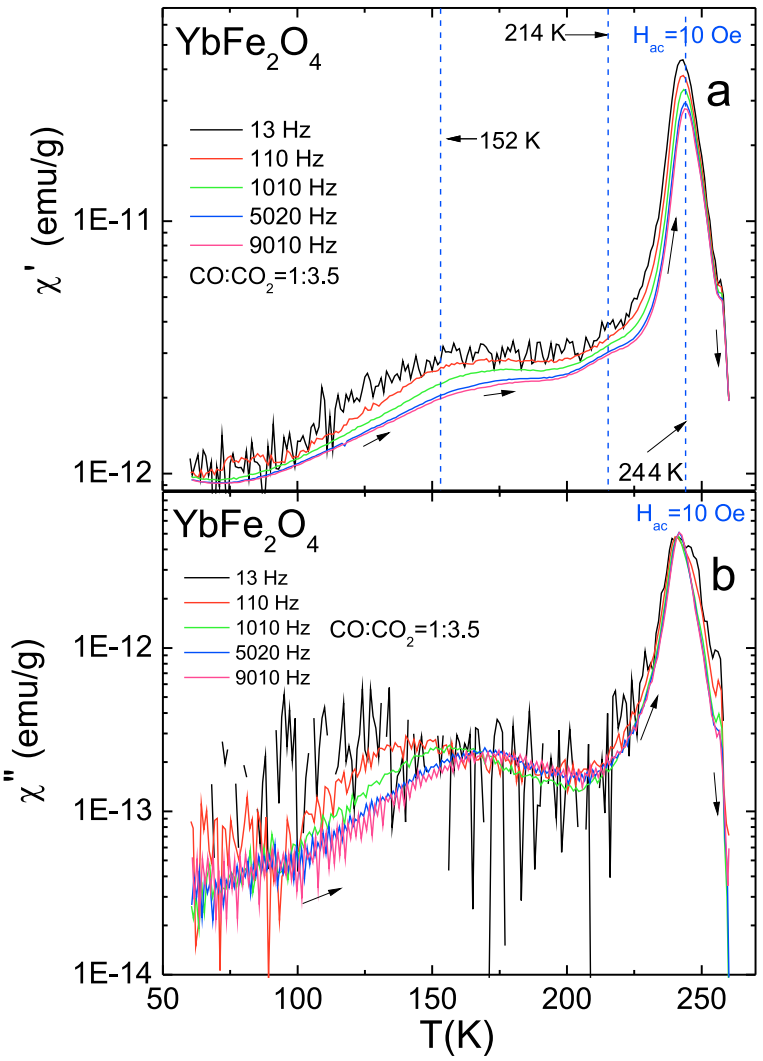

Figure 4.18: A.c Susceptibility of Crystal Grown in $CO:CO_2$=1:3.5 (Warming) (a) Real part of a.c susceptibility. (b) Imaginary part of a.c susceptibility.

4.2.7 Mössbauer Spectroscopy

Mössbauer spectroscopy of powdered single crystals grown in the $CO:CO_2$=1:3 gas atmosphere is reported in figure 4.19. The Mössbauer spectra was recorded on a constant acceleration spectrometer with a Rh matrix ^{57}Co source. Five temperatures at 310, 250, 230, 200 and 150 K were recorded on the Mössbauer spectra, which are above and below the transition temperatures present in the magnetization data. The data shows a single peak at 310 K where, on cooling to 250 K a peak splitting starts to emerge, indicative of Fe^{2+} and Fe^{3+} valence splitting. On further cooling to 230 K, there is an emergence of two peaks either side of the central peak, which on cooling to 150 K arranges into six peaks. At 150 K the total of six peaks, correspond to possible electric quadrupole and magnetic dipole interactions. No fit has currently been made to the spectrum to determine the nature of the magnetic order present.

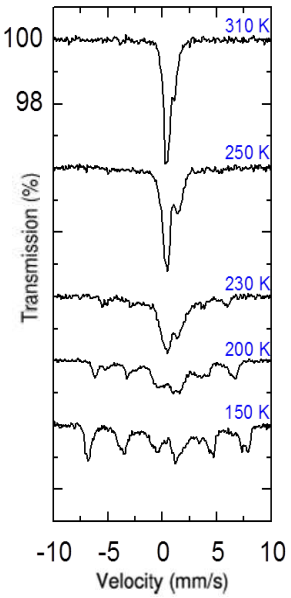

Figure 4.19: Mössbauer Spectroscopy of $YbFe_2O_4$ Powdered Single Crystal
Mössbauer spectra taken at five temperatures on cooling of powdered single crystal grown in $CO:CO_2$=1:3.

4.2.8 Neutron Scattering

The following subsections will provide the experimental details and results obtained from our measurement time at the (DNS) Diffuse Neutron Scattering at the FRM-II on a $YbFe_2O_4$ single crystal of mass 60 mg, grown in $CO:CO_2$=1:3.5 and oriented along the c axis. The (1:3) and (1:3.5) crystals previously measured, exhibiting good magnetization and specific heat curves, are two small. Based on the absence of any previous neutron studies on $YbFe_2O_4$, the count rate with respect to sample size is not yet known.

4.2.8.1 Magnetization

Previous magnetization measurements performed on both $LuFe_2O_{4-\delta}$ and $YbFe_2O_{4-\delta}$ single crystals, shown in section (3.4) and (4.4), respectively, have shown that the effects of oxygen stoichiometry can drastically alter the quality of the transitions and the type of charge and magnetic order present in each system, with sample to sample dependence often seen in one crystal growth. In order to ascertain the quality of the crystal isolated for the DNS beam time, a measurement of magnetization as a function of temperature was performed on ZFC and FC, between 10 and 300 K, with an externally applied magnetic field of 100 Oe.

The ZFC and FC curves shown in figure 4.20 (with arrows indicating the direction of cooling and heating) show the presence of the main Néel transition at 237 K. The FC curve exhibits two very broad transitions at 131 and 30 K which is smeared out on ZFC. These transition points relate to the initial magnetization measurements described in section (4.4), but are less defined and appear at slightly shifted temperatures. The red line relates to the spin flip Bragg line intensity contribution for the four scan temperatures scanned at; 255, 200, 100 and 3.65 K (base temperature).

Due to the difficulty in isolating a crystal of the same stoichiometric quality as those used during the macroscopic measurements as well as one which is large enough to be accepted for neutron beam time, the 60 mg crystal of average quality was the best option for an initial look at both the charge and magnetic order in this system.

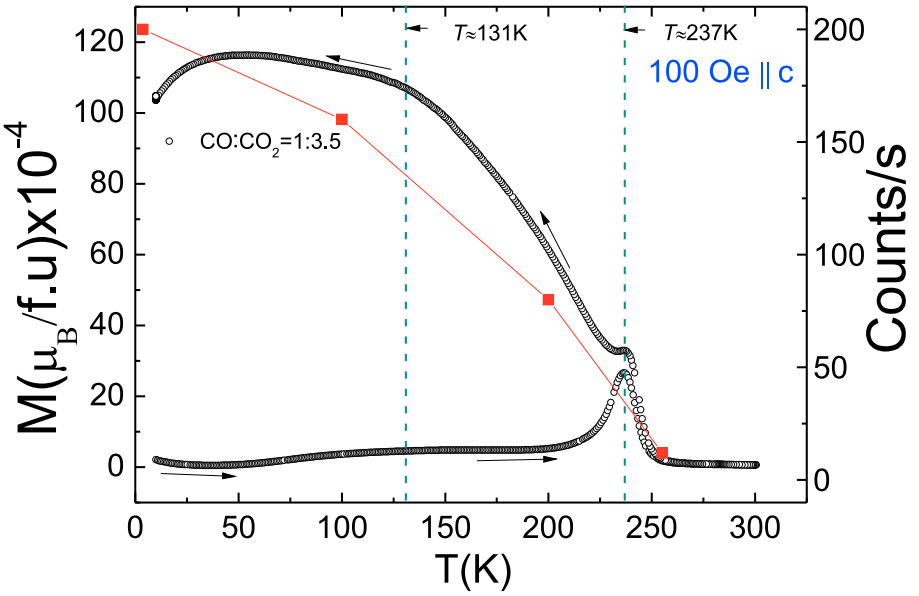

Figure 4.20: Magnetization Data for Crystal used at DNS
ZFC and FC data of crystal grown in $CO:CO_2$=1:3.5 gas ratio.

4.2.8.2 Non-Spin Flip Polarization along hhl

The non-spin flip polarization provides information of possible CO contributions within a sample. The experiment performed at DNS mapped the hhl plane at temperatures of T= 255, 200, 100 and 3.65 K (see figure 4.21). The 60 mg crystal was orientated on the sample holder such that the incoming polarized neutrons were incident on the crystal surface, and parallel to the c axis. Weak diffuse scattering is observed along (1/3, 1/3, l) and (2/3, 2/3, l) at each temperature scanned. At 255 K a maximum intensity of 25 counts/s is present along the (2/3, 2/3, l) line and on cooling to 200 K, the intensity increases to approximately 30 counts/s. A maximum intensity of 35 counts/s was observed along the (2/3, 2/3, l) diffuse Bragg lines, where the intensity increases on further cooling to 100 K and base temperature

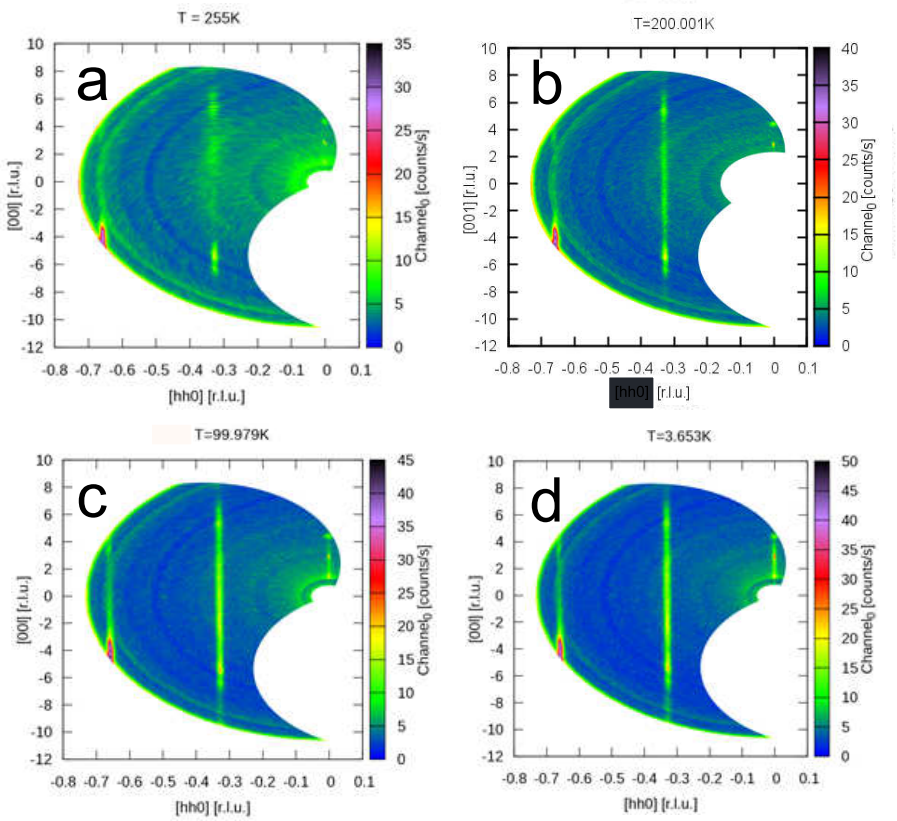

Figure 4.21: Diffuse Neutron scattering Non-Spin Flip Polarization Non-spin flip polarization along 00l at 255, 200, 100 and 3.65 K.

In order to ascertain whether the CO is a true artifact of the non-spin flip polarization or a magnetic contribution, based on the direction of the polarized neutrons to the scattering vector Q, analysis of the incoming neutrons parallel to x (roughly parallel to the average Q) (37), is essential. The data shown in figure 4.22 highlights the non-spin flip polarization of the incoming neutrons parallel to x (a), which is not perfectly aligned along c, like with the data shown in figure 4.21 where polarized neutrons are parallel to z (b), but will also contain and ab-component. The data measured at 200 K for both non-spin flip contributions with neutrons parallel to x and z, show the same CO peak along the (2/3, 2/3, l) line, indicating that it is a true structural transition and not magnetic contribution from the alignment of magnetic moments along the c axis.

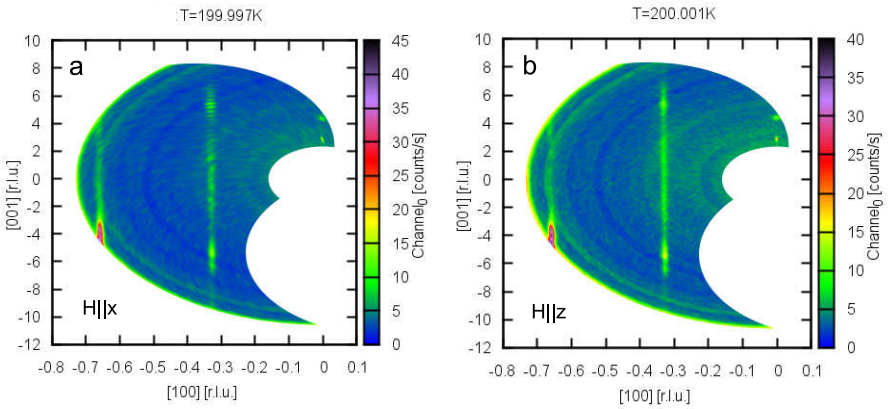

Figure 4.22: Non-Spin flip Analysis at 200 K
Non-spin flip polarization along 00l at 200 K with (a) H——x and (b) H——z.

4.2.8.3 Spin Flip Polarization along hhl

The spin flip polarization analyzes the magnetic contribution of the sample, which in this case highlights 2D diffuse magnetic scattering along the (1/3, 1/3, l) line and (2/3, 2/3, l). The spin flip polarization data was taken at T=255, 199, 100 and 3.65 K, and is shown in figure 4.23. A very weak magnetic signature with a maximum of 10 counts/s is recorded at 255 K (see figure 4.23a) before the main Néel transition at T=237 K, shown previously in the magnetization measurement. Below 255 K at ∼200 K (figure 4.23b) strong diffuse magnetic scattering is present with a maximum of ∼60 counts/s. Interestingly, on measuring at lower temperatures of 100 K (4.23c) and base temperature 3.65 K (figure 4.23d) the magnetic signature increases, which may be representative of the two broad features in the magnetization data shown in figure 4.20, at 131 K and 50 K. The absence of magnetic Bragg peaks suggests glassy 2D-order, with no long range magnetic correlations throughout the crystal.

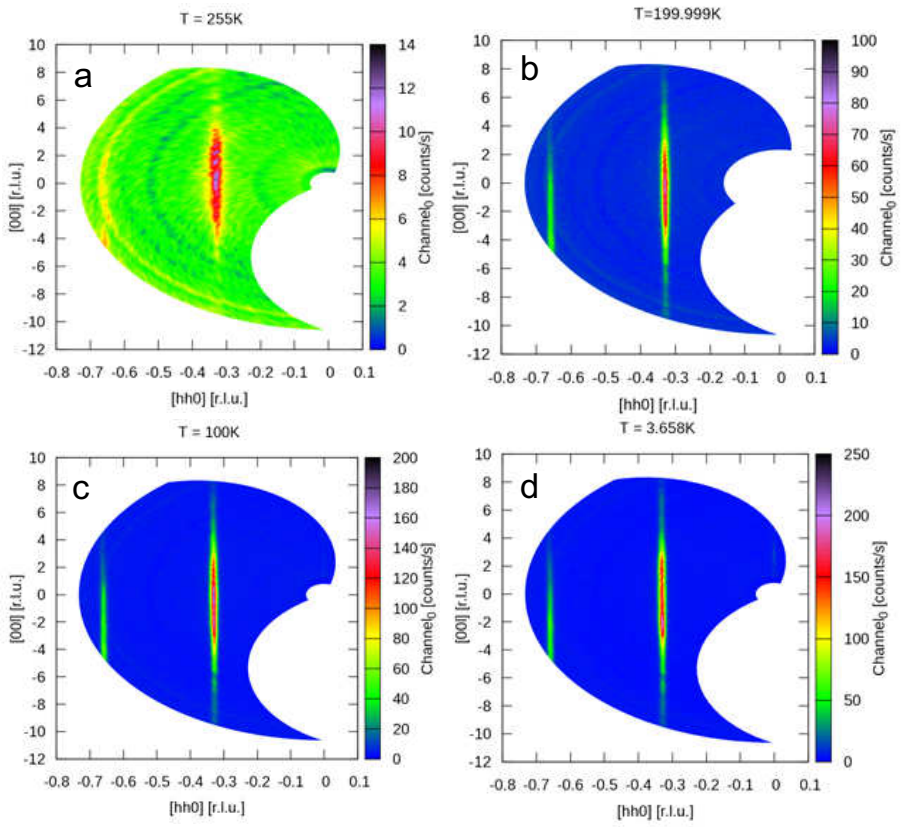

Figure 4.23: Diffuse Neutron Scattering Spin Flip Polarization
Spin flip polarization along 00l at 255, 200, 100 and 3.65 K.

4.3 Discussion

Single phase polycrystalline samples of $YbFe_2O_4$ were all synthesized using stoichiometric mixtures of Yb_2O_3 and Fe_2O_3 and heated using a $CO:CO_2$=1:3 gas ratio. It was only during the crystal growth that the gas ratio was altered. The initial crystal growth was performed using the $CO:CO_2$=1:5 gas ratio; based on the interesting magnetic and CO behavior seen in previous crystal growths of $LuFe_2O_4$ (refer to section (3.3)). Unfortunately, the same did not apply for the crystal growth of $YbFe_2O_4$ using this gas ratio, as not only was it difficult to stabilize the molten zone during growth, but the produced crystal was no longer single phase $YbFe_2O_4$. This is due to the oxygen partial pressure which is in equilibrium with the stoichiometric material is smaller for Yb than Lu. By performing powder x-ray diffraction, it was evident that the single phase $YbFe_2O_4$ had decomposed into four different phases namely: O_3, Yb_2O_3, $YbFe_2O_4$, $Yb_2Fe_3O_7$ and $Yb_3Fe_5O_{12}$. There are a number of reasons for a phase break down during crystal growth: temperature, speed of growth and more importantly the gas ratio used. The chemical composition with respect to the Fe-O octahedra coordination within $YbFe_2O_4$ and $LuFe_2O_4$ differs slightly. The average Fe-O ionic coordination of each octahedra within $YbFe_2O_4$ is 1.94 Å, which is slightly smaller than that of $LuFe_2O_4$, which has an average Fe-O ionic distance of 1.97 Å. This small difference in the ionic position provides just enough stability for Fe-O bonding in the $LuFe_2O_4$ crystal, however the slightly shorter Fe-O bond length in $YbFe_2O_4$ cannot support the excess oxygen in the more oxidizing gas ratio ($CO:CO_2$=1:5), and thus breaks down into subsequent oxidizing phases.

It was this discovery that led to the use of a lower oxygen partial pressure, therefore we maintained the use of the $CO:CO_2$=1:3 gas ratio, which was used for the initial synthesis of single phase polycrystalline $YbFe_2O_4$.

The magnetization data shown in figure 4.24a highlights the presence of three distinct transitions at 248, 219 and 145 K, followed by a small broad hump around 30 K. The transition at 248 K indicates the onset of ferrimagnetic order (48), and the transition at 145 K is comparable to the low temperature transition seen in the $LuFe_2O_4$ magnetization data, measured at higher fields in (32). However based on previous publications containing magnetization data, there is almost no correspondence to the

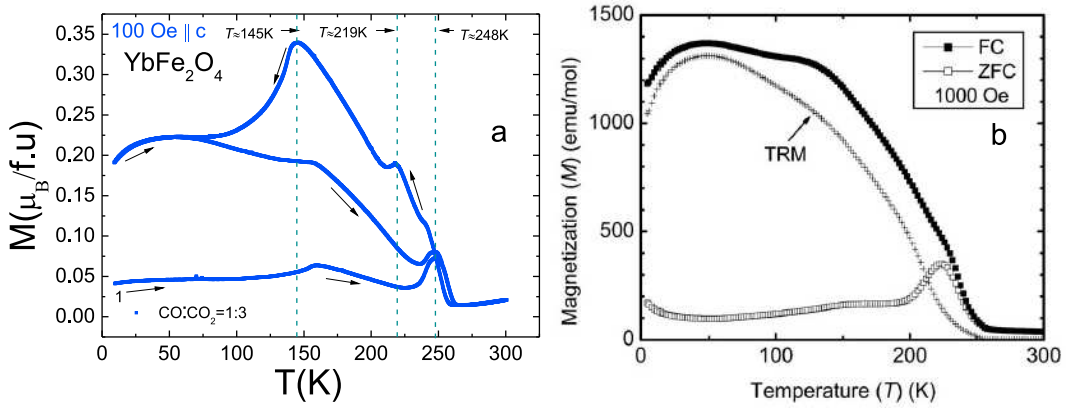

Figure 4.24: Magentization Comparison of a $YbFe_2O_4$ Grown in $CO:CO_2$=1:3 (a) ZFC-FW-FC (indicated by arrows) magnetization with an applied field of 100 Oe. (b) ZFC and FC magnetization data measured with an applied field of 1000 Oe, TRM curve marked with crosses. (b) was reproduced from Ref (48).

transition located at 219 K. Magnetization on ZFC and FC with an applied magnetic field of 1000 Oe, performed by Yoshii *et al.*, provides the closest correlation to the lower temperature transitions at 145 and 30 K, shown in figure 4.24b. Despite their sample being polycrystalline, there are indications of the three main transitions, which appear in our single crystal measurements, with the only exception being the transition at 219 K. All the transitions are more smeared out due to random orientation of the many small crystals present, in the polycrystalline sample. Based on the rhombohedral structure the spin direction of the magnetic moments align along *c*, and is susceptible to saturation of the magnetization at fields much above 100 Oe, where their application of 1000 Oe will also produce some smearing of the transitions; reducing the sharpness. This was seen clearly during previous investigations on $LuFe_2O_4$ in fields from 1000 Oe (68). Yoshii *et al.*, define the transition at 130 K, which would correspond to the 145 K transition in our data, to a modulation of the magnetic structure or a possible spin fluctuation in the Fe sublattice. Further speculation aims at the occurrence of a magnetic structural change, based on previous magnetization studies on YFe_2O_4 (76).

In order to further investigate the magnetism and also any CO present in the system, a specific heat measurement was performed. There are no current publications which provide specific heat data on $YbFe_2O_4$, due to the difficulty of synthesis and more

importantly stoichiometric quality. Therefore to establish a basis for comparison, the specific heat data is compared to the specific heat measurements performed on the better stoichiometric $LuFe_2O_4$, shown in section (3.4.1). The specific heat data shown figure 4.25a shows only one transition near 305 K in both curves of $YbFe_2O_4$ grown in $CO:CO_2$=1:3 and $CO:CO_2$=1:3.5, indicative of CO and corresponds well with the data shown in figure 4.25b

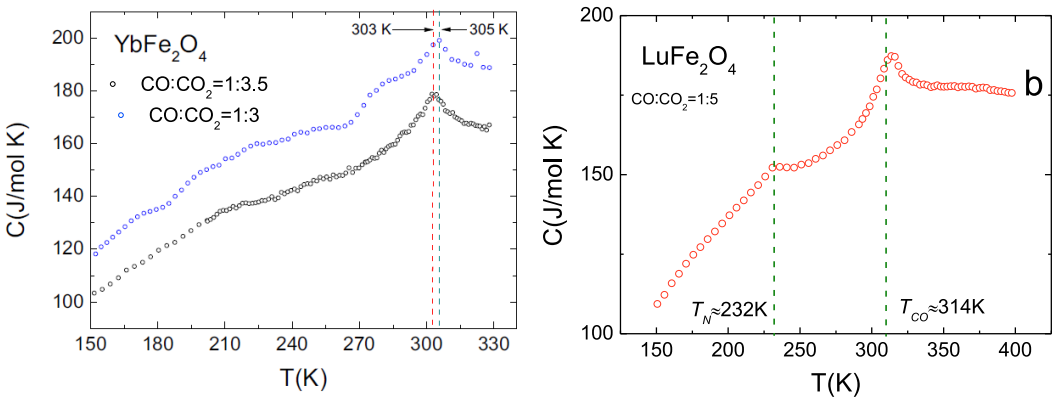

Figure 4.25: $YbFe_2O_4$ and $LuFe_2O_4$ Specific Heat Comparison
(a) specific heat of $YbFe_2O_4$ for both (1:3) (blue curve) and (1:3.5) (black curve) crystals. (b) Specific heat of $LuFe_2O_4$ (1:5) crystal.

The specific heat data of $YbFe_2O_4$ (blue curve) grown in $CO:CO_2$=1:3 exhibits the same sharp CO transition seen at T_{CO}=314 K in the $LuFe_2O_4$ crystal grown in $CO:CO_2$=1:5, but at a slightly lower temperature of T=305 K. The small bumps in the data, below 300 K, are not representative of any magnetic transition, as the specific heat data taken from the crystal grown in $CO:CO_2$=1:3.5 has no such features but stems from insufficient points taken for the empty puck subtraction, described earlier in section (2.5). The absence of a peak indicating ferrimagnetic order in the $YbFe_2O_4$ specific heat data, may imply that initial reports stating a clear ferrimagnetic order at this transition may only apply within certain off-stoichiometric samples (46).

Single crystal x-ray diffraction of the small $YbFe_2O_4$ single crystal, grown in $CO:CO_2$=1:3, indicates the onset of CO below 350 K along the (1/3, 1/3 l) line, which corresponds well to data recently obtained at the DIAMOND synchrotron source by Hearmon *et al.* (50). The single crystal x-ray diffraction measured around 350 K from the crystal

grown in CO:CO_2=1:3 and the crystal measured by Hearmon *et al.* both show weak diffuse CO lines, shown in figure 4.26.

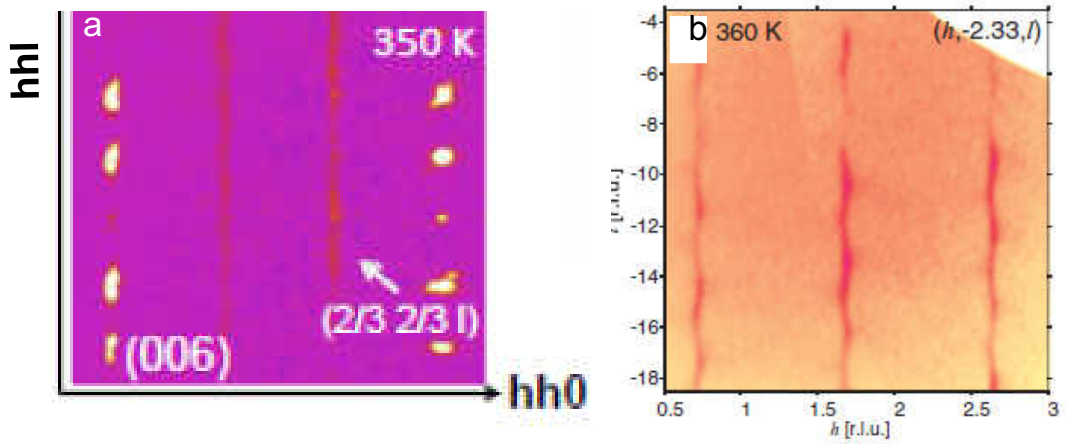

Figure 4.26: Single Crystal X-ray Diffraction Comparison at 350 K
(a) Single crystal x-ray diffraction of $YbFe_2O_4$, (b) synchrotron x-ray diffraction of $YbFe_2O_4$. (b) was reproduced from Ref (50).

Hearmon *et al.* also produced further data on cooling below 200 K, where the CO modulations become much stronger along the (h, -2.33, l) line at 150 K and compares well to our data taken at 90 K, shown in figure 4.27a-b. After much analysis by Hearmon *et al.* on the nature of the diffuse lines, through high resolution synchrotron experiments and theoretical simulation, they found a model which implies a continuous variation of charge on the Fe ions (between the Fe^{2+} and Fe^{3+}) which they state, clearly demonstrates the presence of an incommensurate CDW at 150 K. However, the CO:CO_2=1:4 crystal growth atmosphere they used which is close to the 1:5 gas ratio we initially implemented and caused a complete phase break down, provides some uncertainty to their claims of a 2D-CDW. This fact, as well as a complete absence of magnetization data shown in their recent publication, leads to the fair assumption that the origin of the CO may not be due to charge density waves, but rather off-stoichiometry. Where fine tuning the oxygen content may provide the correct oxygen environment for 3D CO peaks to arise.

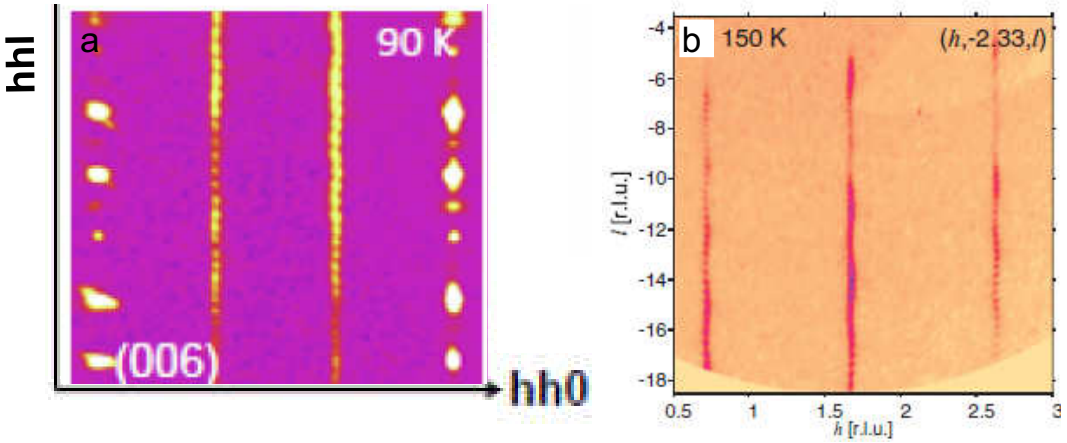

Figure 4.27: Single Crystal X-ray Diffraction Comparison below 150 K
a) Single crystal x-ray diffraction of $YbFe_2O_4$, (b) synchrotron x-ray diffraction of $YbFe_2O_4$. (b) was reproduced from Ref (50).

To further support the CO process in this system, Mössbauer spectroscopy was performed on $YbFe_2O_4$ powdered single crystal grown in $CO:CO_2$=1:3, shown in figure 4.29b. Previous studies on Mössbauer spectra performed at 77 K and 4.2 K by Tanaka *et al.* (46), are in good agreement with our current $YbFe_2O_4$ Mössbauer results. The spectra taken at 4.2 K of single crystal $YbFe_2O_4$, shown in figure 4.28, shows a lower peak intensity at ∼4 mm, compared to that of our powdered $YbFe_2O_4$ spectra, shown in figure 4.29. This difference in the single crystal and powder data can be attributed to the spin direction parallel to the *c*-axis, which can be obtained with correct alignment of the single crystal. The data taken from the powdered single crystal grown in the $CO:CO_2$=1:3, shows a direct correlation between the peak shape, position and hyperfine splitting of that seen by Tanaka *et al.*.

A recent Mössbauer spectroscopy measurement performed on a $LuFe_2O_4$ powdered single crystal of good stoichiometric quality, (Figure 4.29b) by Xu *et al.*, also provides a good basis of comparison to our data obtained for $YbFe_2O_4$ (77). On cooling below 340 K, the $LuFe_2O_4$ data exhibits one central peak, which relates to the isomer shift. A splitting in the spectra begins to emerge at 320 K indicating quadrupole splitting, where the same splitting is seen at 250 K in the $YbFe_2O_4$ data. This peak shape relates to the valence splitting of Fe^{2+} and Fe^{3+}, where Xu *et al.* were able to fit their data using a Blume-Tjon model (78) for the Fe^{2+} and Fe^{3+} relaxation. They found

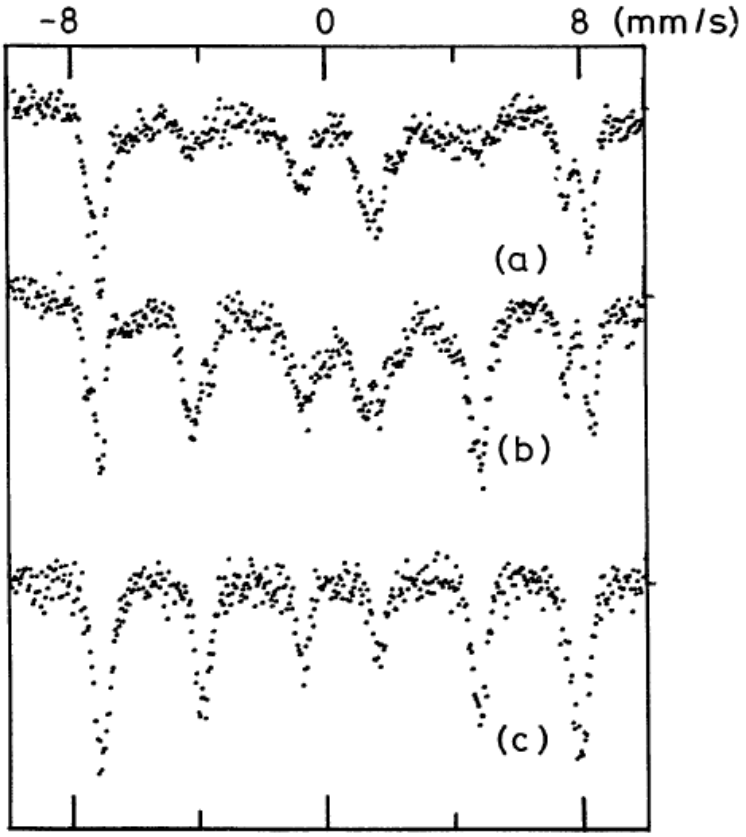

Figure 4.28: Mössbauer Spectra of ^{57}Fe in RFe$_2$O$_4$ and RFeMO$_4$
(a) YbFe$_2$O$_4$ single crystal, incident γ ray is parallel to the c-axis, (b) YbFe$_2$O$_4$ powder and (c) LuFeCoO$_4$ powder. Reproduced from Ref (46).

that individual fits of the spectra revealed two Arrhenius processes, which is clearly indicated by the temperature dependence of the hopping frequency of electrons, with a best fit constraint of 33 %. No fits were made to the $YbFe_2O_4$ Mössbauer data, however based on the structure of this system, the data analyzed in figure 4.29a for the $LuFe_2O_4$ system, provides an initial insight into the valance splitting within $YbFe_2O_4$. No temperatures were measured below the magnetic ordering temperature of $LuFe_2O_4$, but hyperfine splitting is seen at 150 K in the $YbFe_2O_4$ data.

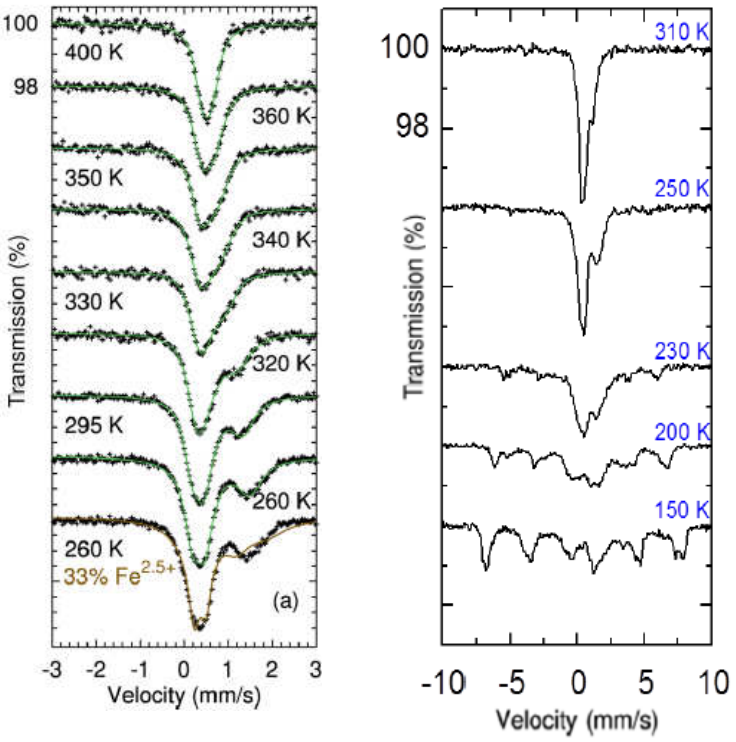

Figure 4.29: $LuFe_2O_4$ and $YbFe_2O_4$ Mössbauer data
(a) Mössbauer spectra of $LuFe_2O_4$ and alternative best fit, with a constraint of 33% of hopping electrons, (b) Mössbauer spectra performed on powdered single crystal of $YbFe_2O_4$ grown in $CO:CO_2$=1:3. (a) was reproduced from Ref (77).

To investigate the changes in stoichiometry which occur in $YbFe_2O_4$, a third crystal was grown in a slightly more oxidizing gas ratio of $CO:CO_2$=1:3.5. Powder x-ray diffraction of a selection of crushed crystals from the molten tip end of the boule uncovered the presence of an FeO phase through Jana refinement, which was not present in the data from the crystal grown in $CO:CO_2$=1:3. Further indication of other magnetic phases was tested with the use of a permanent magnet to see if there was any attraction to the magnet. The increase of the oxygen partial pressure mixture by 0.5 caused a small phase break down, exhibiting an FeO impurity, but no existence of any composite Yb^{3+} phases. This can be explained based on the melting point of Yb, which is 1097 K compared to that of Fe which is 1811 K and the partial pressure at the temperature of growth for this compound.

Magnetization measurements performed under the same condition as all previous measurements, provide a curve which is almost identical to that of the crystal grown in the $CO:CO_2$=1:3 (refer to section (4.4)). There is a slight difference in the sharpness of the transitions present, with a temperature shift of approximately 3-5 K for each transition. To better understand the magnetic behavior at these transitions, a thermo-remanent magnetization measurement was performed and provides an initial insight into any spin glass behavior. The thermo-remanent magnetization data shown in section (4.4.1) contains both cooling, which was measured with an applied field of 5 T from 300 K down to 10 K, and warming, where the field was removed and the magnetization was measured from 10-300 K. The curve on warming exhibits a high magnetization at 30 K, which corresponds to the broad hump in the magnetization data. The magnetization decreases on increasing temperature, showing two more interesting features; a broad hump around 140 K and a double peak at 218 K. These three features seen on the thermo-remanent curve, show that the electron spins on cooling in a high field retain a memory of position, and on warming remain in this coordination, which is a clear indication of a glassy state. The magnetization on warming drops to zero as it approaches the ferrimagnetic ordering temperature. To further investigate the spin glass features present in the thermo-remanent magnetization, a.c susceptibility was performed and shown in figure 4.30a. Recent investigations into the possibility of a magnetoelectric multiglass state in polycrystalline samples of $YbFe_2O_4$ by Sun *et al.* (79), provide similar data to that obtained for $YbFe_2O_4$ grown in $CO:CO_2$=1:3.5, see

figure 4.30.

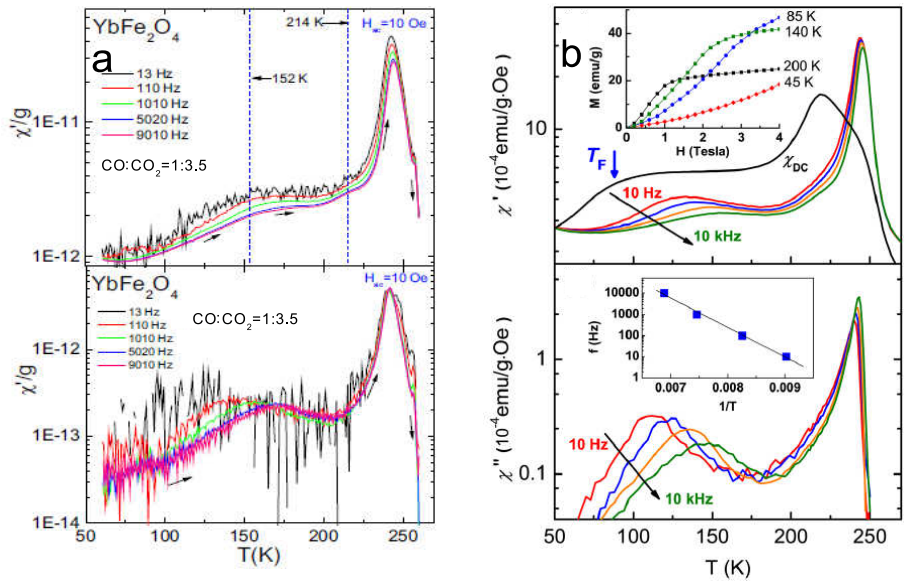

Figure 4.30: A.c Susceptibility Comparison for $YbFe_2O_4$
(a) A.c susceptibility of $YbFe_2O_4$ grown in $CO:CO_2$=1:3.5, (b) a.c susceptibility of polycrystalline $YbFe_2O_4$. Both measurements were performed on warming at at five different applied frequencies. (b) was reproduced from Ref (79).

The synthesis of polycrystalline $YbFe_2O_4$ by Sun *et al.* was completed without the use of an oxygen partial pressure environment, but heated in an evacuated quartz tube at 1100°C for 48 H. The black curve in their data, representing d.c susceptibility, is shown in figure 4.30. The curve does not exhibit the same sharp transitions seen in the lower temperature transitions present in our data, but also a complete absence of the small peak at 218 K present in our magnetization data. However the frequency dependence correlates well with our a.c susceptibility measurements, showing an onset of frequency dependence at 150 K. The one contrast between the two sets of data, is the small sharp peak just before 250 K present in our data and exhibits a distinct frequency dependence. An explanation for this small feature may stem from a similar transition to that discovered in $LuFe_2O_4$, the magnetostructural transition, which may not originate at the freezing temperature, T_f=80 K, but exist also at 250 K, based on off-stoichiometry. As the magnetization data from the crystal grown in $CO:CO_2$=1:3

possesses sharper transitions with no impurities, an a.c susceptibility measurement of this crystal my provide a better insight into the true onset of frequency dependence. An absence of powder refinement data of the polycrystalline sample used in their a.c. susceptibility measurements, as well as a coherent magnetization measurement, it makes it difficult to determine whether the polycrystalline sample produced by Sun *et al.* is single phase containing no impurities. Despite this, the data sets do corroborate well with each other and provide the first insight into possible spin glass states below the main Néel temperature at 250 K.

Neutron scattering is the final key to uncovering the type of magnetism and CO which exists at the transition temperatures seen in the magnetization and specific heat data, however, at present, there is no published neutron data on $YbFe_2O_4$ based on the difficulty of synthesis and off-stoichiometric effects. A single crystal of 60 mg isolated from the $YbFe_2O_4$ single crystal, grown in $CO:CO_2$=1:3.5 was measured at DNS-FRM II. Magnetization of the crystal selected for DNS showed very smeared out transitions (refer to section (4.9.1)) compared to that shown in figure 4.24, which indicates the large variations in stoichiometry that can occur within one single crystal growth. The experimental results obtained from the measurement time at DNS highlighted 2D diffuse magnetic scattering along the (1/3, 1/3, l) line and (2/3, 2/3, l) line, similar to the $LuFe_2O_4$ with non ideal stoichiometry. The spin flip polarization data was taken at 255, 199, 100 and 3.65 K corresponding to the transition temperatures seen in the magnetization data. Despite only seeing the presence of 2D magnetic order, it is clear that the count rate below T_N is approximately 100 times higher at 100 K than at 255 K. Therefore it seems logical, that with the same counting time used for the 60 mg sample of $YbFe_2O_4$, the smaller crystal of 3.5 mg with sharp features in the magnetization data, which is only 10 times smaller, should produce clear magnetic peaks below T_N, with the expected presence of 3D magnetic order. The existence of 3D magnetic order in a stoichiometric $YbFe_2O_4$ single crystal will show a direct correlation to the recently published data by Groot *et al.*, group on $LuFe_2O_4$, where they see sharp CO and Magnetic peaks along the (1/3, 1/3, l) line (65).

4.4 Stoichiometry, Magnetism and CO

New investigations into the varying stoichiometry of $YbFe_2O_4$ has uncovered new transitions not reported previously. Growing $YbFe_2O_4$ in three different oxygen partial pressure environments; $CO:CO_2$=1:5, $CO:CO_2$=1:3.5 and $CO:CO_2$=1:3.5, has provided the first real insight into how $YbFe_2O_4$ acts in oxygen rich and oxygen reduced atmospheres. Initial powder diffraction experiments highlighted a complete phase decomposition, for the crystal grown in the more oxidizing gas ratio $CO:CO_2$=1:5. Powder diffraction data from $YbFe_2O_4$ grown in $CO:CO_2$=1:3 was refined as single phase. However diffraction data taken from the crystal grown in $CO:CO_2$=1:3.5 exhibited an FeO impurity and could only be refined using this secondary phase, as well as the main $YbFe_2O_4$ phase. Obtaining large single crystals from the crystals grown in $CO:CO_2$=1:3 and $CO:CO_2$=1:3.5 was difficult, due to the large number of domains present. Small single crystals of mass 3-5 mg were used for all the macroscopic measurements. There is a distinct difference in the magnetization data from both crystals, where the features exhibited by the (1:3) crystal are sharper and more defined than that of the (1:3.5) crystal. Both sets of specific heat data on each crystal show the same, sharp CO peak at ∼304 K but a drop in the overall specific heat is seen in the (1:3.5) crystal. Single crystal x-ray diffraction of the crystal grown in the $CO:CO_2$=1:3 gas atmosphere, exhibited only strong diffuse scattering, which was also seen in the DNS data, as well as the appearance on 2D magnetic order. The a.c susceptibility highlighted the presence of spin glass states below the main Néel temperature, which are in good agreement with (79). A valance splitting of Fe^{2+} and Fe^{3+} as well as electric dipole and magnetic quadrupole splitting which is seen in Mössbauer spectra for the powdered crystal in $CO:CO_2$=1:3.5, but is yet to be fit to a suitable model. The Mössbauer data shows an almost identical peak splitting to that seen in (46). It seems that from all the macroscopic investigations, the crystal grown in $CO:CO_2$=1:3 is of a slightly better stoichiometric quality than that of the crystal grown in $CO:CO_2$=1:3.5, where slight increases in the oxygen content beyond $CO:CO_2$=1:3 cause small phase decompositions of the initial single phase $YbFe_2O_4$. Unlike $LuFe_2O_4$, the use of the $CO:CO_2$=1:5 gas atmosphere during the crystal growth of $YbFe_2O_4$ promotes a total phase break down. This is based on the mass of the Yb atom which is less than the Lu atom and ionic the distancing between the Yb-O ligands is less than that of the Lu-O. Therefore the

use of a more oxidizing gas ratio, which was stable for the crystal growth of $LuFe_2O_4$, will create a complete instability in $YbFe_2O_4$ structure, due to it's inability to support the excess oxygen atoms. The use of the more reducing oxygen partial pressure environments: $CO:CO_2$=1:3 and $CO:CO_2$=1:3.5 provides more stability between the Yb-O and promotes stronger magnetic and CO correlations throughout the crystal unit cell. Further investigation into different oxygen partial pressures may provide a spectrum of poor to good stoichiometric crystals, highlighting a specific gas ratio which forms the best stoichiometric (quality) crystals.

5

Conclusion

A study investigating both the magnetic and CO characteristics of $LuFe_2O_4$ single crystals grown in $CO:CO_2$=1:3 and $CO:CO_2$=1:5 and $YbFe_2O_4$ single crystals grown in $CO:CO_2$=1:3, $CO:CO_2$=1:3.5 and $CO:CO_2$=1:5 have been presented.

The single crystals measured of $LuFe_2O_4$, exhibited quite contrasting behavior based on off-stoichiometry. Evidence of 3D CO and sharp magnetic transitions were seen in the magnetization, specific heat and single crystal x-ray diffraction measurements performed on the (1:5) crystal. Conversely, the (1:3) crystal exhibited only 2D CO through single crystal x-ray diffraction, where only a single broad transition was featured in the magnetization data and supported by smeared transitions at both the main Néel temperature and the onset of CO in the specific heat data. On measuring the specific heat of the (1:5) crystal, the temperature was taken to 400 K, which caused a noticeable change in the FC data during a remeasure of the magnetization, highlighting a change in the oxygen stoichiometry. Based on the collection of macroscopic data, the $LuFe_2O_4$ crystal grown in $CO:CO_2$=1:5 seems to exhibit magnetic and CO characteristics comparable to recent publications by deGroot *et al.* (65), (66), and therefore currently the closest possibility to the correct stoichiometry.

Studies made on $YbFe_2O_4$ show that the more oxidizing gas ratio, which provided the optimum atmospheric conditions for $LuFe_2O_4$, do not apply to the single crystal growth of $YbFe_2O_4$. The $CO:CO_2$=1:5 gas ratio was far too oxidizing and resulted in a complete phase decomposition. Single crystals of $YbFe_2O_4$ were obtained using $CO:CO_2$=1:3 and $CO:CO_2$=1:3.5 atmospheric conditions. The small increase of 0.5

with the more oxidizing gas ratio produced an FeO impurity, where single crystal powder diffraction could only be refined with a secondary phase of FeO and the main phase $YbFe_2O_4$. The magnetization data provides a detailed insight into the qualities of both the (1:3) and (1:3.5) single crystals, where slightly sharper features and a higher overall magnetization is seen in the (1:3) crystal. A measurement of the specific heat for each crystal show almost identical curves, both indicating the onset of CO below 305 K, however a slight lowering of the overall specific heat capacity is seen for the (1:3.5) crystal. The single crystal x-ray diffraction of a small (1:3) single crystal shows diffuse CO lines emerging at 350 K, but based on the specific heat data and the peak at 305 K, which is in good agreement with the peak seen at 314 K in the specific heat data of the $LuFe_2O_4$ (1:5) crystal, does not exhibit 3D CO. This may not be an artifact of the the compound itself, but rather the small crystal selected for the measurement was of poor stoichiometric quality and further measurements with a selection of crystals should highlight the presence of 3D CO. Measurements of a.c susceptibility provided a more detailed look at the transitions present in the magnetization data for the (1:3.5) crystal. The onset of a frequency dependence in the imaginary part of the a.c. susceptibility highlighted the presence of a glassy state, indicating possible competing magnetic states. Mössbauer spectroscopy presented similar results to those previously reported on $LuFe_2O_4$ by Xu *et al.* (77), indicating quadrupole splitting and the onset of a Fe^{2+} and Fe^{3+} valence state below 310 K, with further hyperfine spitting below 230 K. The nature of the hyperfine splitting below 230 K is yet to be fit to a model and is still under investigation. Final investigations into the magnetic ordering of $YbFe_2O_4$ through the use of spin polarized neutrons provided the first insight into the effects of stoichiometry and the type of magnetism and CO. A $YbFe_2O_4$ (1:3.5) single crystal of mass 60 mg exhibited smeared out transitions compared to the initial magnetization data from the smaller crystal, only highlighting the main Néel transition and a broad maximum at 131 K. The large sample to sample dependence within one crystal growth is greatly apparent from this difference, and based on the lower stoichiometric quality of this crystal, only diffuse 2D magnetic order was seen along with weak diffuse CO. However based on the high count rate observed during the experiment, it is safe to assume that using the (1:3.5) smaller crystal of 3.5 mg, which exhibits very sharp transitions in the magnetization data, could be used used for a following neutron scattering experiment, to look for 3D magnetic and charge order. The wide range of macroscopic experiments

performed indicate that the (1:3) crystal is of slightly better stoichiometric quality than that of the (1:3.5) crystal, and that the magnetization data highlights transitions which have not been previously published. It is clear that the sensitivity to oxygen stoichiometry plays a large role in the magnetism and CO of $YbFe_2O_4$, like with $LuFe_2O_4$, and the data presented in this thesis provides the first insight into $YbFe_2O_4$ single crystals of good stoichiometric quality.

5.1 Future work

In order to investigate the true nature of the magnetic excitations and spin-charge coupling in $LuFe_2O_4$, a large 1.5 g single crystal grown in $CO:CO_2$=1:5 will be used in an inelastic neutron scattering experiment, scheduled to be performed at the instrument 4SEASONS at J-Parc, Japan.

To investigate whether the stoichiometry of $YbFe_2O_4$ grown in $CO:CO_2$=1:3 produces the best magnetic and CO characteristics, a new crystal grown in $CO:CO_2$=1:2.5 will provide us with a good cross comparison to that of the crystals already grown and presented in this thesis. A new measurement at DNS with a crystal of better stoichiometric quality, exhibiting all the sharp features should highlight if 3D magnetic order really does exist.

Bibliography

[1] Cheong, S-W. and Mostovoy, M., *Multiferroics: a magnetic twist for ferroelectricity*, Nature Materials **6**, 13-20 (2007). 1, 2, 5, 6, 7, 11, 12, 13

[2] Ikeda, N., Ohsumi, H., Ohwada, K., Ishii, K., Inami, T., Kakurai, K., Murakami, Y., Yoshii, K., Mori, S., Horibe, Y. and Kito, H., textitFerroelectricity from iron valence ordering in the charge-frustrated system $LuFe_2O_4$, Nature **436**, 1136-1138, (2005). 1, 45, 46, 47, 48, 49

[3] Spaldin, N. A., Cheong, S-W. and Ramesh, R., *Multiferroics: Past, present, and future*, Physics today, **60** p38 (2010). 1, 2, 7

[4] Auciello, O., Scott, J. F. and Ramesh, R., textitThe Physics of Ferroelectric Memories, Phys. Today **51**(7), **22** (1998). 1

[5] 5 Schmid, H. *Ferroelectrics* **162**, 317 (1994). 2

[6] Spaldin, N. A., and Fiebig, M., *The Renaissance of Magnetoelectric Multiferroics*, SCIENCE, **309** (2005). 2, 3

[7] Ramesh, R. and Spaldin, N. A., textitMultiferroics: progress and prospects in thin films, Nature Materials **6**, 21-29 (2007). 2

[8] Feynman, R.P., Leighton, R. B., Sands, M., (1970), textitLectures on Physics, Vol 2, Addison Wesley. 3

[9] Khomskii, D. I., *Multiferroics: Different ways to combine magnetism and ferroelectricity*, Journal of Magnetism and Magnetic Materials, **306**, 1-8, (2004). 3

[10] 10 Fiebig, M., *Revival of the magnetoelectric effect*, J. Phys. D: Appl. Phys. **38** (2005). 3, 4

[11] Eerenstein, W., Mathur, N.D., and Scott, J.F., Nature **442,** p759-765 (2006). 5

[12] Khomskii, D. I., *Classifying multiferroics: Mechanisms and effects*, Physics **2**, **20** (2009). 5, 6, 8, 10, 11

[13] Katsufuji, T., Mori, S., Masaki, M., Moritomo, Y., Yamamoto, N., Takagi, H.. *Dielectric and magnetic anomalies and spin frustration in hexagonal $RMnO_3$ (R = Y, Yb, and Lu)*. Phys. Rev. B **64**, 104419 (2001). 7

[14] Van Aken, B. B., Palstra, T. T. M., Filippetti, A. and Spaldin, N. A.. *The origin of ferroelectricity in magnetoelectric $YMnO_3$*. Nature Mater. **3**, 164170 (2004). 10, 11

[15] 15 Fennie, C. J. and Rabe, K. M.. *Ferroelectric transition in $YMnO_3$ from first principles.* Phys. Rev. B **72**, 100103 (2005). 7

[16] Ikeda, N., Moric, S., and Yoshii, K., *Ferroelectricity from Valence Ordering in RFe_2O_4*. Ferroelectrics, **348**, Issue 1, (2007). 7

[17] Quezel-Ambrunaz, S., Bertaut, F. and Buisson, G. Structure of TMn_2O_5 compounds of rare earth and manganese oxides. Compt. Rend. **258**, 30253027 (1964). 7

[18] Schieber, M., Grill, A., Nowik, T., Wanklyn, B. M. Y., Sherwood, R. C. and Van Uitert, L. G.. *Magnetocrystalline anisotropy of rare-earth manganites.* J. Appl. Phys. **44**, 18641867 (1973).

[19] Golovenchits, E. I., Morozov, N. V., Sanina, V. A. and Sapozhnikova, L. M.. *Correlation of magnetic and dielectric properties in $EuMn_2O_5$ single crystals.* Sov. Phys. Solid State **34**, 5659 (1992).

[20] 20 Saito, K. and Kohn, K. *Magnetoelectric effect and low-temperature phase transitions of $TbMn_2O_5$*. J. Phys. Condens. Matter **7**, 28552863 (1995).

[21] Inomata, A. and Kohn, K.. *Pyroelectric effect and possible ferroelectric transition of helimagnetic $GdMn_2O_5$, $TbMn_2O_5$ and YMn_2O_5*. J. Phys. Condens. Matter **8**, 26732678 (1996).

[22] Gardner, P. P., Wilkinson, C., Forsyth, J. B. and Wanklyn, B. M.. *The magnetic structures of the rare earth manganates $ErMn_2O_5$ and $TbMn_2O_5$*. J. Phys. C: Solid State Phys. **21**, 56535661 (1998). 7

[23] Van den Brink, J. and Khomskii. D. I.. *Multiferroicity due to charge ordering*. J. Phys.: Condens. Matter **20** (2008). 8, 9

[24] Blundell, S. (2001).*Magnetism in Condensed Matter*. New York: Oxford University Press Inc. 9, 15, 39

[25] 25 Hase, M., Terasaki, I. and Uchinokura, K.. Phys. Rev. Lett. **70**, 3651 (1993). 9

[26] Multiferroics Recent history, current excitement and future directions, Nicola Spaldin, European School on Multiferroics presention, Groningen, September. (2009) 10

[27] 27 Volkova, L.M. and Marinin, D.V..*Magnetoelectric Ordering of $BiFeO_3$ from the Perspective of Crystal Chemistry*. J Supercond Nov Magn. **24**:21612177 (2011). 10

[28] 28 Noda, Y., Fukuda, Y., Kimura, H., Kagomiya, I., Matumoto, S., Kohn, K., Shobu, T., and Ikeda. N., *Review and Prospect of Ferroelectricity and Magnetism in YMn_2O_5*, Journal of the Korean Physical Society, **42**, 1192-1195, (2003). 13

[29] 29 Subramanian, M.A., He, T., Chen, J., Rogado, N.S., Calvarese, T.G. and Sleight, A.W.. *Giant RoomTemperature Magnetodielectric Response in the Electronic Ferroelectric $LuFe_2O_4$*. Adv. Mater. **18**, 1737-1739 (2006). 14

[30] 30 Ikeda, N., *Ferroelectric properties of triangular charge-frustrated $LuFe_2O_4$*. J. Phys.: Condens. Matter **20** 434218, (2008). 14, 15

[31] Ko, K.-T., Noh, H.-J., Kim,J.-Y., Park, B.-G., Park, J.-H., Tanaka, A., Kim, S.B., Zhang, C. L. and Cheong, S.-W.. *Electronic Origin of Giant Magnetic Anisotropy in Multiferroic $LuFe_2O_4$* Phys. Rev. Lett. **103**, 207202 (2009). 15

[32] 32 de Groot, J. (2012). *Charge, spin and orbital order in the candidate multiferroic material $LuFe_2O_4$*. Ph.D thesis. RWTH Aachen University. 15, 16, 32, 49, 51, 73, 109

[33] Yamada, Y., Kitsuda, K., Nohdo, S. and Ikeda, N.. *Charge and spin ordering process in the mixed-valence system $LuFe_2O_4$: Charge ordering* Phys. Rev. B **62**, 18 (2000). 16

[34] Kimizuka, N. and Katsura, T.. *Standard free energy of formation of $YFeO_3$, $Y_3Fe_5O_{12}$, and a new compound YFe_2O_4 in the $FeFe_2O_3$ Y_2O_3 system at 1200° C* J. Solid State Chem. **13**, 176 (1975). 17

[35] 35 Kitayama, K. Sakaguchi, M., Takahara, Y., Endo, H. and Ueki, H.. *Phase equilibrium in the system Y-Fe-O at 1100 ° C*, J. Solid State Chem. **177**, 1933 (2004). 17

[36] 36 Shindo, I., Kimizuka, N. and Kimura, S., *Growth of YFe_2O_4 single crystals by floating zone method*, Mater. Res. Bull. **11**, 637 (1976). 18

[37] Mueller, T. (2012). *Charge and spin order in highly stoichiometric $YFe_2O_{4-\delta}$ single crystals*. Diplomarbeit. RWTH Aachen University. 18, 19, 106

[38] Sugihara, T., Siratori, K., Shindo, I. and Katsura, T., *Parasitic Ferrimagnetism of YFe_2O_4*, J. Phys. Soc. Jpn. **45**, 1191 (1978). 18

[39] Inazumi,M., Nakagawa, Y., Tanaka, M., Kimizuka, N. and Siratori, K., *Magnetizations and Mssbauer Spectra of YFe_2O_{4-x}*, J. Phys. Soc. Jpn. 50, **438** (1981). 19, 80

[40] 40 Ikeda, N., Mori, R., Mori, S. and Kohn, K., *Structure Transition and Charge Competition on YFe_2O_4*, Ferroelectrics **286**, **175** (2003). 19

[41] 41 Iida, J., Nakagawa, Y. and Kimizuka, N., *Field Heating Effect Anomalous Thermomagnetization Curves Observed in Hexagonal $LuFe_2O_4$*, J. Phys. Soc. Jpn. **55**, 1434 (1986). 20, 50, 67, 69

[42] Michiuchi, T., Yokota, Y., Komatsu, T., Hayakawa, H., Kuroda, T., Maeda, D., Matsuo, Y., Mori, S., Yoshii, K., Hanasaki, N., Kambe, T. and Ikeda, N., *Stoichiometric Study of the Dielectric and Magnetic Properties in Charge Frustrated System $LuFe_2O_4$* , Ferroelectrics, **378:1**, 175-180 (2009). 21, 47, 67, 73

[43] Kimizuka, N., Takenaka, A., Sasada Y. and Katsura, T., *A series of New compounds $A^{3+}Fe_2O_4$ (A = Ho, Er,Tm, Yb, and Lu)*, Solid State Communications, **15**, 13211323, (1974). 23, 75, 80

[44] 44 Kimizuka, N. and Katsura, T., *The Standard Free Energy of Rormation of $YbFe_2O_4$, $Yb_2Fe_3O_7$, $YbFeO_3$ and $Yb_3Fe_5O_{12}$ at 1200° C*, Journal of Solid State Chemistry, **15**, 151-157 (1975). 23, 87, 91

[45] 45 Kishi, M., Miura, S., Nakagawa, Y., Kimizuka, N., Shindo, I. and Siratori, K., *Magnetization of YFe_2O_{4-x}*, Journal of the Physical Society of Japan, **51**, 2801-2805, (1982). 24, 75, 79

[46] 46 Tanaka, M., Iwasaki, H., Siratori, K. and Shindo, I., *Mossbauer Study on the Magentic Structure of $YbFe_2O_4$: A Two-Dimensional Antiferromagnet on a Triangular Lattice*, Journal of the Physical Society of Japan, **58**, 1433-1440, (1989). 25, 75, 111, 113, 114, 119

[47] Iida, J., Kakugawa, S., Kido, G., Nakagawa, Y., Takekawa, S. and Kimizuka, N., *High Fiels Magentization of Single Crystals YFe_2O_4, $YbFe_2O_4$ and $LuFe_2O_4$*, Physica B, **155**, 307-310, (1989). 25, 43

[48] Yoshii, K., Ikeda, N., Matsuo, Y., Horibe, Y. and Mori, S., Magnetic and dielectric properties of RFe_2O_4, $RFeMO_4$, and $RGaCuO_4$(R=Yb and Lu, M=Co and Cu), Phys. Rev. B, **76**, 024423 (2007). 25, 75, 76, 79, 109, 110

[49] Murakami, Y., Abe, N., Arima, T. and Shindo, D., Charge-ordered domain structure in $YbFe_2O_4$ observed by energy-filtered transmission electron microscopy, Phys. Rev. B, **76**, 024109 (2007). 25, 76, 77, 78

[50] 50 Hearmon, A. J., Prabhakaran, D., Nowell, H., Fabrizi, F., Gutmann, M. J.and Radaelli, P. G., Helical scattering signatures of strain and electronic textures in $YbFe_2O_4$ from three-dimensional reciprocal-space imaging, Phys. Rev. **85**, 014115 (2012). 25, 77, 78, 111, 112, 113

[51] Als-Nielsen, J. and McMorrow, D. (2001). *Elements of Modern X-Ray Physics*. New York: John Wiley and Sons. 30

[52] O'Flynn, D. (2010). *Multiferroic properties of rare earth manganites*. Ph.D. thesis. University of Warwick. 31, 33, 34

[53] 53 Quantum Design. *PPMS (Physical Properties Measurement System)*. 1070-002. Rev. A0. 35, 36

[54] 54 Martien, D. *Introduction to: AC Susceptibility*. San Diego: Quantum Design Corporate Headquarters. 38

[55] Quantum Design. (2003). *Physical Properties Measurement System: AC Measurement System (ACMS) Option User's Manual*. San Diego: Quantum Design. 38, 39

[56] 56 Gütlich, P. *Fifty Years of Mssbauer Spectroscopy in Solid State Research Remarkable Achievements, Future Perspectives* . Z. anorg. allg. Chem., **638**, 1543, (2012). 39, 40, 41

[57] Brueckel, T., Heger, G., Richter. D., Roth, G. and Zorn, R. (2012). *Neutron Scattering*. Germany: Forschungszentrum Jueich GmbH. 41, 42

[58] 58 Iida, J., Nakagawa, Y., Funahashi, S., Takeawa, S. and Kimizuka, N., Two-Dimensional Magnetic Order in Hexagonal $LuFe_2O_4$, Journal De Physique, Colloque CS, Supplément au N^o 12, Tome 49, (1988). 43, 49

[59] Iida, J., Takekawa, S. and Kimizuka, N., *Single Crystal Growth of $LuFe_2O_4$, $LuFeCoO_4$ and $YbFeMgO_4$ by the Floating Zone Method, Journal of Crystal Growth*, **102**, 398-400, (1990). 43

[60] 60 Ikeda, N., Yamada, Y., nohdo, S., Inami, T. and Katano, S., Incommensurate charge order in mixed valence system $LuFe_2O_4$, Physica B, **241-241**, 820-822, (1998). 43, 44, 45, 49, 52, 77, 78

[61] 61 Lewtas, H., Ph.D. thesis, University of Oxford (2010). 43

[62] Christianson, A.D., Lumsden, M.D., Angst, M., Yamani, Z., Tian, W., Jin, R., Payzant, E.A., Nagler, S.E., Sales, B.C. and Mandrus, D., *Three-Dimensional Magnetic Correlations in Multiferroic $LuFe_2O_4$* Phys. Rev. Letts. **100**, 107601 (2008). 45, 49, 72, 73

[63] Xu, X. S., Angst, M., Brinzari, T. V., Hermann, R. P., Musfeldt, J. L., Christianson, A. D., Mandrus D., Sales, B. C., McGill, S. Kim, J.-W. et al., *Charge Order, Dynamics, and Magnetostructural Transition in Multiferroic $LuFe_2O_4$*, Phys. Rev. Lett. **101**, 227602 (2008). 50

[64] 64 Wang, F., Kim, J., and Kim, Y-J., *Spin-Glass behavior in $LuFe_2O_{4-\delta}$*, Phys. Rev. B,**80**, 024419 (2009). 51, 67, 68, 69

[65] de Groot , J., Marty, K., Lumsden, M. D., Christianson, A D., Nagler, S. E., Adiga, S., Borghols. W. J. H., Schmalzl, K., Yamani, Z., Bland, S. R., de Souza, R., Staub, U., Schweika, W., Su, Y. and Angst, M., *Competing Ferri- and Antiferromagnetic Phases in Geometrically Frustrated $LuFe_2O_4$* Phys. Rev. Lett. **108**, 037206 (2012). 52, 53, 54, 69, 71, 73, 118, 121

[66] de Groot, J., Mueller, T., Rosenberg, R. A., Keavney, D. J., Islam, Z., Kim., J.-W. and Angst. M., *Charge order in $LuFe_2O_4$: an unlikely route to ferroelectricity*, Phys. Rev. Lett. **108**, 187601 (2012). 55, 56, 57, 70, 121

[67] 67 Angst, M., Hermann, R. P., Christianson, A. D., Lumsden, M. D., Lee, C., Whangbo, M.-H., Kim, J.-W., Ryan, P. J., Nagler, S. E., Tian, W., Jin, R., Sales, B. C. and Mandrus, D., *Charge Order in $LuFe_2O_4$: Antiferroelectric Ground State and Coupling to Magnetism*, Phys. Rev. Lett. **101**, 227601 (2008). 55

[68] M^{c}Kinnon, R. A., (2011), *Studies of New Multiferroics*, Ph.D. thesis, University of Warwick. 67, 82, 110

[69] 69 Taran, S., Chou, C. C., Her, J. L., Sun, C. P., Lin, C. C., Chan, C. L., Huang, C. L. and Yang, H. D., *Study of magnetic dynamics of $LuFe_2O_4$*, Journal of Physics: Conference Series **150**, 042205 (2009). 67

[70] Yang, H.X., Tian, H.F., Zhang, Y., Qin, Y.B., Zeng, L.J., Ma, C., Shi, H.L. Lu, J.B. and Li, J.Q. *Phase separation and ferroelectric ordering in charge frustrated $LuFe_2O_{4-\delta}$*, Beijing National Laboratory for Condensed Matter Physics, Institute of Physics, Chinese Academy of Sciences, Beijing 100190, China, PACS number(s): 77.84.-s; 71.27.+a; 61.05.J-; 71.23.An. 68

[71] Phan, M. H., Frey, N. A., Srikanth, H., Angst, M., Sales, B. C. and Mandrus D., *Magnetism and cluster glass dynamics in geometrically frustrated* $LuFe_2O_4$, Journal of Applied Physics, **105**, 07E308 (2009). 72

[72] 72 Serrao, C. R., Sahu, J. R., Ramesha, K. and Rao, C. N. R., *Magnetoelectric effect in rare earth ferrites,* $LnFe_2O_4$, J. Appl. Phys. **104**, 016102 (2008). 79

[73] Kato, K., Kawada, I., Kimizuka, N., Katsura, T. Materials Research Bulletin **15**, 647-655, (1980). 84, 89

[74] Bourbia, A., Draissia, M., Bedboudi, H., Boulkhessaim, S., Debili, M.Y., *X-ray and optical crystallographic parameters investigations of high frequency induction melted Al-(alpha-*Al_2O_3*), alloys.*, Journal of X-ray Science and Technology **18**, 201-219 (2010). 86

[75] 75 Crisan, O., Crisan, A.D., *Phase transformation and exchange bias effects in mechanically alloyed Fe/magnetite powders*, Journal of Alloys Compd. **509**, 6522-6527 (2011). 87, 89

[76] Nakagawa, Y. Inazumi, M. Kimizuka, N. and Siratori, K., *Low-Temperature Phase Transitions and Magnetic Properties of* YFe_2O_4, J. Phys. Soc. Jpn. **47**, 1369 (1979). 110

[77] 77 Xu, X. S., Angst, M., Brinzari, T.V. Hermann, R. P., Musfeldt, J. L., Christianson, A. D., Mandrus, D. and Sales, B. C., *Charge Order, Dynamics, and Magnetostructural Transition in Multiferroic* $LuFe_2O_4$, Phys. Rev. Letts. **101**, 227602 (2008). 113, 115, 122

[78] Tjon, J. A. and Blume, M., Phys. Rev. **165**, 456 (1968). 113

[79] Sun, Y., Liu, Y. Ye, F., Chi, S., Ren, Y., Zou, T., Wang, F. and Yan, L., *A magnetoelectric multiglass state in multiferroic* $YbFe_2O_4$, Journal of Applied Physics **111**, 07D902 (2012). 116, 117, 119

Declaration

The work presented in this thesis was carried out by me, except where explicitly stated. All of the work took place between November 2011 and January 2013 and was carried out at the Department of Physics at the University of Warwick and Jülich Forschungszentrum. The experimental data presented in Chapter 3 was collected from $LuFe_2O_4$ single crystal previously grown and oriented by Ruth M^{c}kinnon at the University of Warwick.